WARSAW UNIVERSITY OF TECHNOLOGY

ENVIRONMENTAL ENGINEERING, MINING AND POWER ENGINEERING
ENGINEERING AND TECHNOLOGY

Ph.D. Thesis

Rafał Rogóż, M.Sc.

The influence of flash-boiling effect on droplet size distributions of low-pressure sprays under various ambient pressures and fluid temperatures

Supervisor
Prof. Andrzej Teodorczyk, D.Sc., D.Eng.

Co-supervisor
Łukasz Jan Kapusta, D.Eng.

WARSAW 2022

Acknowledgements

I would like to express my sincere gratitude to my supervisor, Prof. Andrzej Teodorczyk, for mentoring and guidance in my Ph.D. study. His support helped me to confidently pursue my academic goals. I would like to thank my co-supervisor, Dr. Łukasz Jan Kapusta, for his invaluable advices and discussions during these years that shaped my understanding of flash boiling sprays, and also for organizing visits to international institutions and coordination of projects. I would like to thank the Laser Diagnostic Laboratory team, Dr. Łukasz Boruc and Jakub Bachanek, for many hours of work in the laboratory and on numerical modelling.

My sincere thanks to the hosting institutions, which helped me to find an idea for the dissertation. I would like to thank Dr. Klaus Pachler and Dr. Eberhard von Berg from AVL List GmbH (Graz, Austria) for guidance on flash-boiling numerical modelling issues, especially nucleation and angle enhancement correlations. I am thankful to Prof. Jeffrey Naber from Michigan Technological University (Michigan, USA) for his hands-on experience with statistical analysis.

I also would like to acknowledge financial support as the project leading to this application has received funding from the National Centre for Research and Development (NCBiR), (Grant No. MAZOWSZE/0101/19-00), programme Scieżka dla Mazowsza, project budget: 9,880,490.25 PLN.

Finally, I would like to thank my loved ones for both, their patience and support during my PhD studies.

Streszczenie

Zjawisko gwałtownego wrzenia zachodzi gdy ciecz ulega nagłemu zmniejszeniu ciśnienia poniżej ciśnienia nasycenia w danej temperaturze. W praktyce, realizacja takiego procesu może odbyć się podczas wtrysku cieczy, w trakcie którego dojdzie do nukleacji bąbli parowych. Tworzące się bąble spowodują przepływ dwufazowy w dyszy wtryskiwacza. Przy odpowiednich warunkach może również dość do zjawiska gwałtownego wrzenia na zewnątrz dyszy. Wówczas pęcherzyki pary, które znajdują się w pojedynczych kroplach ulegają gwałtownej ekspansji powodując "mikro eksplozje" i powstawanie mniejszych kropel.

Zjawisko gwałtownego wrzenia jest rozważane jako alternatywa do podwyższania ciśnienia wtrysku w celu poprawy atomizacji. Poprzez odpowiedni dobór parametrów cieczy przegrzanej, można otrzymać chmurę kropel, która będzie bardziej jednorodna pod względem rozmiaru i rozmieszczenia kropel w przestrzeni oraz będzie charakteryzować się mniejszymi kroplami, zmniejszoną penetracją i poszerzonym kątem stożka wtrysku.

Analiza literatury w temacie gwałtownego wrzenia ukazuje, że temat ten jest intensywnie eksplorowany przez wielu naukowców. Duży nacisk został położny za zrozumienie zjawisk towarzyszącym gwałtownemu wrzeniu, tj. poszerzeniu kąta wtrysku, zapadaniu się chmury kropel oraz redukcji rozmiarów kropel. Jednakże, w zakresie tych prac brak jest badań odnośnie wpływu stopnia przegrzewu na charakterystykę rozkładu rozmiarów kropel dla wtrysku pod niskim ciśnieniem. Dodatkowo brakuje oceny wpływu temperatury wtryskiwanej cieczy oraz ciśnienia otoczenia, sterowanych oddzielnie, na stopień redukcji średnicy kropel. Jest to szczególnie istotne ze względu na fakt, że badania dla wtryskiwaczy wysokociśnieniowych wskazały na wyraźny wpływ tych parametrów na proces atomizacji, pomimo tego, że gwałtowne wrzenie jest zjawiskiem dominującym. W niniejszej rozprawie, wskazana luka w aktualnym stanie wiedzy została uwzględniona.

Celem niniejszej pracy jest określenie wpływu gwałtownego wrzenia na charakterystyki rozkładu rozmiaru kropel oraz zamodelowaniu tego zjawiska w funkcji stopnia przegrzewu. W tym celu przeprowadzono systematyczne badania podczas których wodę o różnej temperaturze wtryskiwano do komory o stałej objętości wypełnionej powietrzem pod różnym ciśnieniem. Kontrola temperatury cieczy odbywała się poprzez płaszcz chłodzący komercyjnego wtryskiwacza niskociśnieniowego, który zamontowany był w gnieździe komory z dostępem optycznym. Pomiar kropli odbywał się przy użyciu metody cienia z mikroskopią dalekiego zasięgu.

Wyniki badań pokazały, że zarówno ciśnienie otoczenia jak i temperatura wtrysku wpływa na redukcję wielkości kropel. Pokazano, że utrzymując ten sam stopień przegrzewu, wyrażony jako stosunek ciśnienia nasycenia do ciśnienia otoczenia, otrzymane dystrybucje rozmiarów kropel wyraźnie się różnią. Jednakże, pogrupowane wyniku ze względu na temperaturę wtrysku, jasno pokazują, że wszystkie grupy charakteryzują się podobnym i spójnym trendem

tj. redukcją kropel w całym zakresie średnic kropel oraz stopniowym zmniejszaniem stopnia redukcji wraz z rosnącym przegrzewem.

Na podstawie wyników badań eksperymentalnych został utworzony model pozwalający na tworzenie rozkładów prawdopodobieństwa wielkości kropel w funkcji parametrów przegrzewu. Model ten uwzględnia uśredniony trend redukcji wielkości kropel, który został zaobserwowany dla każdej z rozważanych temperatur wtryskiwanej cieczy. Utworzony model odwzorowuje główne trendy z satysfakcjonującym poziomem dokładności dla wszystkich przebadanych warunków eksperymentu.

Słowa kluczowe: gwałtowne wrzenie, atomizacja, rozkład kropel, wtrysk niskociśnieniowy

Abstract

Flash boiling occurs when a heated liquid is suddenly depressurized below its saturation pressure. This scenario can be achieved by overheated fluid injection into the ambient conditions. Due to the nucleation process, bubbles are constantly created inside the flow resulting in two-phase flow through the nozzle. Under certain conditions, this is followed by rapid vapour bubbles expansion inside the droplet and micro explosion of droplets into smaller sizes. As a result, a spray with improved atomization can be achieved.

The flash-boiling phenomenon can be an interesting alternative for improving droplet atomization to the elevation of injection pressure, as this method often leads to a simultaneous increase in spray penetration. This problem can be solved by a proper adjustment of flash-boiling conditions and producing cloud with more uniform droplet and mass distribution, reduced penetration and wider spray angle.

The literature shows a great interest in this topic by researchers from numerous fields of study. A great emphasis was put on understanding of flash boiling-induced phenomena like angle spreading, spray collapse and droplet size reduction. Nevertheless, the review of state-of-the-art revealed that there is a lack of studies regarding the influence of flash-boiling intensity on droplet size distribution shape for low-pressure fluid injection. What is more, there is no studies regarding the individual influence of fluid temperature and ambient pressure conditions on the flash-boiling effect in terms of the overheat level. This is especially important since similar studies for high-pressure injections showed the relevant influence of those factors on the atomization process, regardless of the fact that the flash boiling effect is considered the major. This knowledge gap is addressed within this work.

The goal of this work was to understand the influence of flash-boiling parameters on droplet size distribution and to model this influence in function of overheat parameters. For this purpose, systematic experimental tests which covered a broad spectrum of fluid temperature and ambient pressure conditions were conducted. The experiments were carried out on water injected by a modified commercial low-pressure injector with body temperature control through the cooling jacket. The fluid was injected into a constant-volume vessel with optical access, and the shadowgraph technique with long-distance microscope was used to measure the droplet size.

The conducted tests showed that both fluid temperature and ambient pressure affect the droplet size distributions. It was shown that keeping the same overheat level expressed as saturation to ambient pressure ratio for different fluid temperatures gave substantially different results. Nevertheless, a similar and consistent pattern of droplet size reduction could be observed between data series grouped by fluid temperature. Droplets are reduced in the whole range of size and the level of reduction is decreasing with increasing superheat level.

Based on the observations made for experimental results, a model for simulating droplet size distribution at given overheat conditions was proposed. The model takes into account a global trend of droplet size reduction observed for each fluid temperature. The model was found to simulate the droplet size probability density functions with a satisfactory agreement at all performed experimental conditions.

Keywords: flash boiling, atomization, droplet size distribution, low-pressure injection

Contents

Acknowledgements **3**

Streszczenie **5**

Abstract **7**

1 Introduction **19**
1.1 Flash-boiling phenomenon description 20
1.2 Angle enhancement 24
1.3 Spray collapse 28
1.4 Droplet size reduction 34
1.5 Contribution of the thesis and hypothesis 38

2 Materials and methods **41**
2.1 Test matrix 41
2.2 Experimental set-up 42
2.3 Fluid temperature calibration 46
2.4 Test methodology and metrics 48

3 Results and discussion **53**
3.1 Influence of ambient pressure and fluid temperature in non-flash-boiling condition on droplet size distribution 53
3.2 Influence of flash boiling on droplet size distributions 57
3.3 Droplet size distribution model for size predictions 65

4 Summary and conclusions **81**

Bibliography **83**

List of Figures

Figure 1 Schematic view on flash-boiling phenomenon and parameters for overheat description on $P-T$ diagram 20
Figure 2 Schematic view on flash boiling process 21
Figure 3 Schematic view on homogenous and heterogeneous nucleation 22
Figure 4 Schematic view of the droplet breakup mechanism for external flash boiling 23
Figure 5 Spray angle widening for different Rp 24
Figure 6 Spray collapse shown on comparison of spray morphology from a single-hole and multi-hole injectors 28
Figure 7 Ambient pressure and fluid temperature of tests condition; group 1- subcooled conditions at constant injection temperature and various injection pressures; group 2- subcooled conditions at constant pressure and various fluid temperatures; group 3- flash-boiling conditions 42
Figure 8 ΔT and Rp in analysed group 3 43
Figure 9 Experimental setup. Blue solid line - injected liquid; red solid line - heating circuit; black solid line - pneumatic system; black dashed line - electrical hardware connection 44
Figure 10 The injector used in the study 45
Figure 11 Temperature calibration set-up 46
Figure 12 Measured water temperature (T_{fluid}) for different injection frequencies and oil temperatures (T_{oil}) 47
Figure 13 Oil temperature set (T_{oil}) against the desired water temperature 49
Figure 14 Image of calibration plate. The range of dots' sizes are 10-200 µm 49
Figure 15 Image of water injection droplets at $T_{fluid} = 50\,°C$, $P_{amb} = 1$ bar 50
Figure 16 Number (left) and volume (right) based statistics; probability density function (left axis) and cumulative distribution function (right axis) at operating conditions $T_{fluid} = 50\,°C$, $P_{amb} = 1$ bar 51
Figure 17 Volume based probability density functions and cumulative distribution functions for water at $T_{fluid} = 50\,°C$ and different ambient pressures . . . 53
Figure 18 P-value matrix for water at $T_{fluid} = 50\,°C$ and different ambient pressures 54

Figure 19 Droplet size's metrics for water at $T_{fluid} = 50\,°C$ and different ambient pressures 55
Figure 20 Volume based probability density functions and cumulative distribution functions for water at $T_{fluid} = 50\,°C$ and $80\,°C$ at $P_{amb} = 1$ bar 55
Figure 21 Droplet size's metrics for water $T_{fluid} = 50\,°C$ and $80\,°C$ at $P_{amb} = 1$ bar . 56
Figure 22 Volume based probability density functions and cumulative distribution functions for approximately constant $Rp = 1.4$ 58
Figure 23 Volume based probability density functions and cumulative distribution functions for approximately constant $Rp = 2.05$ 58
Figure 24 Volume based probability density functions and cumulative distribution functions for $T_{fluid} = 70\,°C$ at different superheat ratio 59
Figure 25 Droplet size's metrics for water at $T_{fluid} = 70\,°C$ at different superheat ratio 59
Figure 26 Volume based probability density functions and cumulative distribution functions for $T_{fluid} = 80\,°C$ at different superheat ratio 60
Figure 27 Volume based probability density functions and cumulative distribution functions for $T_{fluid} = 90\,°C$ at different superheat ratio 61
Figure 28 Volume based probability density functions and cumulative distribution functions for $T_{fluid} = 100\,°C$ at different superheat ratio 61
Figure 29 Volume based probability density functions and cumulative distribution functions for $T_{fluid} = 110\,°C$ at different superheat ratio 62
Figure 30 Volume based probability density functions and cumulative distribution functions for $T_{fluid} = 120\,°C$ at different superheat ratio 62
Figure 31 Volume based probability density functions and cumulative distribution functions for $T_{fluid} = 130\,°C$ at different superheat ratio 63
Figure 32 Volume based probability density functions and cumulative distribution functions for $T_{fluid} = 140\,°C$ at different superheat ratio 63
Figure 33 $Dv90$, $Dv50$, $Dv10$ and D_{32} versus Rp for water at different fluid temperature 64
Figure 34 Different probability density functions (Weibull, inverse Gaussian and logarithm gamma) and the experimental data; water injection at $T_{fluid} = 80\,°C$, $Rp = 0.94$ 66
Figure 35 Different probability density functions (Weibull, inverse Gaussian and logarithm gamma) and the experimental data; water injection at $T_{fluid} = 80\,°C$, $Rp = 1.57$ 67
Figure 36 Different probability density functions ($K-S$ distance box plots for tested probability density functions 68
Figure 37 Initially selected probability density functions shown for water at $T_{fluid} = 80\,°C$, $Rp = 0.94$ (solid line – PDF, dashed line – CDF) 70

Figure 38 Initially selected probability density functions shown for water at $T_{fluid} =$ 80 °C, $Rp = 1.57$ (solid line – PDF, dashed line – CDF) 70
Figure 39 $K - S$ distance versus Rp for flash-boiling conditions 71
Figure 40 Quantile-quantile plots for log-normal, generalized gamma, beta prime, burr, inverse gaussian and exponentiated Weibull distributions 72
Figure 41 Log-normal distribution function sensitivity for different σ with fixed μ (left plot) and different μ with fixed σ (right plot) 73
Figure 42 Standard deviation σ and mean μ for all cases included in group 3 73
Figure 43 Standard deviation σ versus Rp, and mean μ versus $1/Rp$ for all cases included in group 3. Scattered points – experimental data; solid lines – regressions 75
Figure 44 The averaged droplet sizing model fitted to the experimental data. Scattered points experimental data; solid lines adjusted model 76
Figure 45 Quantile-quantile plot for the model for log-normal distribution and experimental data in the range of 10^{th} to 90^{th} quantile 77
Figure 46 $Dv10$, $Dv50$, $Dv90$ and D_{32}; the model estimation (y-axis) and the experimental data (x-axis) 78
Figure 47 The best case scenario. The droplet size distribution calculated by the model (dashed line), and the log-normal distribution fitted to the experimental data (solid line) for $T_{fluid} = 120$ °C 78
Figure 48 The worst-case scenario. The droplet size distribution calculated by the model (dashed line), and the log-normal distribution fitted to the experimental data (solid line) for $T_{fluid} = 140$ °C 80

List of Tables

Table 1 Injector parameters (spray parameters shown for 5 bar gauge pressure) . . 45
Table 2 Temperature of oil and water (measured) 48

Table 3 List of investigated probability density functions for the best fit 66
Table 4 Coefficients of linear regression (eq. 22 and eq. 23) 74
Table 5 Coefficients f_σ and f_μ coefficient of determination for a averaged droplet sizing model 76
Table 6 $Dv10$, $Dv50$, $Dv90$ and D_{32} metrics for log-normal distribution and for modelled distributions at $T_{fluid} = 120\,°C$ 79
Table 7 $Dv10$, $Dv50$, $Dv90$ and D_{32} metrics for log-normal distribution and for modelled distributions at $T_{fluid} = 140\,°C$ 80

Nomenclature

Abbreviations

CDF	cumulative distribution function
GDI	gasoline direct injection
PDA	phase-Doppler anemometry
PDF	probability density function
SMD	Sauter mean diameter

Symbols

α	shape parameter
α_T	thermal diffusivity
β	shape parameter
ΔT	degree of superheat
$\Delta\mu$	difference between chemical potential at vapour and liquid state
γ	surface tension
λ	shape parameter
μ	mean
ρ	density
σ	standard deviation
A	Antoine's equation constant
B	Antoine's equation constant
C	Antoine's equation constant
C_p	heat capacity
d	droplet diameter
D_{32}	Sauter mean diameter
$Dv10$	10^{th} percentile of volume droplet distribution
$Dv50$	50^{th} percentile of volume droplet distribution
$Dv90$	90^{th} percentile of volume droplet distribution
G_b	Gibbs energy
h_{lv}	latent heat of vaporization
J	nucleation rate
Ja	Jacobi number
k_B	Boltzmann constant

$K-S$	Kolmogorov-Smirnov
P	pressure
$P()$	probability
R^2	coefficient of determination
R_c	critical bubble radius
Rp	superheat ratio
S	super saturation number
T	temperature

Subscripts

amb	ambient
b	bubble
CNT	classic nucleation theory
$fluid$	fluid
inj	injection
KNT	kinetic nucleation theory
l	liquid
oil	oil
sat	saturation
v	volume
vap	vapour

Chapter 1

Introduction

When a heated liquid is injected into an ambient environment below its saturation pressure, the liquid reaches superheated conditions and experiences a so-called flash-boiling. Under such conditions, a rapid boiling of the jet occurs, resulting in a two-phase flow inside the nozzle, due to the nucleation process that constantly generates bubbles inside the liquid phase. Under suitable ambient conditions, a rapid expansion of the vapour phase occurs, providing "micro explosions" of droplets. This phenomenon results in drastically changed spray structure characteristics, which could bring benefits in improved spray atomization, shortened penetration and finer droplets.

The improved spray atomization is often described as an alternative for elevating injection pressure since it has limits, especially connected with raised spray penetration. This, in practical high-pressure injection systems as in gasoline direct injection (GDI) engines, can cause several problems such as unburned hydrocarbons and creation of particulates matters from spray-wall interactions inside the combustion chamber [1, 2]. Also, for low-pressure injection systems such as urea based selective catalytic reduction (SCR), an increased penetration can cause unwanted solid deposit formation [3–5]. Those problems can be addressed by the flash-boiling atomization, which under proper conditions can promote shorter penetration, more uniform droplet size distribution, uniform mass distribution and wider spray angle for both high [6–9] and low-pressure injection systems [10–14]. From this perspective, flash boiling was intensively investigated last year by researchers.

Knowing the possible benefits of flash-boiling atomization, in this section the theoretical fundamentals of flash boiling are described. Next, based on the simplified categorization of phenomena implications into angle enhancement, spray collapse and droplet size reduction, a literature review is conducted to specify the current state-of-the-art.

1.1 Flash-boiling phenomenon description

Flash-boiling occurs when a liquid is injected into conditions with pressure below its saturation pressure. Figure 1 shows a schematic insight into a theoretical process referred to the liquid injection into a vessel at different backpressure that is below the saturation curve. At the initial state (point 1), the fluid is under injection pressure (P_{inj}) and fluid temperature (T_{fluid}). Then during the injection process the fluid is rapidly depressurized to the second state (point 2) from P_{inj} to P_{amb} crossing the saturation curve (point 1') and the liquid is in the metastable state called superheated. If the internal energy of the liquid is high enough that it cannot be dissipated by evaporation from the surface, the phase transition occurs inside the liquid [15, 16].

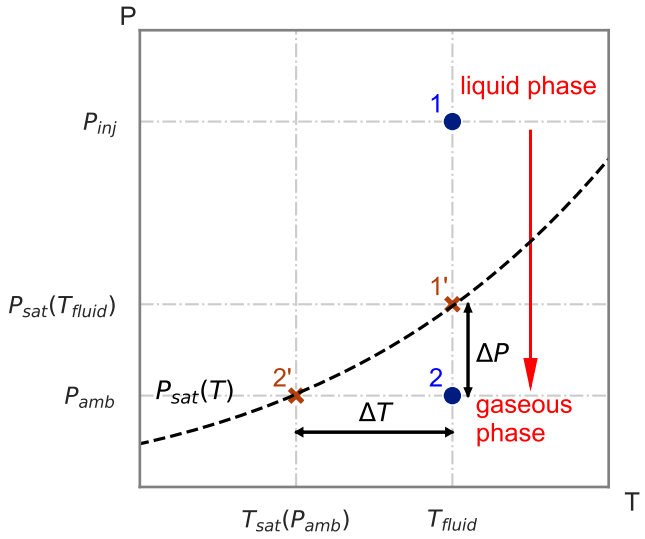

FIGURE 1: Schematic view on flash-boiling phenomenon and parameters for overheat description on $P-T$ diagram [16]

The superheat level, in literature, is mainly described through two parameters. The first one, degree of superheat (ΔT) is defined as the difference between the temperature of the liquid and its saturation temperature (T_{sat}) at ambient conditions (Fig. 1- temperature difference between states 2 and 2'):

$$\Delta T = T_{fluid} - T_{sat}(P_{amb}) \tag{1}$$

The second one is expressed by the pressure difference between equilibrium state $P_{sat}(T_{fluid})$ (point 1') and state at ambient conditions P_{amb} (point 2):

$$\Delta P = P_{sat}\left(T_{fluid}\right) - P_{amb} \tag{2}$$

Nevertheless, instead of ΔP very often, the ratio between saturation (point 1') and ambient (point 2) pressure is used, which is commonly denoted as superheat ratio (Rp):

$$Rp = \frac{P_{sat}\left(T_{fluid}\right)}{P_{amb}} \tag{3}$$

In the injection system, the vertical phase change as shown in Fig. 1 is obviously impossible, and the decompression is a rapid but continuous process which starts inside the nozzle. Figure 2 shows the schematic view of the flash boiling process based on Khan et al. [17]. As it can be seen, once the fluid flows through the nozzle, at some point, it crosses the saturation pressure, and the flash boiling is started. It can be described as a subsequent progression of nucleation, bubble growth, breakup by bubble expansion and evaporation [16]. Based on the experimental investigation of these processes, Oza and Sinnamon [18] suggested separation into two regimes for the flash boiling mechanism:

- an internal, where the growth of the bubble results in a two-phase flow inside the nozzle,
- an external, where the droplets are exploded due to rapid expansion of internal bubbles.

Both mechanisms induce a distinct change in spray structure, like enhanced cone angle, reduced droplet sizes and increased droplet velocity.

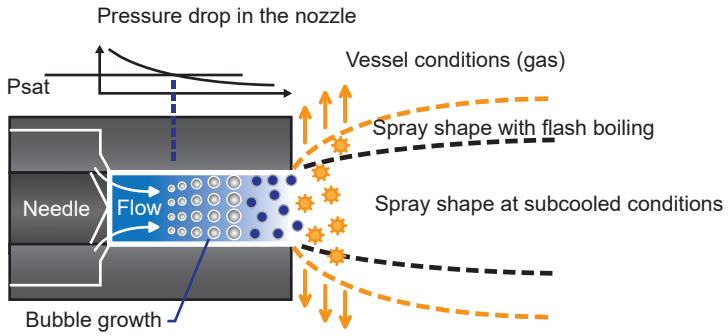

FIGURE 2: Schematic view on flash boiling process based on Khan et al. [17]

The nucleation process can be separated into two types, homogenous and heterogeneous (Fig. 3). In the first one, bubbles are generated in the whole volume of fluid (Fig. 3a). However, this type of nucleation hardly can be achieved except under precisely controlled laboratory conditions. In the second type of nucleation, the bubbles start to grow from the solid surface, as shown in Fig. 3b [19].

The homogenous nucleation can be described by a classical nucleation theory (CNT). Within CNT, a phenomenological approach estimates the nucleation flux by defining the critical work necessary to start nucleation. Thus, the number of stable vapour nuclei generated per unit of

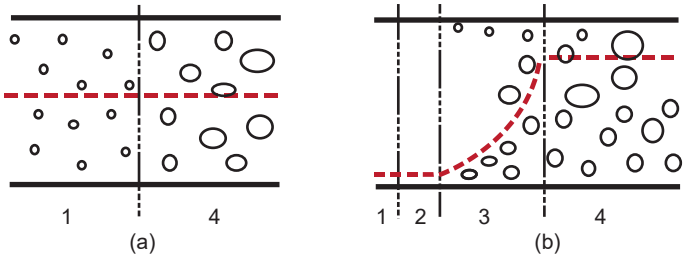

FIGURE 3: Schematic view on homogenous (a) and heterogeneous nucleation (b) based on Chang et al. [19]

volume and time J_{CNT} is proportional to [20]:

$$J_{CNT} \propto exp\left(-G_b\right) \tag{4}$$

where G_b- Gibbs energy for critical cluster formation:

$$G_b = \frac{4\pi\gamma {R_c}^2}{3k_B T_{fluid}} \tag{5}$$

where γ- surface tension, R_c- critical bubble radius and k_B - Boltzmann constant.

In a real scenario, a nucleation occurrence depends on the existence of appropriate disturbance, which leads to kinetic nucleation theory (KNT) with a kinetic limit for an infinitely fast process. Number of modifications in order to obtain KNT were introduced to the CNT. Among others, an estimation for realistic nucleation flux was introduced by Courtney [21] as:

$$J_{KNT} = \frac{1}{S} J_{CNT} \tag{6}$$

where S is described as:

$$S = exp\left(\frac{\Delta\mu}{k_B T}\right) \tag{7}$$

where $\Delta\mu$ is the difference between chemical potential at vapour and saturation state.

Nevertheless, as mentioned, heterogeneous nucleation will probably occur. In such a scenario, the nucleation rate is distinctly lower than for homogenous nucleation. Thus a reference to homogenous nucleation is done by the heterogeneity factor, which represents the level of homogeneity [20]. The literature shows a number of such correlations, for instance, created by Alamgir et al. [22] or Elias et al. [23].

Following the nucleation, bubble growth occurs. For flowing jets exiting from nozzles, this is a complex phenomenon, and the modelling approach is used to describe the bubble growth rate [24]. For instance, Kitamura et al. [25] proposed a model for flashing water and ethanol as

described below. The rate of bubble growth is given by:

$$R = \Phi Ja \left(\pi \alpha_T \Delta T\right)^{0.5} \tag{8}$$

where α is a thermal diffusivity and Ja is a Jacob number given by:

$$Ja = \frac{\rho_l C_p \Delta T}{\rho_{vap} h_{lv}} \tag{9}$$

where ρ_l and ρ_{vap} is density of liquid and vapour respectively, C_p is a heat capacity, h_{lv} is an enthalpy and ϕ is:

$$\phi = 1 - exp\left(-2.3\frac{\rho_{vap}}{\rho_l}\right) \tag{10}$$

The bubble growth itself is a subject of extensive studies, and other many other models can be found in the literature [26–31]. A common feature of all models is they are depended on thermodynamic properties of liquid and gas phase and also from superheat degree or superheat ratio.

As defined by Oza and Sinnamon [18], flash boiling can be separated into internal and external regimes, the bubbles' growth starts inside the nozzle resulting in a two-phase flow, but once the conditions for the external flash boiling are met the bubbles still grow inside the individual droplets outside the nozzle leading to the rapid droplet explosion. A schematic view of such a droplet breakup mechanism is shown in Fig. 4. Firstly, the bubbles grow inside the droplets to some critical extent when the droplet is destabilized. After that, the droplets are burst into smaller versions with additional velocity vectors.

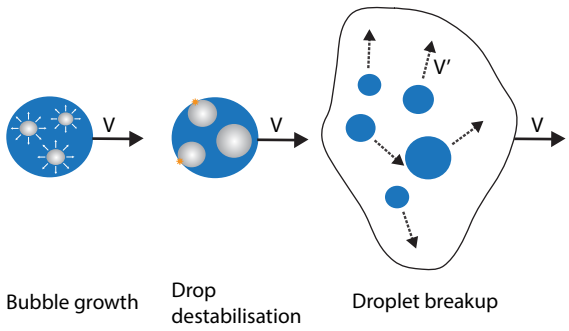

FIGURE 4: Schematic view of the droplet breakup mechanism for external flash boiling

Similarly to bubble growth, the droplet breakup mechanism is the subject of phenomenological modelling as the physical breakup mechanism is not well understood yet [29]. The important aspect of modelling the droplet breakup due to flash boiling is to model the boiling explosion time. Very often this time is defined by void fraction $\varepsilon = V_b/(V_b + V_l)$. For instance, Suma et

al. [32] assumed a void fraction between $0.51 - 0.53$, whereas Kawano et al. [33] applied 0.55. With the nucleation site density (in other words, the number of bubbles), new droplet size can be calculated based on the mass conservation law.

Within this section, the principles of flash-boiling atomization were shown. To sum up, this is a sequential process during which nucleation occurs due to rapid decompression. Then the generated bubbles start to grow, resulting in a two-phase flow through the nozzle, and finally, the flash-boiling atomization occurs. This phenomenon dramatically changes the spray structure. For the purpose of following literature review, these effects were categorized into three main groups: angle enhancement, spray collapse and droplet size reduction. Obviously, the flash boiling effects are much more than these three groups; however, suggested categorization properly underlines the study's scope and contribution.

1.2 Angle enhancement

As mentioned in the previous section, two-phase flow and droplet breakup due to the flash-boiling give droplets additional radial velocity, resulting in enhanced spray cone angle. The example of such a behaviour is shown in Fig. 5 with different spray patterns for increasing superheat ratio for acetone [34]. As it can be seen together with progressing superheat, the spray becomes wider, and the droplets are scattered over the wider area. This phenomenon can be especially interesting from a more uniform droplet spatial distribution point of view and has been widely investigated by researchers.

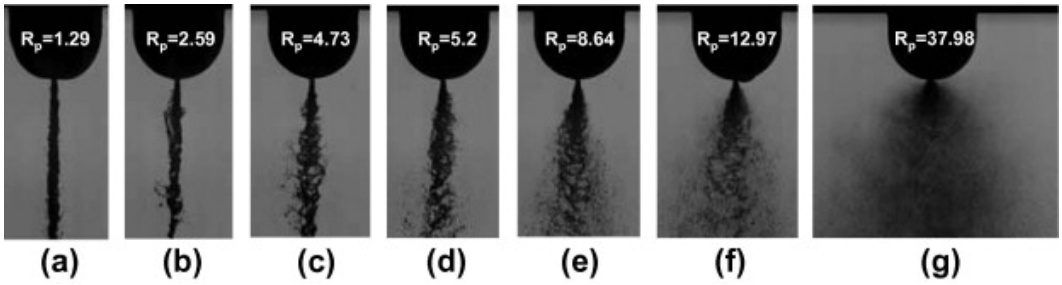

FIGURE 5: Spray angle widening for different Rp [34]

Oza and Sinamon [18] conducted experiments in a constant volume vessel for three different types of injectors (electromagnetic, pencil and a diesel poppet) and three different fuels (propane, methanol and Indolene). The ambient pressure was manipulated in the range of $0.35 - 21$ bar, and the injection pressure varied between 23.45 and 104.5 bar. Based on the results, they distinguished two regimes of flash boiling, the internal and external. In the first one, the bubbles grow within the injector's orifice from relatively low superheat degrees, which results in increased spray-tip velocity and improved atomization. The second one is due to the radial expansion of the jet outside the nozzle, which is a driver for spray cone angle increase. Also, it was observed that if the superheat degree is insufficient, the large droplets occur in the

middle of the injection cone. Senda et al. [35] performed an investigation on a constant volume vessel injected with *n*-pentane and *n*-hexane under 2.5 bar injection pressure and a constant temperature of 22 °C into a varying ambient pressure. For numerical modelling purposes, they found a dependence for angle enhancement as a function of the difference between backpressure and vapour pressure of fuel for both fluids independently. Zuo et al. [36] developed a model for angle enhancement for a hollow cone injector for numerical simulations. The researchers proposed a quadratic function correlating a superheat degree and nominal spray angle with a new cone angle caused by flash boiling. The model was calibrated to a gasoline fuel at 50 bar injection pressure. The analysis of isooctane injection by a GDI swirled injector at an injection pressure of 70 bar under different fuel temperatures ($20 - 120$ °C), and different ambient pressure (0.4 to 8 bar) was conducted by Araneo et al. [37]. For flash-boiling conditions, they observed a dramatic change in spray structure, the spray cone angle became wider, and this effect was intensified with a higher overheat ratio. Another work on isooctane was performed by Vieira and Simoes-Moreira [38]. The experiment was conducted under various injection pressures from 1.2 to 7.5 bar, temperature range from 56.4 to 178 °C, and backpressure from 0.25 to 6.1 bar. Based on the results, a trigonometric relationship of upstream and downstream velocities, thermodynamic properties and wave effects was proposed for spreading angle description.

Mojtabi et al. [39] carried out experimental work on a gasoline direct injector operating with gasoline at 120 and 200 bar pressure into a vessel with pressure ranging from 0.1 to 1 bar and fluid temperature between 20 to 100 °C. The tests were conducted on two different injectors, one with 60° and the second one with 90° of nominal cone angle. The studies revealed that together with ambient pressure decrease, the effect of angle widening could be observed, especially from 0.3 bar ambient pressure, at which this effect significantly increases. Serras-Pereira et al. [40] investigated the main factors that affect spray formation for GDI engine application. For this purpose, a special optical nozzle was designed to provide insight into the phenomena from the beginning. They tested three different fuels: gasoline, isooctane and *n*-pentane, for a range of injector's body temperature from 20 to 120 °C and ambient pressure from 0.5 to 1 bar. A similar observation at the near-nozzle region was noticed compared to macroscopic visualization. For each liquid, a significant improvement of atomization was observed in terms of enhanced spray angle. Kamoun et al. [16] carried out the experiments on a modified single hole automotive injector under fixed 10 bar injection pressure. Three different fluids, ethanol, acetone and isooctane, were injected into a vacuum vessel ($0.02 - 0.4$ bar) under different fluid temperatures ranging between $30 - 147$ °C. Based on the high-speed images, they defined spread angle metric at a different distance from the injector tip expressed as a ratio between distance and injector nozzle diameter. The study revealed that for a given distance from the injector tip, the spreading angles at different test conditions formed clearly separated curves as logarithm functions of superheat ratio, dimensionless surface tension [41] and molar mass. It was shown

that this dependence is valid for each fluid. Based on that, a polynomial function was suggested to model the spreading angle, and the model was verified against experimental data showing its capability to reflect the measurements. This study was later extended by Lamanna et al. [34]. Besides the correlation for spreading angle description, they directly linked it with the population of bubble clusters, proving the larger the cluster is, the wider the resulting cone angle. Also, they observed shock waves consistently for each fuel, confirming this is independent of the fuel's degree of retrogradicity (ideal-gas heat capacity at the critical temperature normalized by specific gas constant).

Arora et al. [42] tested in a heated constant-volume pressure vessel a six-hole GDI injector under various conditions of ambient pressures ($1 - 13.8$ bar), fluid temperature ($80 - 140$ °C) and fuel injection pressures ($34.4 - 207$ bar). They tested four different fuels, *n*-heptane, ethanol, ethanol blended with 15% isooctane and test grade E85. They showed that E100 and *n*-heptane formed a wider spray structure with a spread vapour region, while E85 blends formed a narrower spray structure. Aleiferis and Romunde [43] tested five different fuels, gasoline, isooctane, *n*-pentane, *n*-butanol, ethanol and *o*-xylene, under 20, 50, 90 and 120 °C fluid temperatures and 0.5 and 1 bar ambient pressure in order to reflect early injection strategies for part-load and open throttle operating conditions. The high-speed camera images showed a significant increase of spray cone angle due to flash boiling for each fuel. Also, it was pointed out that high volatility components had a clear impact on the spray atomization and comparing gasoline to ethanol, distinct differences in angle could be observed. Alloca et al. [44] realized an experimental work on gasoline sprays formed by a single-hole GDI injector. With the constant injection pressure of 100 bar, two ambient pressures of 0.5 and 1 bar and six different fuel temperatures (from ambient to 120 °C) were tested. They observed that with higher temperatures of the fuel, there are a noticeable recirculation wings with fine atomized droplets, also at flash-boiling conditions the jet cone angles increased and this effect is stronger for lower ambient pressure conditions. However, at flash-boiling conditions, from certain fuel temperature it's further increase did not affect radial and axial penetration.

Weber and Leick [45] investigated one- and two-holes GDI injectors supplied by *n*-heptane and gasoline to distinguish variations between single- and multi-component fuels. The tests were conducted for two different injection pressures, 50 and 200 bar, in various ambient pressures from 0.2 to 1 bar. The fuels were heated from 20 to 120 °C. The study showed that similarities between *n*-heptane and gasoline structures; however, a higher temperature needed to be applied to *n*-heptane since it's vapour pressure is lower than gasoline's. Similar to other researchers, the spray widening was observed at high pressure ratios, but increased ambient air entrainment into the spray plume was also noticed. Since tests were conducted at different injection pressure, it was revealed that for higher pressures the resulting spray angle is distinctly lower, what is not observed for mechanical breakup in non-flash-conditions. Moreover, it was stated that for a constant superheat ratio, the influence of flash boiling is lower at higher injection pressures.

Guo et al. [46] studied a single-hole GDI injector for *n*-hexane in a constant volume vessel in the ambient pressure range between $0.2-1$ bar. The injection pressure was fixed at 100 bar, and fluid temperature varied between $20-100$ °C. Based on the conducted experiments, the authors showed that the flash-boiling effect is not the only factor influencing the spray morphology in terms of external shape. A stable width was observed close to the injector tip despite the changing overheat ratio due to fluid temperature increase. This leads to the conclusion that this may be mostly the effect of lower ambient resistance. Also, it was pointed out that low overheat results in a slight change of spray width only, and a significant increase of radial expansion can be observed for distinct superheat degrees. In another work from Guo et al. [47], the research on single-hole GDI injector fuelled with *n*-hexane was conducted with similar conditions as previously [46]. Based on a high-speed camera measurements, they suggested to represent a jet width at different distance from injector tip in function of chemical potential difference and Naber et al. [48] correction to include the effects of ambient gas resistance. They assumed the flash-boiling effect is an isothermal process, and the chemical potential difference can be described as the difference between the liquid and gaseous phases. Such a data representation revealed that experimental results of jet width form a consistent curve on the graph; hence a universal function to describe the spreading angle can be proposed.

Wang et al. [49] performed a microscopic investigation of a near-field spray plume for 2-methylofuran, ethanol and isooctane at 400 bar injection pressure. The temperature range was between $20-80$ °C and the ambient pressure varied from 0.5 to 1 bar. The study showed that in the near field, the atomization is significantly improved for all fuels, resulting in wider sprays. Another near-field research was conducted by Li et al. [50]. In the study, a two-hole GDI injector was used under fluid pressure of 5 bar, ambient pressure from 0.12 to 2.5 bar and fuel temperature in the range of $30-85$ °C. The results showed that the flash-boiling effects had a stronger impact on a spray structure and expansion than cavitation for external sprays. It was shown again that lower ambient pressure can reduce the resistance for spray radial expansion. Moreover, a hypothesis was made that a greater cone angle is expected due to ambient pressure conditions than from the fuel temperature solely; nevertheless, such a temperature impact was also observed but to a lower extent. Zhao et al. [51] examined a near field angle for different fuels, isooctane, hexane, pentane and ethanol. The injection pressure was fixed at 200 bar, and the fuel temperature was set to 90 °C. In this case, the ambient pressure was adjusted to keep the constant overheat ratio for different fuels; hence it varied between 0.05 and 5 bar. For the near-field cone angle it was observed that each fuel undergoes a significant spray widening, but despite the constant overheat ratio, different fuels showed different angles. That was again connected with different ambient pressure resulting in different pressure resistance.

1.3 Spray collapse

Following the angle enhancement, another typical for flash-boiling atomization phenomena can occur. Spray collapse is an event when, the spray jets are dragged towards each other to extent that separate jets become one stream. The example showing flashing *n*-hexane sprays from single-hole and spray collapse at the same conditions from multi-hole injection was shown in Fig. 6 [47]. It can be seen that while a single hole injector follows the observation made in the previous section, the multi-hole injection start to collapse at middle overheat conditions ($T_{inj} = 90\,℃$ and $P_{amb} = 101\,kPa$). Based on this example, a three different states could be distinguish, spray formation under subcooled conditions ($Rp < 1$) where three different plumes are visible, collapsed flashing spray with reduced penetration for $Rp = 1.87$, and finally collapsed flashing spray with increased penetration observed for $Rp = 4.94$. This phenomenon and regimes were the subjects of extensive investigations in the recent years.

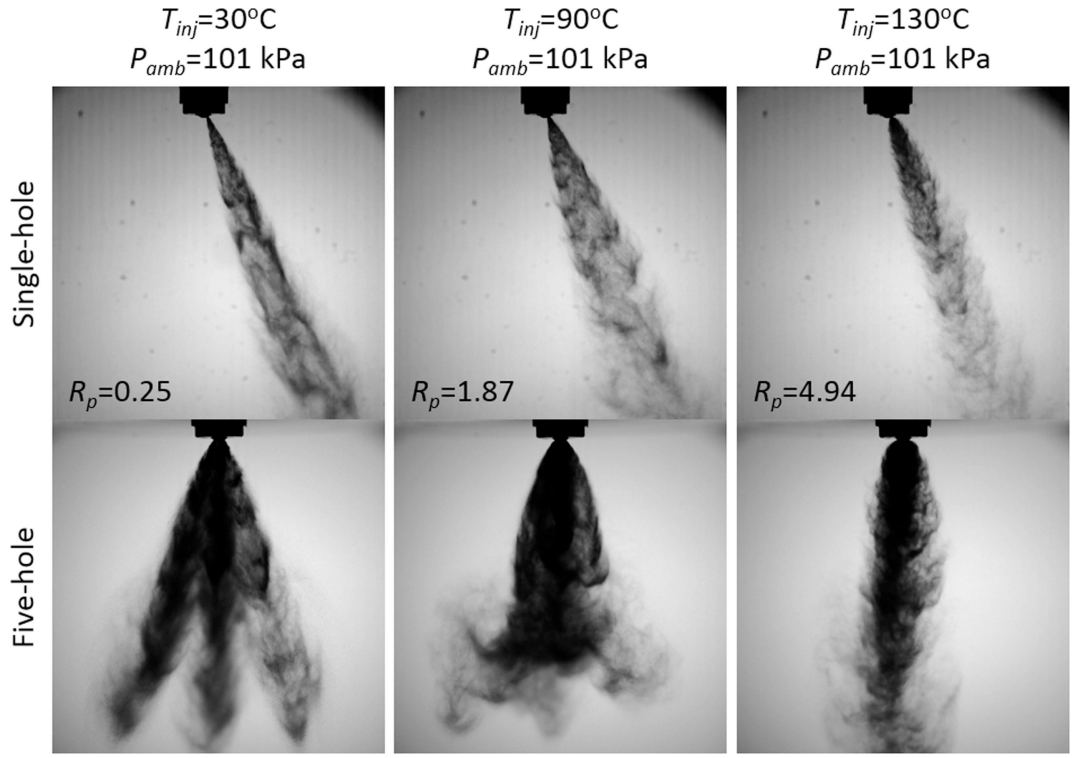

FIGURE 6: Spray collapse shown on comparison of spray morphology from a single-hole and multi-hole injectors [47]

Araneo et al. [37] performed analysis based on the experiment on isooctane injection by a GDI swirled injector at injection pressure of 70 bar under different fuel temperatures ($20 - 120\,°C$) and ambient pressures ($0.4 - 8$ bar). They observed as with increasing superheat level, the spray cone becomes wider near the nozzle but then falls to a rapid decay with further distance through the axis. This was explained as vortex activity which led to strong spray contraction and, as a result, faster spray tip penetration. Experimental wok on a GDI swirl and multi-hole injectors was carried out by Schmitz and Leipertz [8]. Three different fuels (*n*-hexane, isooctane and

n-octane) were injected under the pressure of 80 bar and varying fuel temperatures between $50-108\,^{\circ}\mathrm{C}$ into the bomb with 5 bar pressure. The study showed that, independently from the injector type, the spray contraction happened at the same conditions. As a possible reason for this state, a local pressure drop caused by a rapid drop in temperature was suggested.

Mojtabi et al. [39] carried out experimental work on two different gasoline direct injectors (60 and 90 deg of nominal angle) operating with gasoline at high injection pressure (120 and 200 bar) and different fluid temperatures ($20-100\,^{\circ}\mathrm{C}$). The ambient pressure varied between $0.1-1$ bar. The authors observed a collapse of streams towards the centre of the injection axis and the creation of the "tulip" structure with recirculation zones. Moreover, a distinct reduction in spray density under certain conditions was observed, suggesting an increased fraction of spray evaporated due to flash boiling. Again, a collapse was observed, and it was suggested that this is due to the interaction of individual plumes, which bent inwards by the interaction of vortices. Parrish et al. [52] tested GDI injectors (with different angle between nozzles) under 200 bar injection pressure with different fuel temperatures ($20-100\,^{\circ}\mathrm{C}$) and ambient pressure conditions ($0.4-1.2$ bar). They showed that for larger angles between the nozzles, the spray is more resistant to collapse, but once it is achieved, the spray shape remains similar independently from the angle. Zeng et al. [53] used *n*-hexane, methanol and ethanol fluids with 8-hole GDI injector (50 bar). The fluids were injected into a test bomb ($0.2-1$ bar) under various temperatures ($25-90\,^{\circ}\mathrm{C}$). The authors, based on a spray width measurements, suggested three different regimes for spray behaviour. The first one, is non-flash boiling conditions where the normalized width is constant. The second, for ambient-to-saturation pressure ratio between $0.3-1$, was called the transition regime, for which the spray width increases (independently from the fluid) until its maximum close to ambient to saturation pressure ratio of 0.3. At this point, the sprays collapse, and the third regime is defined where together with the increase of superheating, the spray cloud gets more collapsed. Those regimes also influence spray penetration, which for non-flashing conditions is constant, then for transition regime decreases, and finally for flare flash boiling again increases.

Zhang et al. [54] carried out the set of experiments for *n*-hexane injection from a multi-hole GDI injector (100 bar) for fluid temperature from 25 to $85\,^{\circ}\mathrm{C}$. The ambient pressure was adjust between $0.2-0.4$ bar. As expected, together with the superheat level the spray collapse gradually progresses until the flare flash boiling. In line with previous researchers, the authors indicated a pressure imbalance between the inside and outside the cone as reason for such a spray behaviour. Also, it was noticed that spray collapse is a transient process, at the beginning the spray plumes remained separated; however, the vapour component already collapsed to the centre line, then after some period of time spray plumes also collapsed. Finally, it was discovered that after the spray collapse a vaporization rate increased rapidly. The effect of injection pressure on flashing sprays in optical accessible, single-cylinder SI engine was evaluated by Chan et al. [55]. The fuel was injected under different pressures ($40-150$ bar) into

a cylinder with two injection timings 90 and 300 crank angle degrees after top dead centre to simulate a low and high ambient pressure scenario. It was shown, that spray collapse effect can be suppressed by the injection pressure, as for the highest injection pressure, the spray cones maintained their direction, while for lower conditions, the spray collapsed. Huang et al. [56] published the study on gasoline and ethanol at various temperatures from 3 to 127 °C injected into a constant ambient pressure of 1 bar under the injection pressure equal to 60 bar. The authors showed that spray collapse occurred for lower overheat level that was defined in [53], due to a much lower angle between nozzles. They concluded that it was another factor that needed to be taken into account when analyzing the spray collapse.

A detailed study on spray collapse was performed by Kramer et al. [15]. The authors conducted a systematic study with different backpressures ($0.3-1$ bar) and fuel temperatures ($30-95$ °C). As fuels, RF-02-08 (legislative fuel, Euro 5 gasoline) as a reference for gasoline and the single-component alkanes: *n*-pentane, *n*-hexane, *n*-octane and *n*-decane were used. The injection pressure for each case was kept constant and equal to 200 bar. Based on the study, it was shown that the collapse effect could also be achieved in non-flashing conditions by the increase of number of holes. A jet-to-jet interaction was indicated as a reason for the spray collapse. The spray widening was observed as independent from the fuel and always occurred at the same saturation to ambient pressure ratio. Moreover, the authors indicated the possibility of controlling the collapse effect through the geometrical design of the injector. Wu et al. [57], for a comprehensive collapse explanation, investigated a one-, two- and six-hole injector with two length to diameter nozzle ratio, fuelled by hexane. The injection was operated under the high pressure (150 bar), with fuel temperatures in the range of $20-85$ °C and ambient pressures between $0.2-2$ bar. The results showed that the shorter nozzle led to a narrower spray plume. This was found as a contradiction to other studies [58]. The authors explained this as an effect of quick expansion of the spray after emerging from nozzle, what resulted in hitting the wall of the counter bore, while for longer nozzle only very little fuel hit the wall. For the number of hole effect, it was quantitatively showed that 2-hole injector produced wider spray plumes comparing to one-hole, for all tested conditions. This can be connected to the different local pressure at orifices, as it is higher for one-hole injector, what is in line with previously shown study by Chan et al. [55]. A strong collapse effect was observed for the 6-hole injector, for which a schematic process was proposed. As long as the spray plumes are separated, the flow between the inner and outer parts of the spray cloud is free, and the pressure is almost identical. Once the inner part is closed by connected plumes, due to the widening of the spray angles, pressure imbalance is created, causing the collapse.

Araneo and Donde [59] focused spray collapse in terms of near (0.1 mm from injector tip) and far field angle ($20-30$ mm from injector tip). The authors tested different single-component fuels (*n*-hexane, *n*-heptane and isooctane) and multicomponent fuels (three different types of gasoline with known aromatic content and one with unknown). The fuels ($30-110$ °C) were

injected under a constant injection pressure of 100 bar into a vessel ($0.4-1$ bar). The study revealed that with an increased superheat level, the near-field angle increases while the far-field angle is opposite due to the collapse effect. Importantly, those observations were consistent for each fluid to the extent that the results of near- and far-field angles converged to one line in function of saturation-to-ambient pressure ratio. This observation led the authors to a method for a saturation pressure curve calculation for fuel with unknown content of aromatics. For this fuel, the inverted calculations were done, hence from the near-field angle a theoretical saturation pressure was calculated. Guo et al. [60] discussed two different modes of spray collapse based on a research on gasoline injection (fuel temperature of 20, 80 °C) by 5-hole GDI injector (injection pressure of 100 bar) into a various ambient conditions (pressure of $0.5-10$ bar). It was observed that for elevated ambient pressure the spray collapsed in the near field (<10 mm), while in the further distance, it expanded. In the flash-boiling induced collapse, the observations were opposite; the near-field spray was expanded, while the far field collapsed drastically. Based on this, the authors proposed two mechanisms for spray collapse, jet- and condensation induced for ambient pressure and flash-boiling, respectively.

Lacey et al. [61] tested isooctane and propane ($30-90$ °C) injected by GDI injector (at 200 bar) into a constant-volume vessel at different pressures ($0.36-1$ bar). The experimental results, showed that the pressure ratio lacks generality to describe the collapse effect fully. They proposed a new parameter, stream tube expansion ratio, which is specific to the injector geometry and thermodynamic states, and defines a spray collapse when exceeds 1. The authors considered this new criterion valid for different fuels, other injectors and set of fuel rail conditions. Closely-coupled split injection strategy effects on spray collapse were investigated by Wang et al. [62]. Fuel, isooctane ($20-100$ °C) was injected (150 bar) by 6-hole diesel injector into a vessel with $0.2-1$ bar pressure. The study showed that a split injection strategy could be a vital solution for increased spray penetration due to spray collapse, which was a major drawback for engine applications. Li et al. [63] conducted a comprehensive work on understanding the collapsing effect for multi-hole injectors. Gasoline ($20-120$ °C) was injected into various ambient conditions ($0.2-10$ bar) under the 100 bar injection pressure. For flare flash boiling, an inner structure of the collapsed spray consists of the condensation core and a blob near the nozzle exit. The collapse itself was explained as the outcome of vapour condensation caused by a rapid temperature drop and pressure change due to radial expansion. In similar conditions, *n*-hexane was tested by Li et al. [64]. The study showed that ambient pressure could have two basic effects on developing a flash-boiling and spray collapse. The first is connected to the ambient gas resistance and aerodynamic forces, while the second is controlling the superheat degree. A low ambient pressures, the produced vapour and droplets can disperse faster, thus the local concentration is limited and the resultant low pressure zone in the inner side of spray is reduced hence also a collapse weaker. This is opposite for higher ambient pressures. Guo et al [47] for *n*-hexane under different temperatures ($30-130$ °C) injected under the pressure of

100 bar into the vessel with various pressure conditions ($0.2 - 1$ bar) suggested the relationship between the expansion of a single jet and the collapse effect. It was found that individual jet width and spray collapse are positively correlated. As a method for spray collapse mitigation, an injector realizing the eternal expansion of droplets was proposed.

Jiang et al. [65] investigated the impact of 5-hole and 6-hole GDI injector (200 bar) on a spray morphology and its implications on optical engine performance under different injection timing ($330 - 180$ crank angle degrees before top dead centre). The detailed near- and far-field visualization were done in order to capture the difference in spray collapse effect. It was shown that the 5-hole injector plume structures are more resistant to collapsing than the 6-hole injector, which is in line with previously discussed literature. Since the droplet size of both injectors was similar, the spray structure itself had an impact on the combustion process. The 5-hole injector provided a better mixing resulting in faster combustion with higher temperature peak, and elevated NOx emissions. Also, particle number (PN) emissions were lower due to better atomization. In another study, Jiang et al. [66] investigated the influence of nozzle geometry on the spray structure under the flashing conditions. For this purpose, a fuel (gasoline at 30 and 90 °C) was injected (at 100 and 200 bar) into different backpressure conditions ($0.3 - 1$ bar) by injectors with different nozzle configurations. The study showed that the middle-size hole diameter gave the best resistance to the spray collapse, which could be further improved by applying divergent holes.

Li et al. [67] carried out tests in a constant-volume vessel with ambient pressures ranging from 0.6 to 11 bar and fuels (propane, *n*-hexane and isooctane) at a temperature from 30 to 110 °C. The injection pressure was constant for each case and equal to 100 bar. Based on the study, the threshold (above which the spray did not collapse) for propane collapse was found between 1 and 3 bar of ambient pressure. The root cause of this effect was explained as higher ambient pressures suppressed the nucleation and bubble expansion inside the nozzle what resulted in collapse resistance effect. Moreover, the high vapour production via surface boiling could counteract the low-pressure tendencies created by high-speed jets. Hollow cone injectors under flash-boiling conditions were studied by Wang et al. [68]. The injection pressure was equal to 80 bar, and ambient pressure varied between $0.01 - 1$ bar. As a fuel isooctane was used with range of $25 - 125$ °C. It was observed that due to flash boiling, a hollow shape expanded inwards and outwards. Eventually, the inward expansion is merged resulting in very distinct spray stream thrust in the middle of the hollow shape, which greatly passed the main shape. Under certain conditions, this stream can reach 200 m/s and the flash boiling starts to be dominant creator of the spray structure. Thus, as multi-hole injector collapse could be described as a bell-shaped, the hollow-cone collapse can be described as "mushroom" or "umbrella" shaped with a distinct round zone in the upper part and a long stream in the middle of injection axis.

Another comprehensive study on multi-hole GDI injector was conducted by Wu et al. [69]. A fuel (*n*-hexane at a temperature range of $25-85\,^{\circ}\mathrm{C}$ and injection pressure of 150 bar) by 1- and 6-hole injector into the ambient conditions of $0.2-2$ bar. The authors observed than even slight plume interactions led to a shortened penetration, which with the increased superheat level led to a spray collapse. Basing on this analysis, an extended view on air flow between the spray plumes was suggested as a main reason for the spray collapse. The previous findings about the plume-to-plume interaction were confirmed by Xu et al. [70] in the study on two-hole injector working under 350 bar injection pressure. In their study, *n*-pentane ($20-290\,^{\circ}\mathrm{C}$) was injected into a vessel with various pressure (0.15 and 1 bar). The study showed that plume-to-plume interaction is intensified by the superheat level, which can be suppressed by a higher injection pressure, different nozzle configuration or higher ambient pressure. The subject was further explored by Du et al. [71] in a study on a 10-hole GDI injector (100 bar) fuelled by isooctane ($60-120\,^{\circ}\mathrm{C}$) and ambient pressures from 0.04 to 2.45 bar. For such dense injector's holes distribution the observed structure for high overheat is similar to the collapsing spray produced by a hollow cone injector, with the difference that the upper part is a bell shaped. This work was extended by the research on spray structure using time-space tomography [72]. The work confirmed previous findings about the spray structure in a more detailed 3D analysis.

Chang et al. [73] investigated different injector's hole arrangements, in terms of the inclination angle, in order to obtain improved injector design for combustion engine applications. For this purpose *n*-heptane ($60-180\,^{\circ}\mathrm{C}$) was tested under 100 bar injection pressure in a vessel with pressure varying between 0.2 and 1 bar. The study revealed that the spray with a higher inclination angle promoted a larger evaporation rate, due to larger plume spacing. This is pointed out as a possible room for GDI spray design improvement for flash-boiling injection strategy. A further work on improving a plume-to-plume interaction, and a collapse effect was shown by Liu et al. [74]. They tested different types of single-component fuels (isooctane, hexane, pentane) and their binary mixtures in various fluid temperature conditions (70 and $90\,^{\circ}\mathrm{C}$) and ambient pressure conditions ($0.1-2.5$ bar) under the 200 bar injection pressure. The authors proposed a new transition to a collapse criterion based on the fuel properties, ambient conditions and nozzle geometry, which is valid for single- and multi-component fuels.

The findings for high-pressure injectors were evaluated in a detailed analysis of spray collapse for low-pressure injection in study by Kapusta [12]. The test conditions covered a various fluid temperature conditions ($60-160\,^{\circ}\mathrm{C}$) under a two different injection pressures (5 and 7.5 bar) and ambient atmospheric conditions for two- and six-hole injector. The study showed that similarly to high-pressure injection systems, the higher number of holes induces an earlier collapse effect in terms of overheat progressing. Nevertheless in contrary to the high-pressure systems, the flash boiling effect did not lead to penetration increase. The author indicated that due to breakup mechanism for subcooled conditions, low-pressure injectors produced relatively large droplets with high momentum and penetration, for which aerodynamic forces are minor.

Therefore, even with a high additional momentum caused by the flash-boiling atomization, the superheated spray will not propagate faster than in subcooled condition since the droplets are significantly reduced.

1.4 Droplet size reduction

Lastly, as described earlier, the droplet size reduction is happening due to flash boiling. This literature review focused on the droplet size quantification for different liquids and test conditions rather than on modelling aspects.

Park and Lee [75] conducted an experimental study on a water injection by a transparent, single-hole injector under different pressures of $2-4.35$ bar and various fluid temperatures ($110-144\,^{\circ}$C).The authors analyzed droplet size distribution and Sauter mean diameter (SMD), and based on that it was revealed that for higher overheat ratio the droplets became smaller but also radial distribution of SMD is more flat, what pointed out on more uniform distribution. Based on those observations, it was stated that with increasing overheating, the internal flow regime changes from bubbly to slug and finally to annular flow. For modelling purposes, Senda et at. [35] measured SMD for on *n*-pentane and *n*-hexane under 2.5 bar injection pressure and constant temperature of 22 °C at various ambient pressures. They observed that for subcooled conditions, the SMD is nearly constant. It has a maximum value when the ambient pressure equals to fluids saturation pressure due to large droplets formation from contracting spray, and then it rapidly decreases together with an overheat increase. Araneo et al. [37] investigated the effect of fuel temperature on the droplet size in a GDI swirled injector. The fuel, isooctane, was injected into a quiescent environment (pressure $0.4-8$ bar) under 70 bar injection pressure. The temperature of the fluid varied between $20-120\,^{\circ}$C. Based on a phase Doppler anemometry (PDA) measurement at 15 mm and 30 mm from the injector tip, the authors showed a distinct decrease of SMD at several radial locations. However, a minor influence of ambient pressure and liquid temperature was reported.

Schmitz and Leipertz [8] conducted experimental wok on a high-pressure multi-hole injector for GDI engines. The droplet size distribution of *n*-hexane sprays was measured for the injection pressure of 80 bar and fuel temperatures between 50 and 108 °C and ambient pressure of 5 bar. The study showed that due to flash boiling the droplet size can be reduced by about 30-40%. Lecourt and Barricau [76] performed experimental work for rocket engine propellants in vacuum conditions. They injected ethanol, acetaldehyde and monomethyl hydrazine under pressure between $1.7-18.6$ bar into near-vacuum conditions ($0.3-13.1$ kPa). Based on the results, the authors proposed an empirical correlation for SMD in the function of non-dimensional superheat for two different types of injectors. Also, an empirical sub-model for predicting SMD from subcooled to flash-boiling conditions was proposed by Cleary et al. [77]. They conducted the

experimental work on water sprays formed under injection pressure between 2 and 20 bar and fluid temperature between $130-180\,^{\circ}\mathrm{C}$ in atmospheric conditions. Park et al. [78] investigated characteristics of dimethyl ether under 600 bar injection pressure, various ambient conditions (ambient pressure: 1, 15 and 30 bar, ambient temperature: 20, 77 and $127\,^{\circ}\mathrm{C}$) and different fluid temperatures (20, 57, $97\,^{\circ}\mathrm{C}$). The study showed that SMD had an almost uniform value, regardless of the ambient pressure. However, SMD increased while the ambient temperature was increased, at the same ambient pressure. This effect was connected to faster evaporation of smaller droplets. Flash-boiling for heavy fuel oil and water emulsions was characterized by Kim et al. [79]. They investigated different emulsions of heavy oil and water injected at various temperatures ($87-147\,^{\circ}\mathrm{C}$) under 6.9 bar injection pressure into atmospheric conditions. It was shown that the micro-explosion of emulsion caused by the flash boiling is more effective in improving the atomization than the reduced viscosity.

The comparison between droplet characteristics obtained at highly elevated injector pressure and by the flash-boiling atomization was conducted by Sens et al. [7]. They investigated gasoline under the injection pressure from 180 to 1000 bar and fluid temperature from 20 to $350\,^{\circ}\mathrm{C}$. The results showed that thanks to the flash boiling atomization, the SMD can be about 25% smaller when rising the temperature from 25 to $200\,^{\circ}\mathrm{C}$, than if rising the injection pressure from 180 to 350 bar. It was also measured that injection pressure can be lowered to 50 bar while thanks to the flash boiling the droplets were still sufficiently fine. Wen et al. [80] conducted research on the assessment of flash boiling for pulse detonation engines. The authors heated JP-8 fuel to $100\,^{\circ}\mathrm{C}$ and injected it into ambient conditions. The injection pressure varied between $10-130$ bar. The results showed a distinct particle sized distribution shift towards lower sizes for heated fuel. Also, they showed that the SMD spatial distribution is more uniform in case of overheated fuel. Aleiferis and Romunde [43], for simulated early injection strategies for part-load and open-throttle operating conditions, tested five different fuels (gasoline, isooctane *n*-pentane, *n*-butanol, ethanol and*o*-xylene) under 20, 50, 90 and $120\,^{\circ}\mathrm{C}$ fluid temperatures and 0.5 bar and 1 bar ambient pressure. For each fuel, the reduction of SMD in the function of fluid temperature was observed, but with different rates due to different saturation temperatures of fuels. Also, the difference in droplet sizing was observed in terms of ambient pressure resistance.

Kamoun et al. [81] performed droplet size measurements for flashing methanol. The tests were conducted in medium-vacuum conditions ($0.02-0.4$ bar) under a low injection pressure (not specified) with fluid temperature up to $116\,^{\circ}\mathrm{C}$. As was expected, the mean droplet size decreased with the superheat level. The authors proposed a correlation based on classic nucleation theory for a mean diameter (error below 2.85%); however, the correlation was shown only for three data points. Xu et al. [9] tested gasoline, ethanol, methanol and *n*-hexane with injection pressure between 30 and 150 bar. The fluids were injected at various temperatures ranging from 25 to $90\,^{\circ}\mathrm{C}$ into a constant volume chamber with pressure in the range of $0.2-2$ bar. Based on

the SMD measurements, the authors showed that the difference in SMD, observed for different injection pressures, decreases with the superheat level until it reaches a quasi-stable value. This means that with the superheat level, the influence of injection pressure on atomization decreases. Based on the observation, the three different regimes were proposed to describe the flash-boiling atomization. The first one, non-flashing region for ambient to saturation pressure ratio above 1, where there is a distinct constant difference between SMD produced at different injection pressures. The second one, transitional regime for ambient-to-saturation pressure ratio between 0.3 and 1, where the SMD was reduced for both injection pressures but reduction rate was higher for the lower injection pressure. The last one, flare flash boiling region for ambient-to-saturation pressure ratio below 0.3, with constant difference of SMD. This is generally in line with the previous findings for spray collapse regimes [53].

Van Vuuren at al. [13] investigated the influence of flash-boiling conditions on a low injection pressure (5 bar) of urea-water-solution atomization in the stationary conditions. The study showed that this form of atomization can be also beneficial for urea-based selective catalytic reduction systems. The research was extended to superheated urea-water injection into a hot airflow to simulate diesel exhaust-like conditions [14]. Shen et al. [82] provided a detailed droplet size measurement in various spatial positions in a spray cloud. The authors tested different fluids (gasoline, *n*-pentane, *n*-hexane, *n*-heptane) under the injection pressure of 50 bar, fuel temperature $20-110\,^{\circ}\mathrm{C}$ and constant ambient pressure of 1 bar. The authors analysed the droplet size distribution at different radial and axial positions from the injector tip. It was found that for non-flashing cases a relatively large droplets can be observed at the spray periphery and spray tip. Also, a proportion of large droplets increase with the distance from the injector tip. For transitional flash-boiling state, the SMD is decreased twice and the large droplets are observed in the middle of the spray cloud. Finally, at flare flash-boiling state even faster decrease of SMD was observed.

Liu et al. [83] performed tests on a single-hole gasoline spray for different fuel temperatures ($25-376\,^{\circ}\mathrm{C}$), various injection pressures ($60-140$ bar) and constant ambient -atmospheric conditions. Based on droplet size histograms, it was shown how the high temperatures, and the resulting flash-boiling atomization, can shift the whole distribution towards smaller droplet sizes. Also, 1 and 10 percentiles of the largest droplets were analysed, and it was shown that thanks to flash atomization, big droplets can be completely eliminated. Wang et al. [62] tested isooctane in flash- and non-flash boiling conditions with a 6-hole DI injector under the 150 bar injector pressure for single and split injection strategies. The test matrix covered ambient pressures from 0.2 to 1 bar and fuel temperatures from 20 to $100\,^{\circ}\mathrm{C}$. The study showed that the split injection strategy leads to larger droplets for all considered conditions. As possible reasons, a lower effective pressure and transient state of split injection were pointed out. Yang et al. [84] examined flash boiling effects for multi-component fuels in near nozzle sprays. The authors tested a transparent single-nozzle injector with gasoline-surrogate fuels consisting of

n-pentane, isooctane and *n*-decane in various proportions. The fuel was injected under constant pressure equal to 50 bar into atmospheric conditions. The fuel temperature varied between $59-143$ °C. The results showed that the addition of high-volatility fuels induced a higher level of flash boiling in the near-nozzle region of the spray.

The study showing the effects of flash-boiling atomization on low-pressure injection (5 bar) for water and urea-water-solution was showed by Kapusta et al. [11]. The fluids were injected into the atmospheric conditions under various fluid temperatures ($60-143$ °C). The study showed the systemic decrease of droplet size as the superheat level increased, which was pointed out as a potential method for improving atomization in urea-based selective catalytic reduction applications [10].

Atac et al. [85] investigated the influence of initial flash-boiling spray formation at the same superheat level, differencing fluid temperature ($60-145$ °C) and ambient pressure ($0.08-1$ bar) independently for high-pressure (200 bar) 6-hole GDI injector. The authors showed that for the same superheat level a distinctly lower SMD is obtained by increasing the fluid temperature than lowering the ambient pressure. This effect was related to the possible influence of lowered fuel viscosity at higher fluid temperatures, but also increased ambient resistance and resulting aerodynamic shear and drag forces for elevated ambient pressures. Yan et al. [86] used pure isooctane, hexane and ethanol and their binary mixtures to establish the effect of high volatility content in the mixture on the droplet sizes. The injection was performed under pressure of 200 bar by a 8-hole GDI injector. The fluid temperature was constant (90 °C) and the ambient temperature was varied from 0.22 to 1 bar. Based on the SMD and arithmetic mean diameter comparisons, it was shown that ethanol, a high latent heat fuel, results in the largest droplet sizes among single component fluids; while the addition of 10% of ethanol to isooctane could effectively lower the number of large droplets. This study was used for a validation of numerical model for droplet breakup by Gao et al. [87]. Chang et al. [88] investigated two GDI injectors with different holes with *n*-heptane under 100 bar injection pressure. The tests were performed at two different fuel temperatures (20 and 120 °C) and constant ambient pressure equal to 1 bar. The study showed that under flash-boiling conditions the spatial SMD distribution was more uniform, as the SMD standard deviations decreased.

Li et al. [89] showed the impact of spray evaporation on droplet size characteristics under flash-boiling conditions. They used a single-hole GDI injector fueled with pentane under various temperatures ($20-156$ °C). The liquid was injected into a vessel with various pressures ($0.05-1$ bar). The injection pressure was constant and was equal to 350 bar. The authors observed that the SMD is significantly impacted by the evaporation during the spray propagation. The SMD increased with the distance from injector tip, which indicated evaporation of smaller droplets. This leads to the conclusion that SMD alone may be insufficient to describe the whole phenomena, and liquid-volume composition flux was proposed as a supplementary

metric. Also, Li et al. [63] conducted a study on gasoline ($20-120\,°C$) injected into an ambient conditions ($0.2-10$ bar) under the injection pressure of 100 bar. They discovered that under high superheat level a bimodal droplet size distribution can be observed as a possible result of condensation. Zhao et al. [51] performed tests to evaluate the influence of fuel (isooctane, hexane, pentane, ethanol) properties and aerodynamics forces on spray atomization under flash-boiling conditions. An 8-hole GDI injector under 200 bar injector was used for this purpose, the fluid temperature was constant at 90 °C and ambient pressure was varied from 0.1 to 5 bar. The study revealed that the aerodynamic forces played an important role in a droplet breakup, as pentane had a largest aerodynamic breakup level. Also, since ethanol has the higher latent heat of vaporization, it resulted in the highest SMD.

1.5 Contribution of the thesis and hypothesis

In the previous chapter, the extensive literature review was shown to draw the current state-of-the-art in flash-boiling atomization to give a background for this dissertation. The literature showed a significant effort made by researchers in the description of spray angle enhancement, spray collapse, and droplet atomization due to the flash-boiling effect.

It was shown that due to the rapid expansion of the jet, the initial spray angle becomes wider with increased overheat level. Despite the fact that the effect of flash boiling is considered as a dominant driver for angle enhancement, it was shown that other factors such as ambient resistance, fluid temperature, injection pressure and injector geometrical parameters can play a minor but distinguishable role in angle formation. As for the spray collapse, it was widely investigated that it is induced by plume-to-plume interaction as a consequence of angle spreading. Therefore, similarly to angle enhancement, this effect can be different depending on the ambient conditions, fluid temperature, injection pressure, bore shape, and nozzle geometrical parameters and number of holes. Lastly, for a droplet size reduction, it was shown that flash boiling can greatly improve atomization and can be considered as an alternative to elevated injection pressure, to promote smaller droplets. The review also showed that a primary mechanism of droplet reduction is a micro explosion, but remaining effects of fluid temperature and ambient pressure conditions are still important.

Based on the conducted literature review, it can be seen that there are no studies regarding the influence of flash-boiling effect on a shape of statistical droplet size distribution under various overheat conditions. Until now, vast majority of the qualitative analysis of droplet size reduction due to flash boiling was done in terms of the mean droplets size metrics as Sauter mean diameter or arithmetic mean diameter. The statistical droplet size distributions were reported but no direct link between flash-boiling parameters and probability distribution function was provided. Such an analysis can be especially important for low-pressure injection, as droplet sizes can be

dispersed over a wide range of sizes from 10 to ~300 μm [90–96]. The consideration of only mean metrics could be misleading, as this does not bring any information about shape of sizes' probability distributions function like for instance skewness. In addition, the literature review shows that the investigations for low-pressure injectors ($<$ 10 bar) are the minority, and among those studies there is a lack of full spectrum of test conditions in terms of fluid temperature and ambient pressure controlled independently, as it was done for high-pressure injectors [85]. Therefore the direct influence of these parameters has not been reported yet for low-pressure injectors. This is especially important since many studies for higher pressures revealed that despite the fact that flash boiling is the main cause of structural spray changes, the ambient conditions and fluid temperature can distinctly influence the process, as was shown for spray angle [45, 46, 50, 51], spray collapse [60, 64] and atomization [43, 78, 85]. Thus, the conditions that cover both fluid temperature and ambient pressure change are needed to fully analyse the process.

The above considerations reveal a knowledge gap which is the understating of flash-boiling effect on droplet size distribution in terms of how the overheat level affects the droplets diameters in whole size spectrum in low pressure sprays. To make the conclusion more universal, this influence should be assessed by controlling flash boiling by both, the ambient pressure and fluid temperature. This gap is aimed to be filled within this work, which led to the hypothesis that the droplet size distribution, in terms of both the average parameters and its shape is systematically changed by the intensity of flash boiling and it can be modelled as a function of a superheat parameter.

Chapter 2

Materials and methods

As it was underlined by the hypothesis, the scope of this work is to understand the influence of flash-boiling intensity parameters on droplet size distribution in various ambient pressure and fluid temperature conditions. This was done by systematically conducted experiments followed by the data analysis. In this section the materials and methods of experimental part are described. This is organized as follows; firstly, based on liquid temperature and ambient pressure, a test matrix is discussed and the purpose of such a test design is explained. Secondly, the experimental set-up is discussed in the context of gathering the necessary data using laser-optical methods for spray visualization. Next, there is also a supplement to the experimental set-up describing the set of liquid temperature-calibration tests, which were conducted due to the indirect fluid temperature measurement. Finally, the test methodology and metrics are discussed. This contains the explanation of test procedures including, data post processing and metrics which are used in the dissertation to analyse the results.

2.1 Test matrix

The tests were conducted on water at various temperatures and ambient pressures in both non-flash and flash-boiling conditions. Figure 7 shows operating conditions described by ambient pressure and fluid temperature, the green line depicts the saturation pressure of water, which was calculated according to the Antoine's equation:

$$log_{10}P = A - \frac{B}{T+C} \tag{11}$$

where P- vapour pressure (mmHg), T- temperature (K).

Coefficients A, B and C were selected according to the NIST database [97]. The operating conditions were divided into three groups (Fig. 7) to distinguish different parts of investigation. Group 1 and 2 represents non-overheated conditions to check how the fluid temperature and ambient pressure can affect a spray itself, separately from the overheat ratio. To check the influence of ambient pressure on spray behaviour the group 1 was investigated, where three

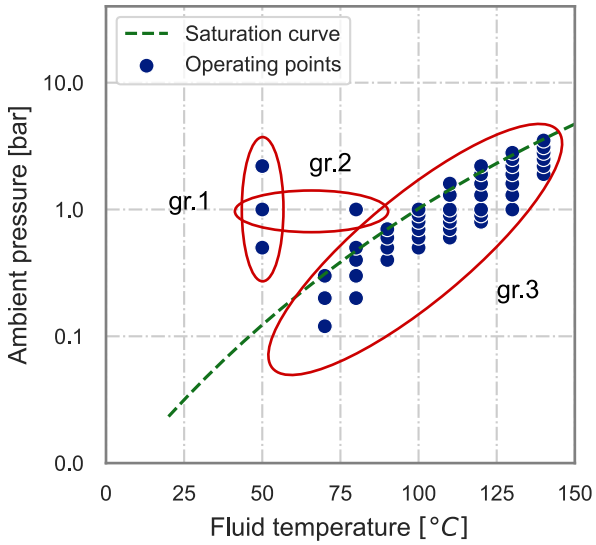

FIGURE 7: Ambient pressure and fluid temperature of tests condition; group 1- subcooled conditions at constant injection temperature and various injection pressures; group 2- subcooled conditions at constant pressure and various fluid temperatures; group 3- flash-boiling conditions

different ambient pressures (0.5, 1, 2.2 bar) were tested at constant water temperature (50 °C). Also, to assess the effect of fluid temperature a group 2 was investigated, where two operating points can be found at different injection temperatures (50 and 80 °C) and the same ambient pressure equal to 1 bar. Group 3 contains all operating conditions that were used to assess the effect of flash boiling and to perform a droplet size model creation. The tests were conducted at 8 different temperatures of injected liquid, from 70 to 140 °C with 10 °C increment step. The ambient pressure was adjusted to keep the operating conditions under or close to the saturation curve. In other words, the flash boiling occurs at each condition. Also, the ambient pressure was adjusted in order to operate in the similar range of superheat ratio (Rp). This is shown in Fig. 8, where superheat degree (ΔT) is plotted against superheat ratio (Rp). It can be seen that ΔT is between $\sim 0-30$ °C, while Rp varies between $\sim 1-2.6$. The limit for the ambient pressure adjustment was $Rp < 3.33$, since this value in many studies is indicated as the maximum for transitional flash boiling [9, 53]. All tests together gave 50 different operating points, where group 1 had three, group 2- two cases, and finally group 3- forty five cases.

2.2 Experimental set-up

The experiments were designed to measure the droplets at different overheat conditions of injected fluid. To do that, the shadowgraph method was used and the experimental set-up was designed to control both, the fluid temperature and ambient pressure. A schematic diagram was shown in Fig. 9. The injector with cooling jacket is mounted in the pressure vessel. The temperature of the investigated fluid is controlled by the circulating oil through the cooling jacket,

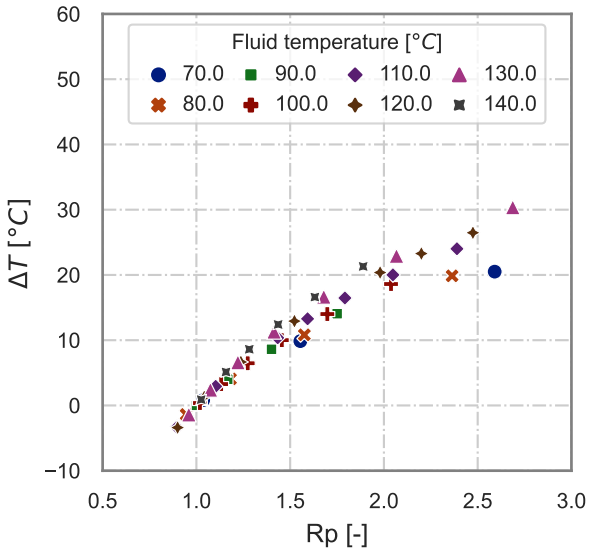

FIGURE 8: ΔT and Rp in analysed group 3

while the oil temperature is controlled by the circulator (Huber Kiss K6) within the range of $20 - 200\,°C$. The fluid is supplied to the injector from the liquid tank pressurized by the nitrogen. The injection pressure is controlled manually based on the pressure gauge indication. Depending on the pressure inside the pressure vessel, the injection pressure was adjusted in order to keep the constant pressure difference (between injection and ambient pressure) of 5 bar. The injector is mounted in the pressure vessel that can be both pressurized or decompressed by the compressor or vacuum pomp depending on the setup. Thus, the pressure inside the vessel could vary between $0.05 - 10$ bar. Such a design allowed to obtain various range of superheat level controlled by two independent parameters: fluid temperature and ambient pressure.

For the droplet size measurements a shadowgraph set-up based on the Nd: YAG laser (Spectra Physics Quanta-Ray Pro-230). The 532 nm beam was used to excite the dye in the diffuser, The generated light (574-580 nm wavelength) going through the diffuser optics illuminated the spray. On the other side a camera (LaVision CMOS) with long-distance microscope was placed to record the pictures. The field of view was setup to visualize the area of 5 x 5 mm of the spray. The optical access was obtained by two quartz windows mounted at the opposite sides of the vessel. Due to the dimension constrains, the injector tip was placed above the edge of the windows; however, the goal of the study was to characterize the spray cloud in the fully developed region, hence the optical access to the injector's tip was not necessary. A similar experimental set-up, in terms of the optics, was previously validated and used to characterize droplets in number of works conducted by Kapusta et al. for low pressure injectors in non-flash conditions [93, 96] and also in flash-boiling conditions [10, 11].

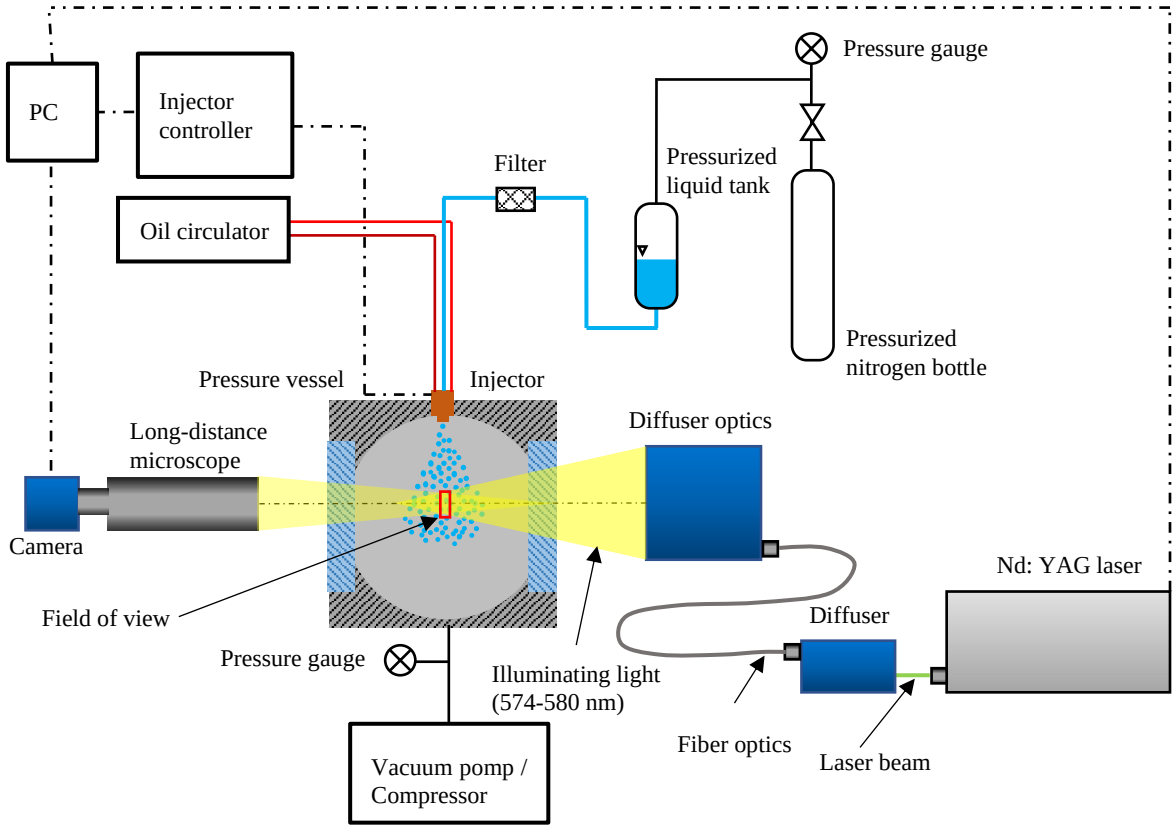

FIGURE 9: Experimental setup. Blue solid line - injected liquid; red solid line - heating circuit; black solid line - pneumatic system; black dashed line - electrical hardware connection

The camera, injector and laser were synchronized by a computer with LaVision Davis 8.4 software. The laser was working with 10 Hz frequency. The camera and the injector were synchronized in such a way that pictures were captured 10 ms after the start of injection. The signal from the computer triggered the injector driver which controlled the injector voltage at 12V and opening time of 15 ms. This setup allowed to measure droplet sizes in fully developed spray clouds.

The injector used in the experiments was a 3-hole low-pressure type injector designed for AdBlue® application. A hole diameter is equal to 150 µm distributed by 120° over the circle with a diameter at hole centre position equal to 2.32 mm. According to the data provided by the injector manufacturer that injector has a static flow of 1.16 g/s, and the global spray visualisation angle of 23.6°, while the individual spray plums are the full cones. Finally, the Sauter mean diameter is equal to 68 µm. The parameters which describe a spray cloud characteristics: static mass flow, spray angle, Sauter mean diameter were measured at 5 bar gauge pressure. It is also worth to note that these parameters can fluctuate due to deviations in series production. The injector parameters were listed in Tab. 1.

TABLE 1: Injector parameters (spray parameters shown for 5 bar gauge pressure)

Parameter	**Value**	**Unit**
Number of holes	3(1)*	-
Hole diameter	150	µm
Diameter at hole canter position	2.32	mm
Circumferential distribution	120	deg
Static mass flow	1.16	g/s
Spray angle visualisation	23.6	deg
Spray type	full cone	-
Sauter mean diameter	68	µm

*only one hole was used in this study (the other two were plugged)

For testing purposes two holes (of three) of the injector were physically plugged; hence, only one nozzle was working. This was made to avoid a multi nozzle interaction and the collapse effect of overheated spray, which was widely reported for high-pressure injectors [47, 53, 55, 57, 60, 69, 98, 99], but also applies to low-pressure injectors [11, 12]. The injector was positioned so the only working plume was perpendicular to the optics set-up. In Fig. 10 a picture of the injector was shown to give better overview on the experiment. The injector has the cooling jacket with the inlet from the bottom side to ensure that the circulating oil is flowing upstream the injected fluid. The fluid is supplied through the perpendicular tube located at the top of the injector.

FIGURE 10: The injector used in the study

2.3 Fluid temperature calibration

Since the temperature of the liquid inside the injector was controlled indirectly via oil circulating in the cooling jacket, there was a need to determine the dependency of liquid temperature in function of the oil temperature. Following the methodology performed by Kapusta et al. [11], the additional temperature calibration tests were conducted in order to meet temperature demands in test matrix (Fig. 7).

Figure 11 shows the calibration set-up. A 0.2 mm junction diameter, bare thermocouple J type was placed about 1 mm below the injector tip. The tip of the thermocouple was placed directly in the liquid plum in its unbroken part. In order to obtain a function of fluid temperature depending on oil temperature a several temperatures of oil from 50 to 100 °C with a 10 °C step were tested. Since, the calibration was conducted in the atmospheric conditions, the temperature was limited by the boiling point. Additionally, for each temperature, different injection frequencies of 1, 2, 5, and 10 Hz were tested, to assess the thermocouple response at different frequencies.

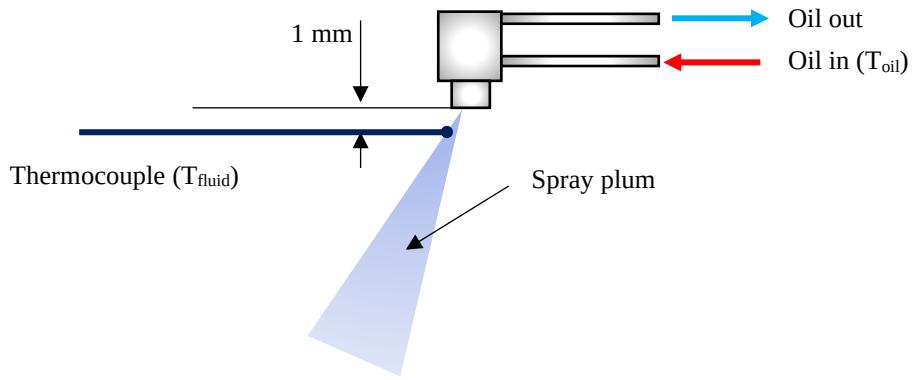

FIGURE 11: Temperature calibration set-up

Figure 12 shows the whole set of conducted measurements. The injection duration was equal to 15 ms, and the whole measurement last 10 s. It can be seen that independently from the oil temperature the characteristics are similar. At each condition the fastest response was observed for 10 Hz injection frequency. Also, at this condition there is the highest temperature peak and the lowest amplitude. Those trends systematically changes with the injection frequency. The amplitude and response time are increasing and the highest temperature peak decreases, when the frequency is lowered. Moreover, it can be seen that 10 Hz temperatures tend to decrease over the measurement time, while 2 and 5 Hz remains constant as well as 1 Hz (after the initial increase at the beginning of the measurement). Based on the injected fluid temperature characteristics it was decided to assume that the fluid temperature can be estimated by the highest indication of measured temperature, as it is the closest to the actual fluid temperature inside the injector before the injection.

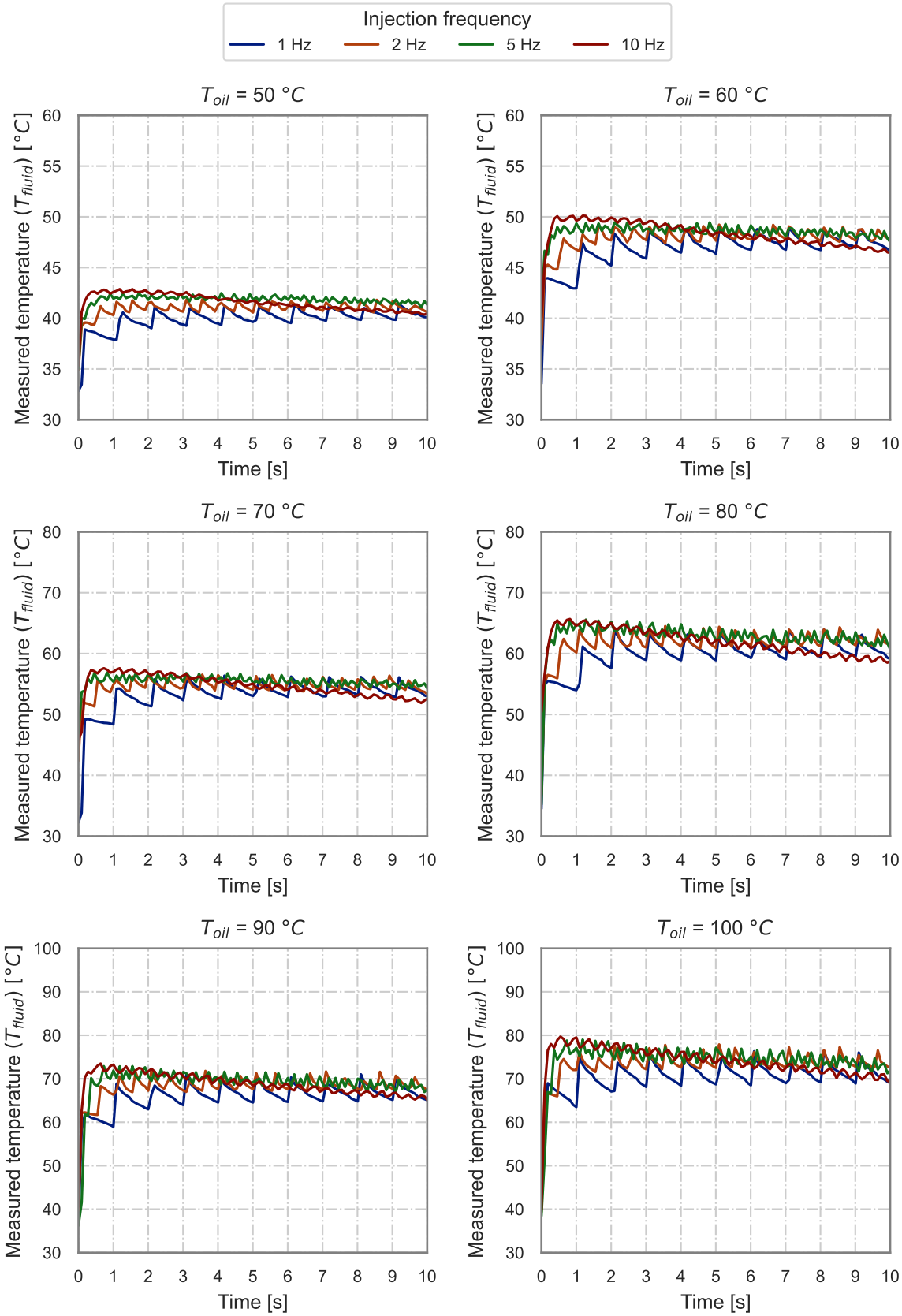

FIGURE 12: Measured water temperature (T_{fluid}) for different injection frequencies and oil temperatures (T_{oil})

The questionable in this assumption is a temperature decrease during the measurements. Nevertheless, the testing procedures for droplet sizing assumed that only 20 injection were performed during the single measurement, what gave 2 s duration of single test (this is explained later on in 2.4 Test methodology and metrics section). Thus the effect of the temperature drop was minimized. The results of the temperature calibration are listed in the Tab. 2.

TABLE 2: Temperature of oil and water (measured)

Oil temperature (T_{oil}) [°C]	Measured water temperature (T_{fluid}) [°C]
40	36
50	42.9
60	50.1
70	57.6
80	65.7
90	73.5
100	79.7

In order to obtain a function, which describes the oil temperature depending on the desired temperature of the liquid inside the injector, the polynomials regressions were fitted into the data from Tab. 2. The temperature of water was denoted as T_{fluid}. Figure 13 shows the scattered data from Tab. 2 with fitted linear and quadratic regressions. It can be seen that both functions were fitted with high coefficient of determination (R^2), which are 0.9989 and 0.999 for linear and quadratic functions respectively. As it can be seen, the functions are overlying for the investigated temperatures range (from Tab. 2); however, a substantial difference can be seen at extrapolated range. The difference between the functions for the highest desired liquid temperature from the test matrix (140 °C) equals to 9.12 °C. As along with higher temperatures a more intensive heat loss can be expected, and also due to a slightly better coefficient of determination, it was assumed that quadratic function should be used to calculate the required oil temperatures. The function is given by:

$$T_{oil} = 1.515e-03 \cdot T_{fluid}^2 + 1.147 \cdot T_{fluid} - 1.607 \tag{12}$$

2.4 Test methodology and metrics

The droplet sizes measurements were conducted based on shadowgraph images. At each condition shown in test matrix (Fig. 7), the whole set of images was taken. The droplets were measured and the lists of droplet sizes and their positions were created for each operating condition. The detailed procedure is described within this section.

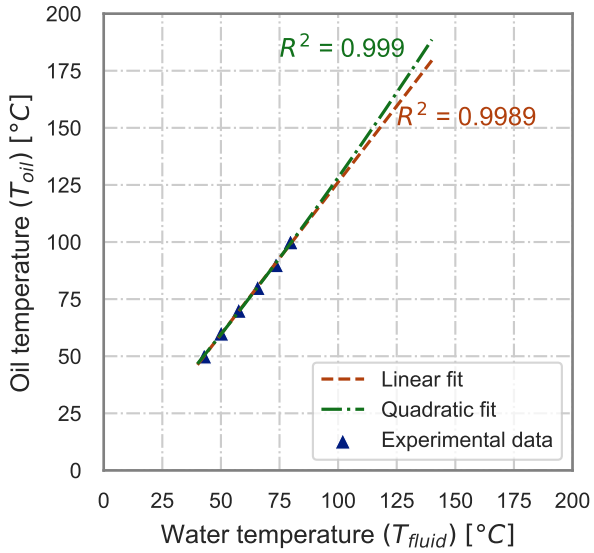

FIGURE 13: Oil temperature set (T_{oil}) against the desired water temperature

Firstly the optics calibration was made based on the calibration plate. Figure 14 shows the picture of the calibration plate. The calibration plate is a transparent board with different sizes of black dots. In this case the biggest dot is 200 µm and the smallest one is 10 µm. Next, based on this image the software postprocessing constants were calibrated in order to capture these sizes.

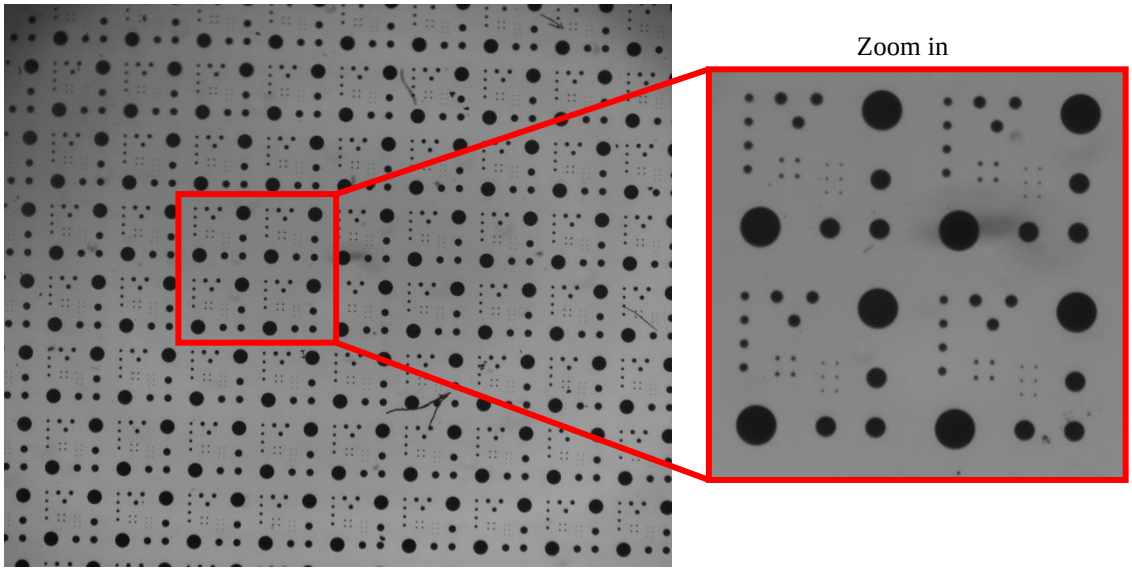

FIGURE 14: Image of calibration plate. The range of dots' sizes are 10-200 µm

Figure 15 shows an example of single image taken for water at 50 °C injection temperature and 1 bar of ambient pressure. As this is a real life scenario it cannot be expected that produced droplets will be as regular as on calibration plate. It may happen that captured droplet will be of irregular shape or out of the focus droplet will partially overlay with the droplet in the

focal plane, which on the 2D picture look like "connected" (example shown in Fig. 15). Such the artefacts are difficult to interpret by the picture processing algorithms and very often are treated as one big elliptical droplet what leads to misinterpretation by changing a droplet size characteristics significantly, especially if a volume of droplets is concerned. A common way to avoid that is to not include those artefacts in the statistics; therefore, in post processing it was limited that eccentricity of such droplets cannot be higher that 200%. Moreover, it can also happen that two or more droplet are so close to each other that during the postprocessing they will be treated as single droplet with a distinctly higher diameter. To avoid this kind of situation, the upper limit of recorded droplet size was set to 300 µm, while for lower sizes it is partially solved by the eccentricity limit.

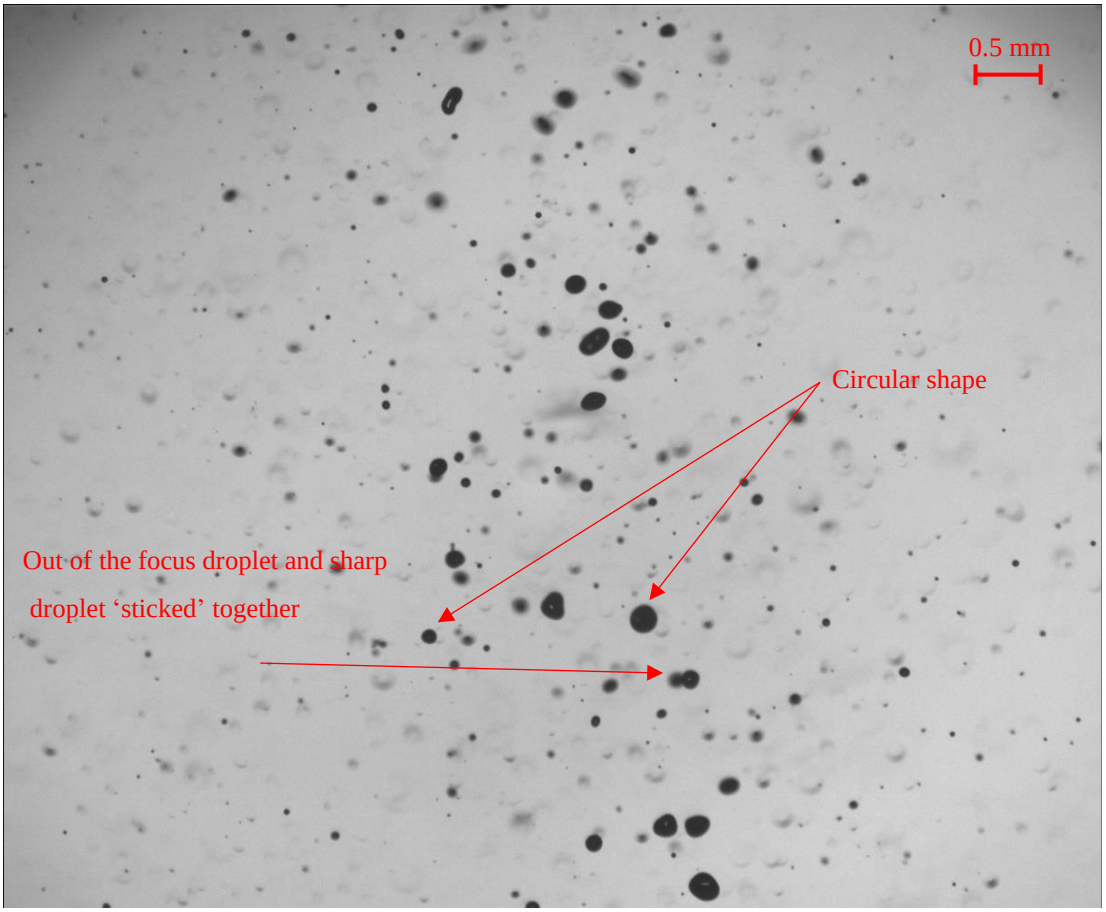

FIGURE 15: Image of water injection droplets at $T_{fluid} = 50\,°C$, $P_{amb} = 1$ bar

For each test condition 100 images were captured to obtain a sufficient number of droplet to perform a proper analysis. However, to capture 100 images at 10 Hz injection frequency the test need to be 10 s long. Since it rises a problem with maintaining the constant temperature of the injected fluid, what can be observed in Fig. 12, the set was divided into 5 subsets of 20 images (single subset duration 2 s). Between each subset a pause was done to recover the temperature. It was also observed that after maximum 25 images there was a need for flushing

and cleaning the vessel. For each set of 100 images a number and volume-based distributions were calculated with 5 µm resolution. The example of the probability density function (*PDF*) and cumulative distribution function (*CDF*) for the test conducted for water at $T_{fluid} = 50\,°C$ and $P_{amb} = 1$ bar are shown in Fig. 16. It can be seen that number based *PDF* are more skewed towards lower diameters, as there is naturally more smaller droplets detected. Such characteristic will not give a full understanding of spray structure, as the information about the mass is hidden. Therefore, to reveal this information, a volume-based *PDF* was calculated according to the following formula:

$$P_V(d_i) = \frac{d_i^3 \cdot P(d_i)}{\sum\{(d_i\} \cdot P(d_i))} \tag{13}$$

where d_i is a droplet diameter, $Pv(d_i)$ is a probability for d_i.

It can be seen that the volume-based representation (Fig. 16) is shifted to the right compared to the number based. The droplet diameters that seemed to be minor in the number based histogram (> 100 µm), are playing a significant role in the volume-based distribution. Within this study, the focus was put on the volume-based characteristics, as this brings information about mass distribution over the droplet sizes; hence, each *PDF* and *CDF* graphs are referred to it from now on.

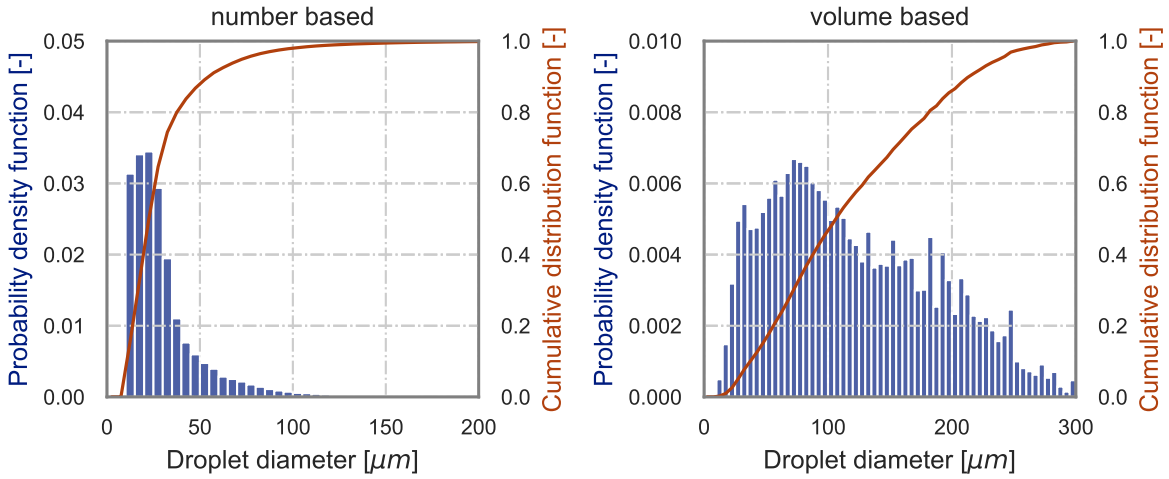

FIGURE 16: Number (left) and volume (right) based statistics; probability density function (left axis) and cumulative distribution function (right axis) at operating conditions $T_{fluid} = 50\,°C$, $P_{amb} = 1$ bar

Besides a direct comparison of droplet size distributions, the spray cloud is very often described by the parameters based on cumulative distributions. In this study 10^{th}, 50^{th} and 90^{th} percentiles of distributions were used to compare the spray characteristics, this is namely: *Dv*10, *Dv*50, *Dv*90. Another parameter to compare spray droplets characteristics is a Sauter mean diameter

(SMD or D_{32}), which is defined according to:

$$SMD = D_{32} = \frac{\sum d_i^3 (d_i)}{\sum d_i^2 (d_i)} \tag{14}$$

Chapter 3

Results and discussion

In this section, the results are discussed. Firstly, the influence of ambient pressure and injected liquid temperature on droplet sizes in non-flash-boiling conditions are shown. This is followed, by the analysis of the superheat influence on spray droplet size characteristics. Lastly, there is an analysis of possibilities of modelling droplet probability distribution as a function of different overheat parameters and the model for it is suggested.

3.1 Influence of ambient pressure and fluid temperature in non-flash-boiling condition on droplet size distribution

To assess the effect of fluid temperature and ambient pressure on non-overheated spray, the tests were conducted separately at fixed fluid temperature (Fig. 7- group 1) and fixed ambient pressure (Fig. 7- group 2). For the pressure impact, the temperature T_{fluid} was set at 50 °C, and the ambient pressure was 0.5, 1.0 and 2.2 bar, sequentially. The results of the test were depicted in the form of $PDFs$ and $CDFs$ in Fig. 17. Generally, it can be observed that for

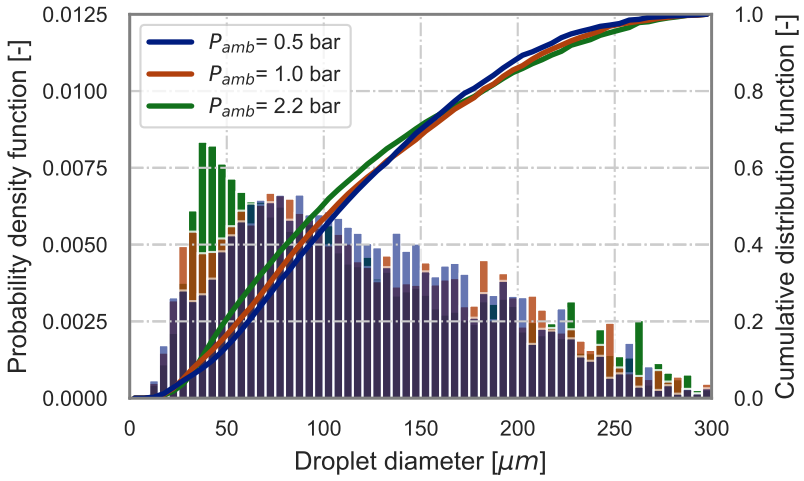

FIGURE 17: Volume based probability density functions and cumulative distribution functions for water at $T_{fluid} = 50$ °C and different ambient pressures

the highest ambient pressure (2.2 bar) the distribution is the most positively skewed, while this trend lowers together with decreasing ambient pressure. What is more, it can be seen that $CDFs$ are crossing each other approximately at 150 µm, and at the left side of graph (droplet diameter < 150 µm) corresponding percentiles are smaller for higher ambient pressures. It means that smaller droplets are promoted at increased ambient resistance. This is opposite at the right side of the graph (droplet diameter > 150 µm) where bigger droplets are promoted at lower ambient pressures.

Based on this conclusion and on the graph itself it can be said that distributions are substantially different. To confirm that, a two-tailed Kolmogorov-Smirnov ($K-S$) test for testing distributions' similarity was conducted between each pair of experimental conditions [100, 101]. The null hypothesis was that two data sets come from the same distribution. The results of the test are shown in Fig. 18 as a matrix of p-values, which describe probability of obtaining test results at least as extreme as the result actually observed, assumping that the null hypothesis is correct. As can be seen, each pair of data has p-value close to 0 which is much below a significance level (0.05), hence according to the $K-S$ test the null hypothesis should be rejected, confirming that the distributions are substantially different.

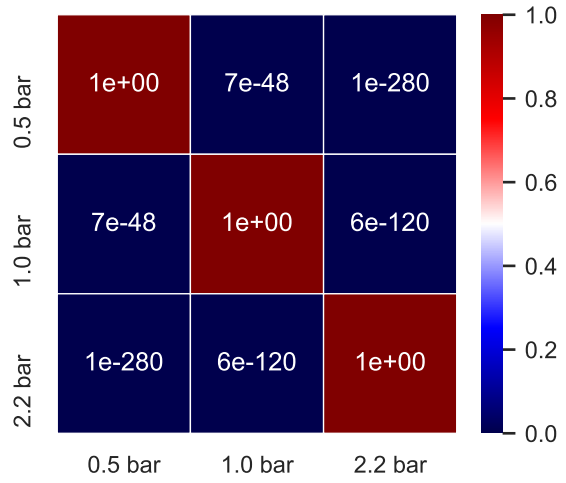

FIGURE 18: P-value matrix for water at $T_{fluid} = 50\,°C$ and different ambient pressures

If one looks closer at the metrics (Fig. 19) it can be seen that trends are systematic over the ambient pressure change. As it was previously shown on cumulative distribution graphs, at higher pressure the smaller droplets are promoted. The differences between the extreme cases in $Dv10$ and $Dv50$ are 6.8 µm and 10.9 µm respectively. For bigger droplet the trend is opposite, and $Dv90$ decreases together with pressure with a maximum difference equal to 14.4 µm. Also, what is not directly seen $PDFs$ and $CDFs$ graphs, D_{32} follows the trend set by $Dv10$ and $Dv50$. It slowly decreases with the ambient pressure elevation up to maximum difference equal to 6.4 µm.

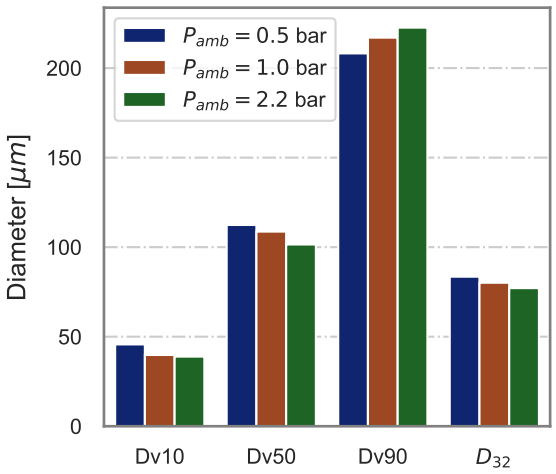

FIGURE 19: Droplet size's metrics for water at $T_{fluid} = 50\,°C$ and different ambient pressures

Similarly to the ambient pressure effect, the fluid temperature effect on droplet sizing in subcooled conditions was investigated. Since the liquid temperature directly affects parameters as surface tension, viscosity and others, it influences the droplet sizing. In order to assess that, the experiment was conducted for 50 °C and 80 °C, the ambient pressure was kept constant at $P_{amb} = 1$ bar.

Figure 20 shows probability density functions and cumulative distribution for the abovementioned cases. For this comparison, the difference in skewness hardly can be assessed, but a substantial difference in tail shape (groups of larger droplets) can be observed. For the lower temperature, the tail of the distribution contains distinctly higher probabilities of occurrence. This can be also observed at the cumulative distributions. Up to about $70-80$ µm both curves

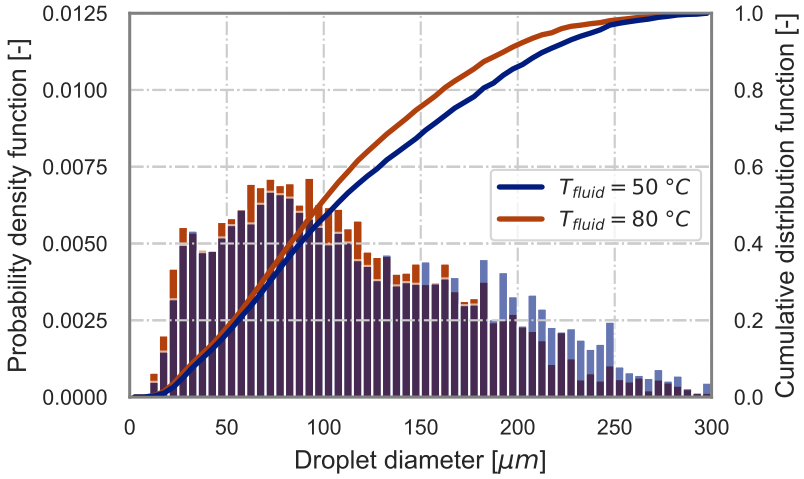

FIGURE 20: Volume based probability density functions and cumulative distribution functions for water at $T_{fluid} = 50\,°C$ and 80 °C at $P_{amb} = 1$ bar

are practically overlayed, while above those droplet size lines diverges,and higher fluid temperature promotes smaller droplets in the upper range of sizes. Here, in contrary to the ambient pressure influence on sizes distributions, the trend is consistent in whole range of droplet sizes, and the lines do not cross.

With the similar methodology as for ambient pressure influence assessment, $K-S$ tests were conducted for both cases to assess if the null hypothesis of distributions equality can be rejected. The test showed p-value ~ 0, hence according to the $K-S$ test the null hypothesis should be rejected, confirming that the distributions are substantially different, as it was also calculated for the ambient pressure influence.

Figure 21 shows the main metrics of droplet distribution for discussed cases. As it was seen at *CDF* graphs the difference between metrics increases with their magnitude. If $T_{fluid} = 50\,°\text{C}$ is treated as a base case, for $T_{fluid} = 80\,°\text{C}$ the reduction in $Dv10$, $Dv50$, $Dv90$ and D_{32} is 6%, 7.5%, 10% and 7.1% respectively. It shows that especially for bigger droplets a significant reduction is observed, which proves that despite the same ambient conditions fluid temperature induces distinct changes in droplet size distribution formation.

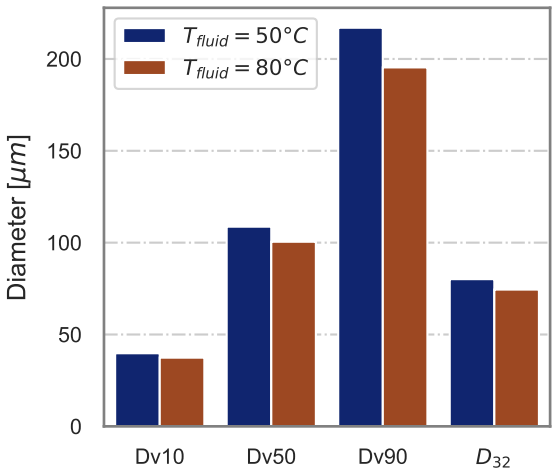

FIGURE 21: Droplet size's metrics for water $T_{fluid} = 50\,°\text{C}$ and $80\,°\text{C}$ at $P_{amb} = 1$ bar

In this section it was shown that both ambient pressure and temperature of injected fluid have a clear impact on the droplet sizes in subcooled conditions. This is understandable since both parameters directly influence driver parameters for atomization. The ambient pressure is strictly connected to the density of the surroundings; hence also affects aerodynamics forces that act on the spray from the beginning of the injection processes. For instance, for the conducted tests on ambient pressure influence, the pressure varied from 0.5 bar to 2.2 bar what according to the ideal gas equation results in respective density variations. Moreover, to keep the same pressure difference between the injector and in the vessel, the absolute pressure inside injector is also varied. While for the higher injection pressures (assume: above 100 bar pressure difference) a

2 bar increase of absolute injector pressure is only 2%, for low-pressure injector (for example 4 bar difference), the same elevation is the increase of about 50%. As for the temperature of injected liquid, it can affect the jet breakup according to four Reitz regimes [102] by Ohnesorge [103] and Weber [104] numbers, since the temperature changes viscosity and surface tension.

The same effects are expected for flash-boiling conditions. Despite the fact that in this scenario a main driver for atomization is a rapid boiling, the influence of ambient pressure and liquid temperature can also play a significant role in the process of droplet formation. Therefore, in the following study for flash-boiling conditions, both parameters are variable and are systematically changed to provide a wide spectrum of pressure-temperature conditions, since controlling only one parameters could gave incomplete view on the study and conclusion.

3.2 Influence of flash boiling on droplet size distributions

In this section the influence of flash boiling on droplet size characteristics is discussed based on the analysis of conditions defined as group 3 (Fig. 7). As it was mentioned, this group contains all tests that fluid was injected at the border or in fully-flash-boiling conditions for different fluid temperatures and ambient pressure. The cases at the transitional conditions ($\Delta T \sim 0\,^{\circ}\mathrm{C}$, $Rp \sim 0$) were treated as a baseline for the droplet reduction assessment.

Following the discussion started in the previous section, the operating conditions with same superheat ratio (Rp) but for different values of T_{fluid}, will differ in ambient pressure. To keep constant Rp, the ambient pressure needs to be elevated or decreased according to the saturation pressure of liquid for the particular fluid temperature. This means that despite the theoretical constant level of overheat liquid temperatures and ambient pressure can be different. Figures 22 and 23 show a comparison of droplet size distributions for approximately equal values of $Rp =$ 1.4 and 2.05 respectively. It can be seen that despite the same level of superheat ratio the droplet size characteristics are different. It can be noted (Fig. 22) that the fluid temperature varies between 90 °C and 130 °C, and ambient pressure from 0.5 to 1.9 bar respectively, so the conditions are distinctly different. Cumulative distributions are crossing each other above $Dv50$, in the way that for higher fluid temperature and ambient pressure smaller droplets are promoted above $Dv50$, while below this value it is opposite. In Fig. 23 the fluid temperatures are 100 °C, 110 °C and 130 °C while the corresponding ambient pressures are 0.5 bar, 0.7 bar and 1.3 bar. Again, the conditions are substantially different in terms of T_{fluid} and P_{amb}. In this case the characteristics are different, however, they do not cross each other as it was in the previous case. Thus the observations made for Fig. 22 are not universal in any aspect. To draw any conclusions a more systematic analysis is needed, where each parameter will be separated.

Figures 22 and 23 confirm the hypothesis made in previous section. Despite the fact that main driver of atomization in flash-boiling conditions is the flash boiling itself, the fluid temperature

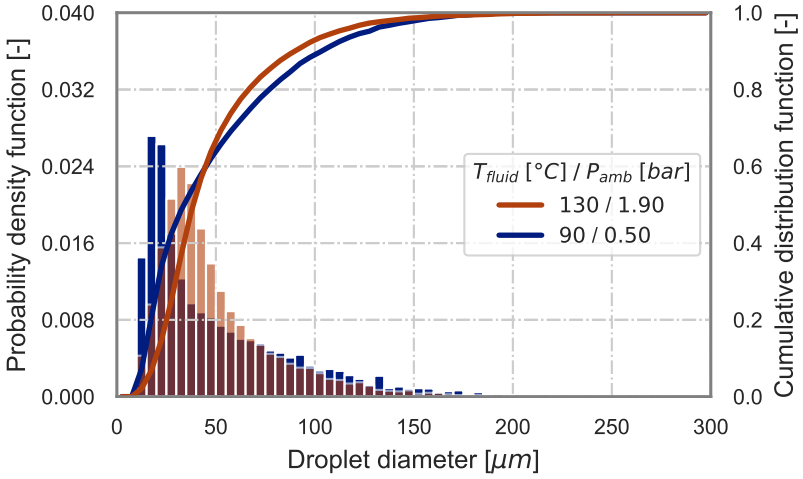

FIGURE 22: Volume based probability density functions and cumulative distribution functions for approximately constant $Rp = 1.4$

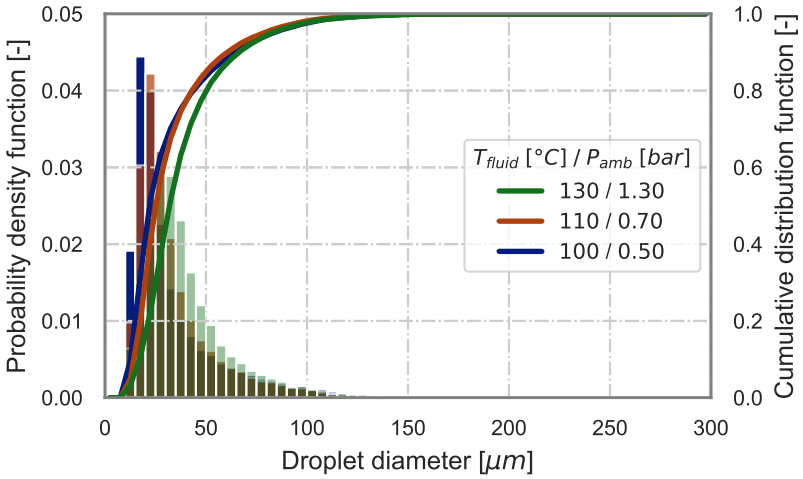

FIGURE 23: Volume based probability density functions and cumulative distribution functions for approximately constant $Rp = 2.05$

and ambient pressure are not negligible in droplet atomization and the final size distribution formation. This is in line what was observed previously for high injection pressure conditions [43, 78, 85]. To find more consistent pattern for the droplet size distribution changes, the results of the tests were divided into the subgroups with respect to liquid temperature and analysed separately.

In Fig. 24, droplet size distributions at $T_{fluid} = 70\,°C$ were shown in the form of probability density distribution and cumulative distribution function. A superheat degree ΔT and superheat ratio Rp were changed from 4, 11, 20 °C and 1.04, 1.55, 2.59 respectively. The plot, distinctly shows how the flash-boiling affects droplet sizes distribution. Looking at the probability density functions, a systematic and consistent mode shift towards the lower droplet sizes and reducing the tail of distribution can be observed as ΔT and Rp increases. This trend of droplets' size

reduction is better visible at the cumulative distribution graph, where together with ΔT and Rp increases. A remarkable fact is that the shift can be seen in all range of diameters, it means that smaller and bigger droplets are reduced at the same time. The $CDFs$ do not cross each other, as it was observed in Figs. 17 and 20 for subcooled conditions. Also, it can be observed that together with Rp increase, the CDF plots not only are shifted, but also a slope of the increase is much faster. This means that the distance between $Dv10$ and $Dv90$ is reduced. Lastly, the distance between the $CDFs$ is decreasing together with overheat. This is also proved later on higher number of cases.

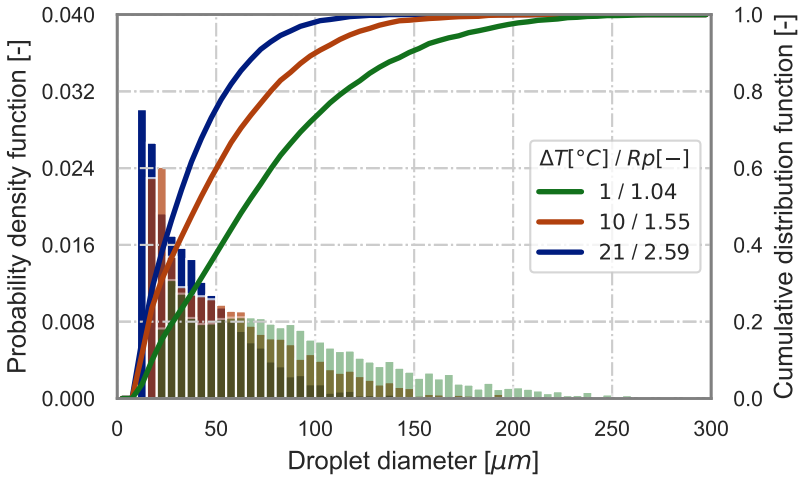

FIGURE 24: Volume based probability density functions and cumulative distribution functions for $T_{fluid} = 70\,°C$ at different superheat ratio

To quantify the above observations, the droplet sizes metrics were shown in Fig. 25. It can be seen that $Dv90$ is reduced from 149.8 to 103.2 and 73.4 µm what gives a significant 31% and 51% reduction respectively. Similarly, for $Dv50$ the sizes are 67.8, 32.7 and 43.5 µm, what gives

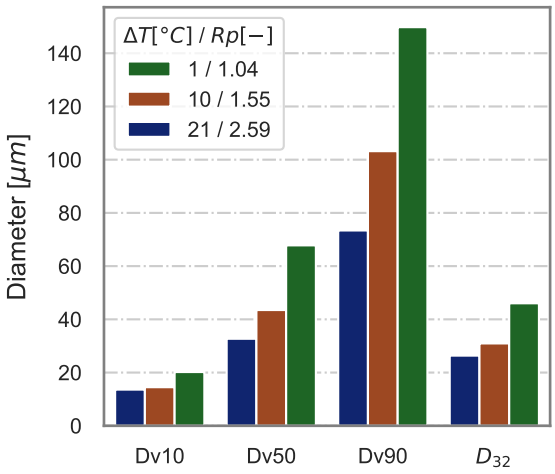

FIGURE 25: Droplet size's metrics for water at $T_{fluid} = 70\,°C$ at different superheat ratio

36% and 51% reduction respectively. It also can be noted that the lowest $Dv90$ ($\Delta T = 20\,°C$, $Rp = 2.36$) is comparable with the highest $Dv50$ ($\Delta T = -1\,°C$, $Rp = 0.95$), what greatly shows the potential of flash boiling usage to droplet diameter reduction. $Dv10$ is reduced from 20.2, 14.5 to 13.6 µm. Lastly, summarizing the analysis of cumulative statistics, the same trend can be observed for D_{32}, which also takes into account a number based distribution The sizes are reduced from 46.4 to 34.1 and 26.5 µm, which is 28% and 43% respectively. The observed differences are distinctly higher for those observed for subcooled conditions.

To confirm the findings made on the data series at $T_{fluid} = 70\,°C$, the same sets of plots were shown in Figs. 26 – 32 for the rest of the temperature series ($80 - 140\,°C$). All graphs are confirming previously made statements. Firstly, all $PDFs$ show the same consistent trend that together with the superheat ratio increase the mode is shifted to the left, while the tail is shortened. Also for CDF characteristics, the same trend of droplet sizes decrease can be seen for the whole distribution. However, the distance between $CDFs$ for different cases decreases together with Rp.

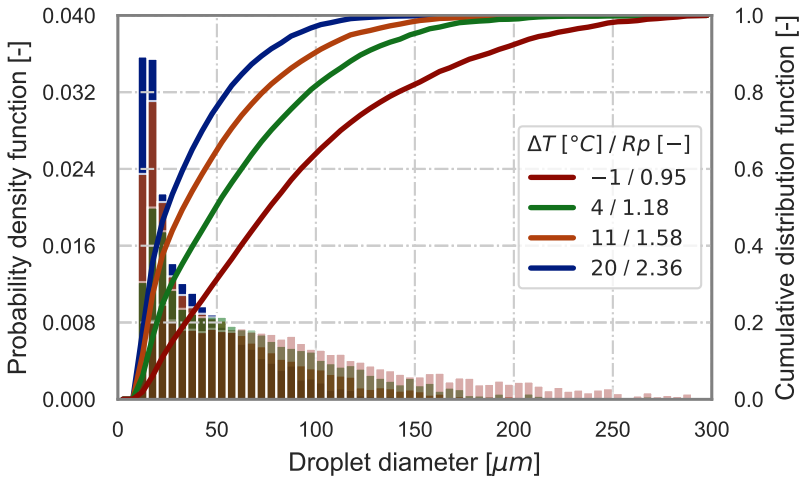

FIGURE 26: Volume based probability density functions and cumulative distribution functions for $T_{fluid} = 80\,°C$ at different superheat ratio

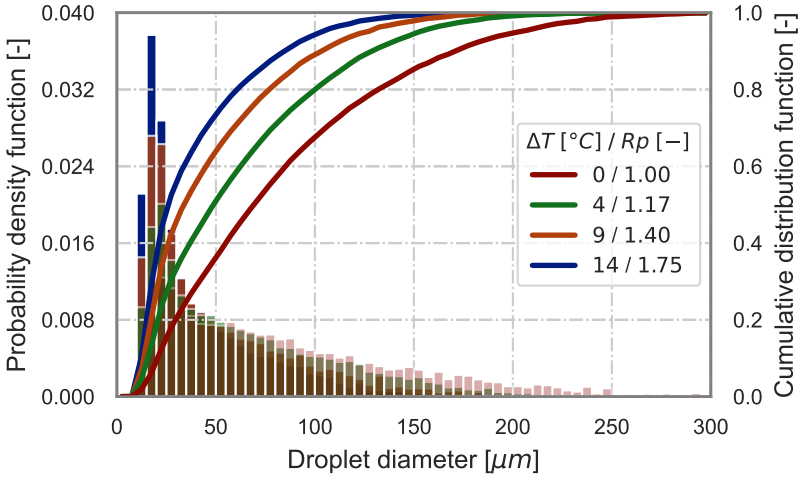

FIGURE 27: Volume based probability density functions and cumulative distribution functions for $T_{fluid} = 90\,°\text{C}$ at different superheat ratio

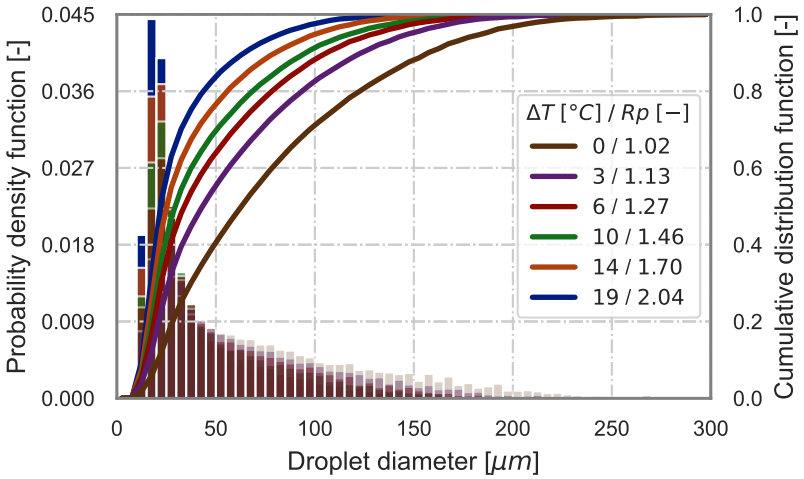

FIGURE 28: Volume based probability density functions and cumulative distribution functions for $T_{fluid} = 100\,°\text{C}$ at different superheat ratio

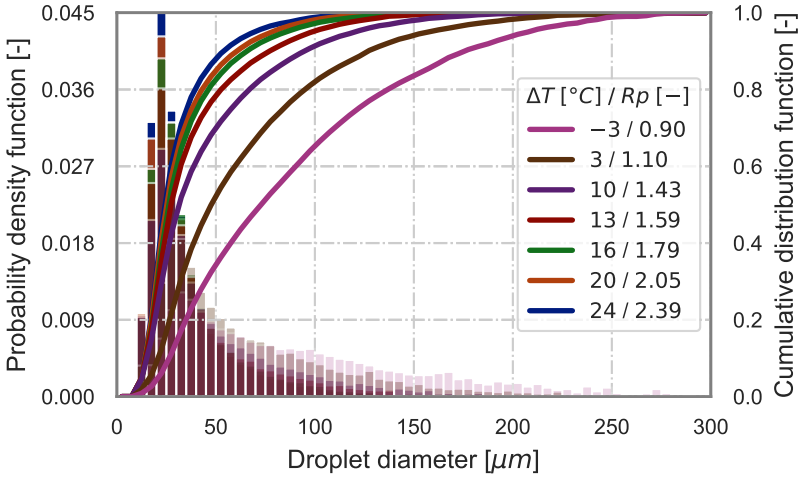

FIGURE 29: Volume based probability density functions and cumulative distribution functions for $T_{fluid} = 110\,°C$ at different superheat ratio

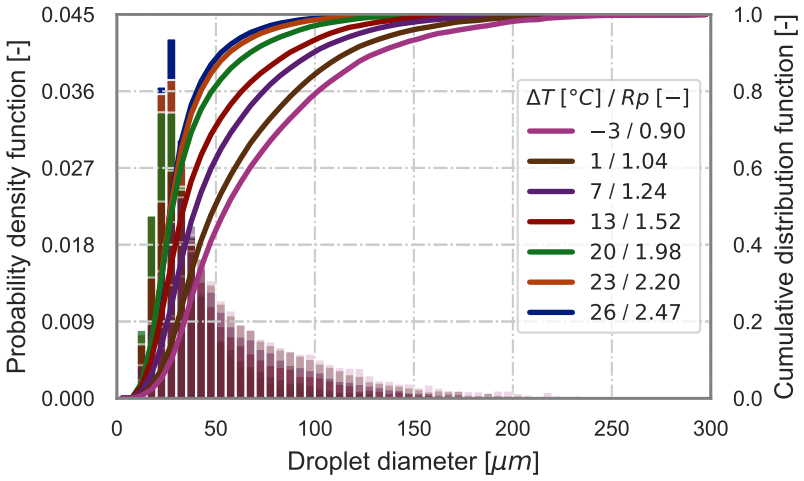

FIGURE 30: Volume based probability density functions and cumulative distribution functions for $T_{fluid} = 120\,°C$ at different superheat ratio

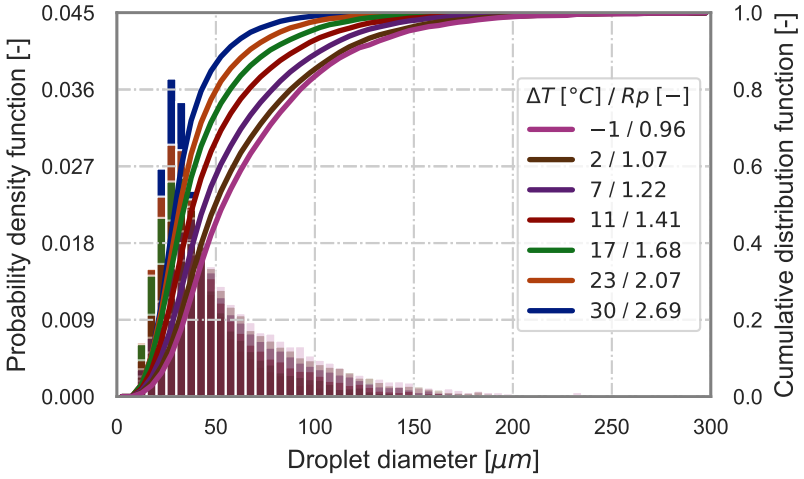

FIGURE 31: Volume based probability density functions and cumulative distribution functions for $T_{fluid} = 130\,°C$ at different superheat ratio

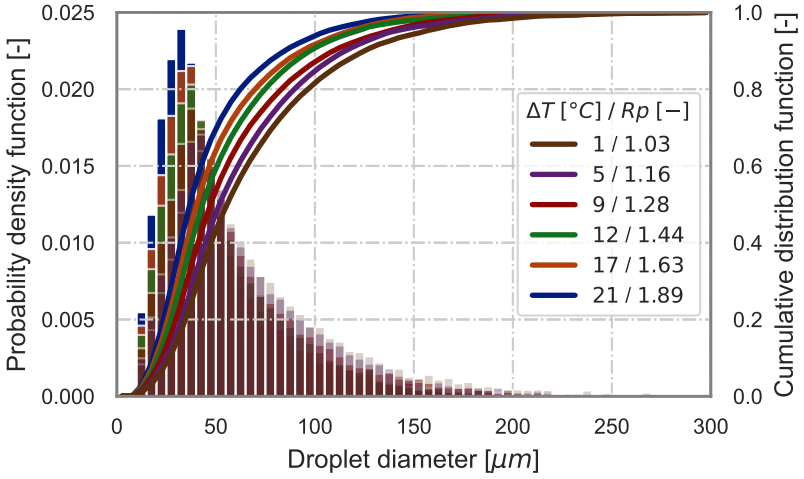

FIGURE 32: Volume based probability density functions and cumulative distribution functions for $T_{fluid} = 140\,°C$ at different superheat ratio

In order to compare all characteristics from Fig. 24 and Figs. 26 – 32 all metrics: $Dv10$, $Dv50$, $Dv90$, and D_{32} were shown versus Rp in Fig. 33. Focusing on the global qualitative trend it can be noted that the points form non-linear shapes on the graphs. This especially can be seen for $Dv90$, where the scattered points form some kind of quadratic or hyperbolic functions. Such a trend was also observed for D_{32} in the previous studies [75, 85], this actually greatly depicts the trend of decreasing the effect of the droplet size reduction in function of the overheat, which was discussed above. Also, a clear distinction based on the fluid temperature can be done each T_{fluid} creates its own reduction path. The way of reduction remains similar, however, Rp itself does not fully explain the phenomenon, and this is visible on each plot.

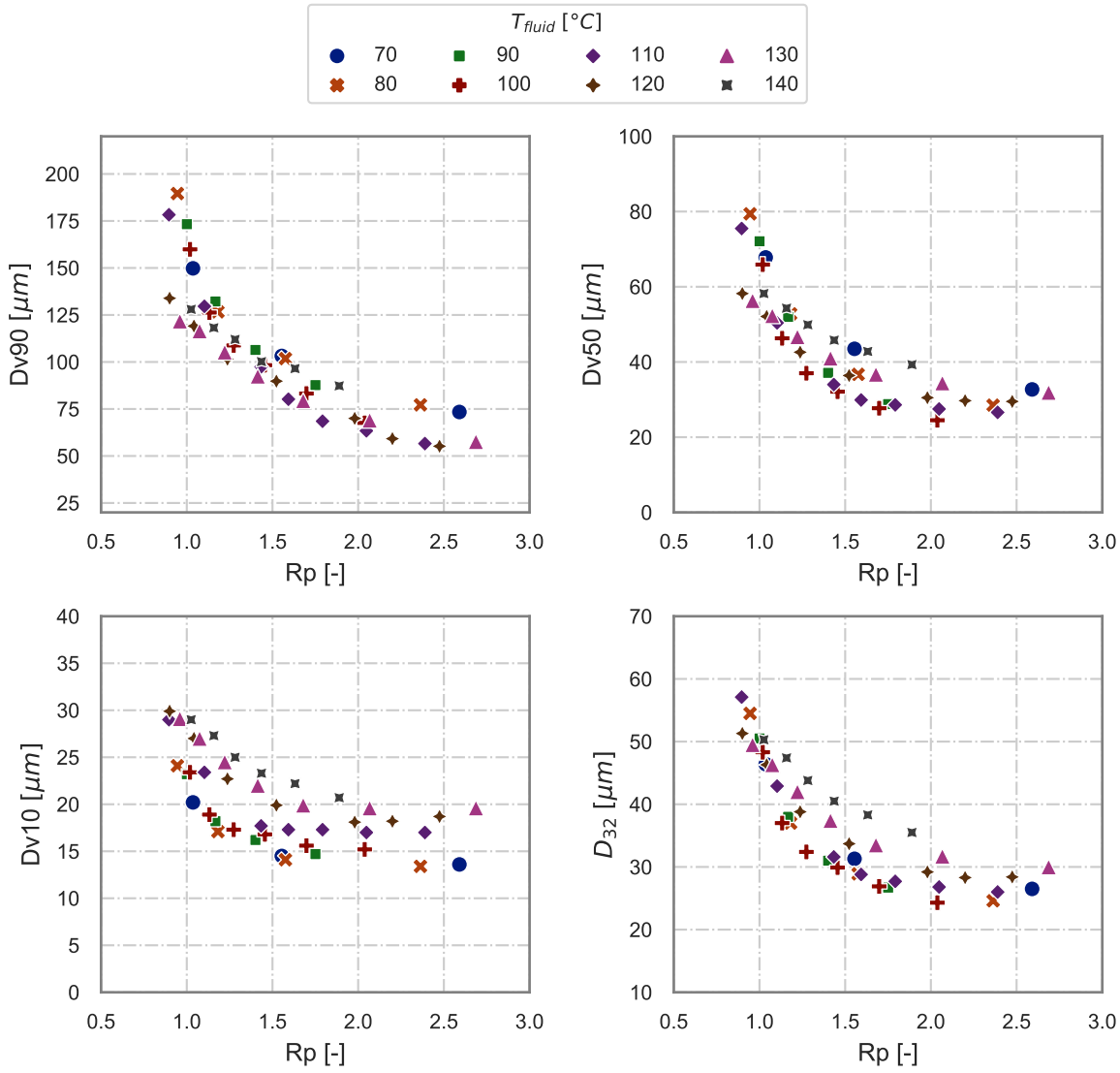

FIGURE 33: $Dv90$, $Dv50$, $Dv10$ and D_{32} versus Rp for water at different fluid temperature

Based on each metric a significant impact of flash boiling on the droplet size can be seen. $Dv90$ is reduced from ranges of $120-200$ µm up to $50-80$ µm. The highest observed $Dv90$ reduction is approximately 68.3% for $T_{fluid} = 110$ °C, and the lowest is 51% for 70 °C. In the

case of $Dv50$, it was reduced from ranges of $60-80$ µm up to $20-40$ µm with the highest reduction 64.8% for $T_{fluid} = 110\,°C$, and the lowest 43.3% for $T_{fluid} = 130\,°C$. For $Dv10$ the upper range is $20-30$ µm, and the lower is $12-20$ µm, the highest observed reduction is 44.4% for $T_{fluid} = 80\,°C$ and the lowest 32.6% for $T_{fluid} = 130\,°C$. Lastly, D_{32} is reduced from range $45-60$ µm to $20-30$ µm, while the highest reduction 54.9% for $T_{fluid} = 80\,°C$, and lowest 39.4% for $T_{fluid} = 130\,°C$.

In this section it was shown that the superheat ratio parameter (Rp) do not fully describe the investigated phenomenon, as it does not take all possible physical variables during the flash-boiling atomization. Nevertheless, the study also shown that for cases grouped by liquid temperature, the changes in the droplet sizes distributions follow a systematic pattern and they are similar for each analysed group. This gives a direction for a modelling approach of droplet size distribution, which is conducted in the next section.

3.3 Droplet size distribution model for size predictions

In this section, an approach for droplet size reduction modelling is discussed. The primary goal was to create a model that describes a global trend in droplets' probability density function change due to flash-boiling effects along with increasing superheat ratio. The assumption for model creation is based on the finding from the previous section, and it states that the model should catch the trends observed for each individual T_{fluid} series. At the same time, it should also take into account that ambient pressure and fluid temperature can affect droplet distribution. This is organized as follows; firstly, the best continuous probability density function is searched in terms of experimental data representation. Secondly, the best fit variables are discussed in terms of their trends in the function of superheat ratio and a simplified model to capture their global trends is suggested. Finally, the model performance is assessed based on the ability to model the best fit function and experimental data.

To find the best probability density function, the number of different most common functions were tested against the experimental data. Table 3 shows a full list of investigated distributions. It contains the full distribution names, which for the practical reasons and visualization purposes were simplified to the shortened versions. Also a number of equations' parameters is given (including scaling; hence the minimum is one parameter). The right-skewed distributions were selected since all experimental data show such a feature. The total number of evaluated functions was 19.

The Kolmogorov-Smirnov distances ($K-S = sup|Y-Y'|$) between the experimental distributions of the samples and cumulative distributions of functions were calculated to evaluate the quality of the fits [105]. Overall, the smaller the $K-S$ statistic is, the better the fit of a function. All, listed in the Tab. 3, distributions were fitted at each operating condition. Figure 34

TABLE 3: List of investigated probability density functions for the best fit [100]

Full name	Simplified name	Number of parameters
Beta	beta	3
Generalized extreme value (Gumpel)	genextreme	2
Log-normal	lognorm	2
Generalized gamma	gengamma	2
Generalized normal	gennorm	3
Weibull	weibull_min	2
Beta prime	betaprime	3
Burr	burr	3
Log-logistic (Fisk)	fisk	2
Inverse Gaussian	invgauss	2
Inverted gamma	invgamma	3
Log-Laplace	loglaplace	2
Logarithm gamma	loggamma	2
Maxwell	maxwell	1
Rice	rice	3
Inverted Weibull	invweibull	2
Exponential power (generalized Gaussian)	exponpow	2
Exponentiated Weibull	exponweib	3

shows the representative example of fitted functions for water at $T_{fluid} = 80\,°C$, $Rp = 0.94$. The presented functions: Weibull, inverse Gaussian and logarithm gamma, were fitted with $K - S$ distance equal to 0.041, 0.083 and 0.147 respectively, which are the best, medium and the lowest-ranked fits from all considered functions (in this particular case). At the plot, it can be seen that, indeed Weibull function is the best fitted to the experimental data, which is visible from both *PDF* and *CDF* points of view. Inverse Gaussian is too skewed to the left,

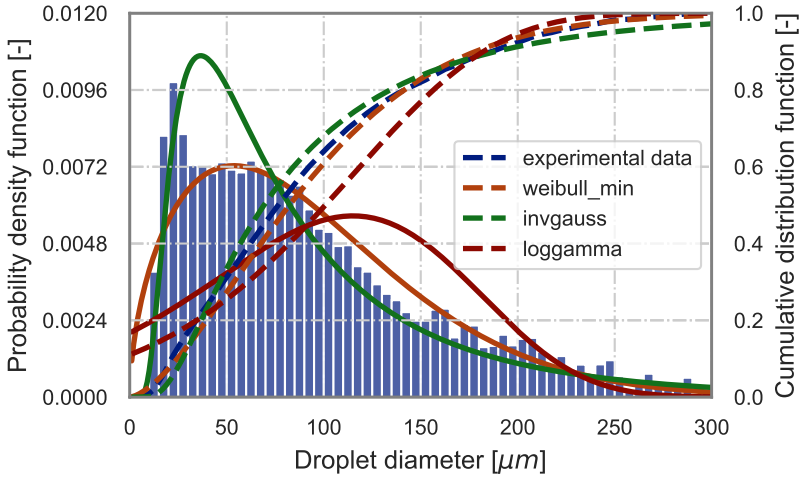

FIGURE 34: Different probability density functions (Weibull, inverse Gaussian and logarithm gamma) and the experimental data; water injection at $T_{fluid} = 80\,°C$, $Rp = 0.94$ (solid line – *PDF*, dashed line – *CDF*)

overestimating the probability of smaller droplets. At the same time, it overestimates the sizes of bigger droplets since the *CDFs* cross each other. On the other hand, logarithmic gamma completely misses at the smallest sizes, while medium sizes are overestimated, and bigger sizes are underestimated again.

Since the droplet size distributions are characterized in various conditions, ranging from a transitional state ($Rp \sim 1$) to a fully flashing state ($Rp \sim 2.5$), the shape of the distributions is distinctly changed, which was shown in Figs. 24 – 32. Therefore, the best function for one operating point can have a much worse fit in other conditions. Figure 35 shows the same probability density functions that were used in the previous example (Fig. 34) but for different operating conditions – $T_{fluid} = 80\,°C$ and Rp = 1.57. Hence, now the functions are fitted to fully-flashing conditions. The calculated $K-S$ distances are 0.121, 0.116, 0.203 for Weibull, inverse Gaussian and logarithm gamma distribution, respectively, so first of all, the best fit now is given by inverse Gaussian. Secondly, the overall $K-S$ distances are higher than for those shown in Fig. 34. It can be seen that for these conditions, the experimental *PDF* is highly skewed. Thus, inverse Gaussian is the most appropriate while Weibull distribution is too "flat". Based on these observations, the best fit should be the function that gives the best performance across all considered operating points.

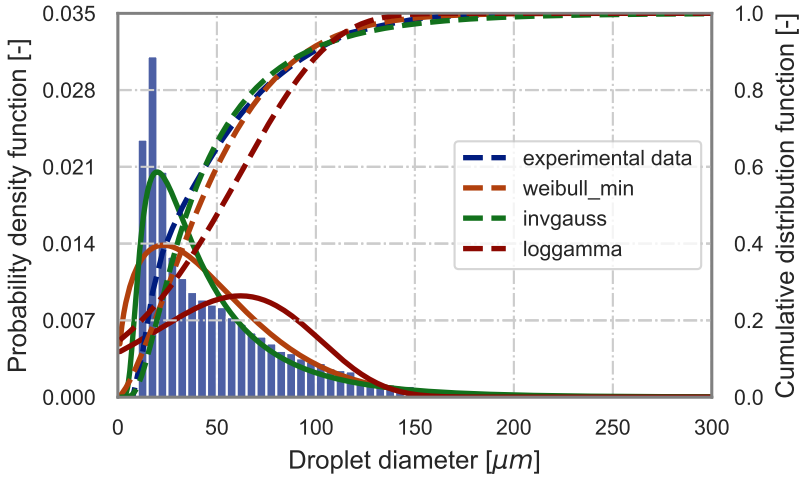

FIGURE 35: Different probability density functions (Weibull, inverse Gaussian and logarithm gamma) and the experimental data; water injection at $T_{fluid} = 80\,°C$, $Rp = 1.57$ (solid line – *PDF*, dashed line – *CDF*)

To shorten the list of distributions, all calculated $K-S$ distances for flashing operating conditions were aggregated and shown on a box plot in Fig. 36. To perform the initial selection, the first step was to decline all functions with outliers, (genextreme, loglaplace, invweibull and exponpow). Secondly, as there are many functions within similar range of boxes, it was decided to cut off all function with median above the $K-S = 0.1$. Hence lognormal, gengamma,

betaprime, burr, invgauss and exponweib were chosen for the final examination (theoretically, also fisk should be included, however, this is a special case of burr function [100]).

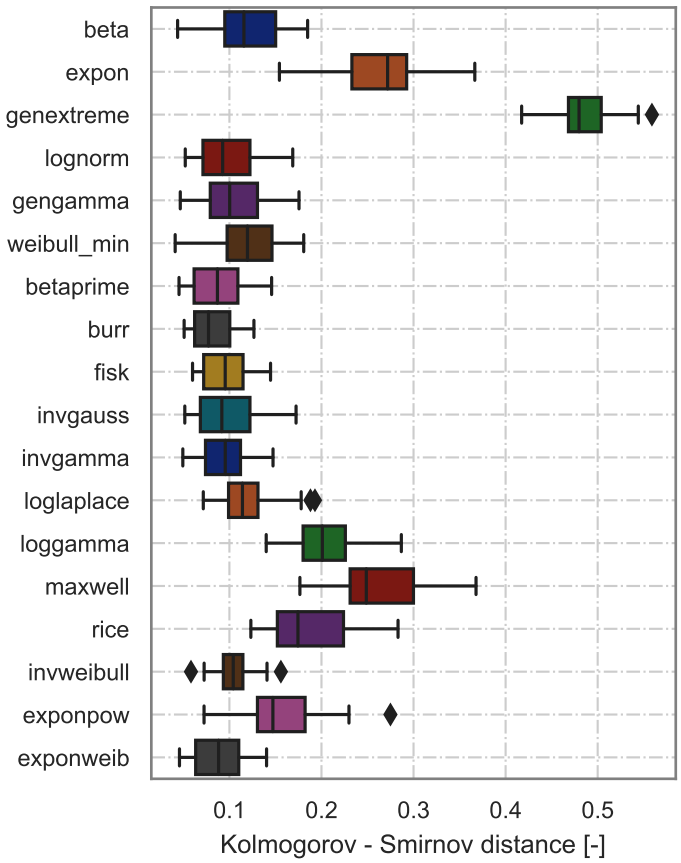

FIGURE 36: $K-S$ distance box plots for tested probability density functions

The final six nominated functions are given by the following equations:

- Log-normal distribution (lognorm):

$$f(x;\sigma,\mu) = \frac{1}{x\sigma\sqrt{2\pi}} exp\left(-\frac{(ln(x)-\mu)^2}{2\sigma^2}\right) \tag{15}$$

  where $\mu$is the mean of natural logarithms of the probe and σ is its standard deviation of $ln(x)$.

- Generalized gamma (gengamma):

$$f(x;\beta\ ,\alpha) = \frac{\beta^{\alpha}}{\Gamma(\alpha)} x^{-\alpha-1}\ exp\left(-\frac{\beta}{x}\right) \tag{16}$$

  where α is a shape parameter, β is a scale parameter, $\Gamma(n) = (n-1)!$ is a gamma function.

- Beta prime (betaprime):

$$f(x;\alpha,\beta) = \frac{x^{\alpha-1}(1+x)^{-\alpha-\beta}}{B(\alpha,\beta)} \tag{17}$$

where α and β are shape parameters, and B is a beta function:

$$B(\alpha,\beta) = \int_0^1 t^{\alpha-1}\ (1-t)^{\beta-1}\ dt \tag{18}$$

- Burr (burr):

$$f(x;\ \alpha\ ,\beta\ ) = \alpha\beta\frac{x^{\alpha-1}}{(1+x^{\alpha})^{\beta+1}} \tag{19}$$

where c and k are shape parameters.

- Inverse Gaussian (invgauss):

$$f(x,\mu,\alpha) = \sqrt{\frac{\lambda}{2\pi x^3}} exp\left(-\frac{\lambda(x-\mu)^2}{2\mu^2 x}\right) \tag{20}$$

where λ is a shape parameter and μ is a mean of a probe.

- Exponentiated Weibull (exponweib):

$$f(x;k,\lambda,\alpha) = \alpha\frac{k}{\lambda}\left(\frac{x}{\lambda}\right)^{k-1}\left(1-exp\left(-\left(\frac{x}{\lambda}\right)^{k}\right)\right)^{\alpha-1}\exp\left(-\frac{x}{\lambda}\right)^{k} \tag{21}$$

Figures 37 and 38 show the distribution functions given by eq. 15 – eq. 21 plotted with the experimental data for boundary conditions ($Rp = 0.94$) and fully-flashing conditions ($Rp = 1.57$). Since the $K-S$ distance was optimized and its interpretation is a distance between cumulative distribution functions, it can be seen that there all functions are close to the experimental data. Nevertheless, substantial differences can be observed. For the low Rp operating point (Fig. 37), the highest skewness and mode are shown by log-normal and inverse gaussian functions, while for the rest, these parameters are lower and at a similar level. This, however, is changed for fully-flashing conditions (Fig. 38) where Burr distribution has the higher mode, while inverse gaussian and log-normal are at lower levels. It may indicate that some functions can be better for small and others for high superheat ratios.

In order to check the mentioned hypothesis, a $K-S$ distance versus Rp was plotted in Fig. 39. It can be observed that points are formed in structures related to the boxplots from Fig. 36. Hence the exponentiated Weibull is placed at the bottom of the group, while gengamma can be distinguished in the upper region. Nevertheless, there is no strict correlation between the

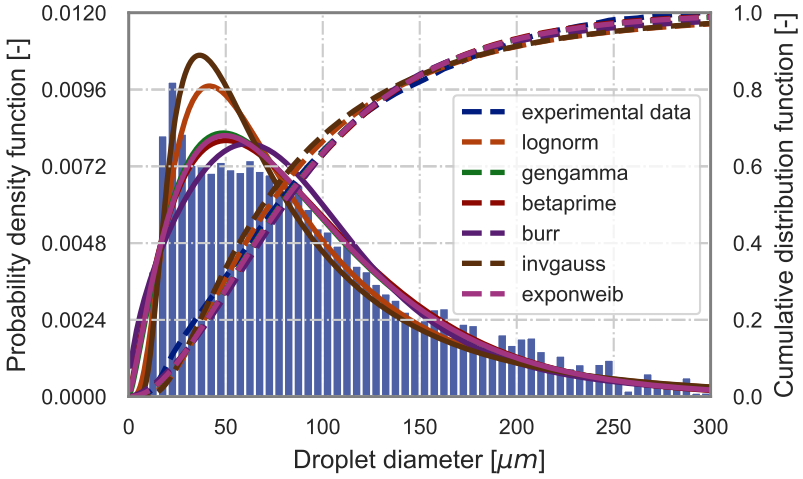

FIGURE 37: Initially selected probability density functions shown for water at $T_{fluid} = 80\,°C$, $Rp = 0.94$ (solid line – PDF, dashed line – CDF)

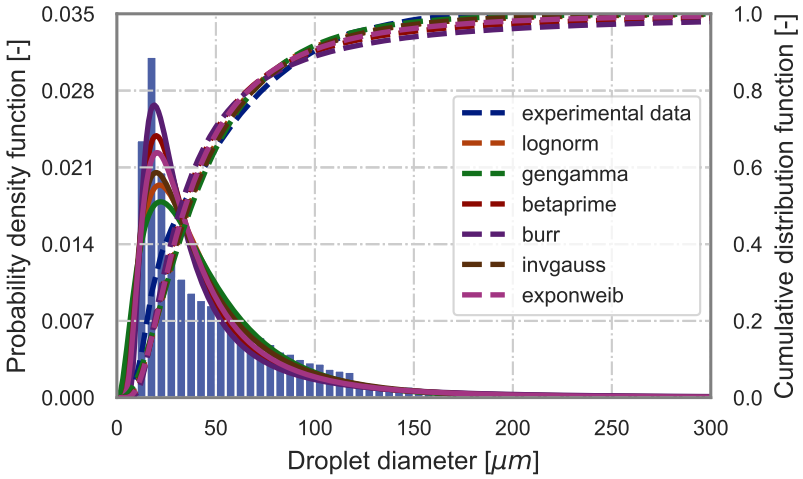

FIGURE 38: Initially selected probability density functions shown for water at $T_{fluid} = 80\,°C$, $Rp = 1.57$ (solid line – PDF, dashed line – CDF)

function type and the superheat ratio, and it can be generally concluded that better fits are given for low overheats. Also, it cannot be said that one function performs better in some conditions.

Finally, to quantitatively compare all functions, quantile-quantile plots were created and shown in Fig. 40. To create the plots, for each distribution at each operating condition, a set of quantiles was calculated (y-axis) and paired with the corresponding quantiles from the experimental data (x-axis). The range of quantiles was narrowed to $10^{th} - 90^{th}$ as this is in the range of discussed earlier metrics ($Dv10 - Dv90$) and will be a primary focus of the created model. Two types of general trends can be observed, the first one for log-normal and inverse gaussian distribution, where for the smallest and biggest droplet the quantiles overlap ($f(x) = x$), while in the middle range (above 50 µm) they are underestimated. The second type is observed for the rest of the distributions. For smaller droplets the quantiles overlap as well, but for larger

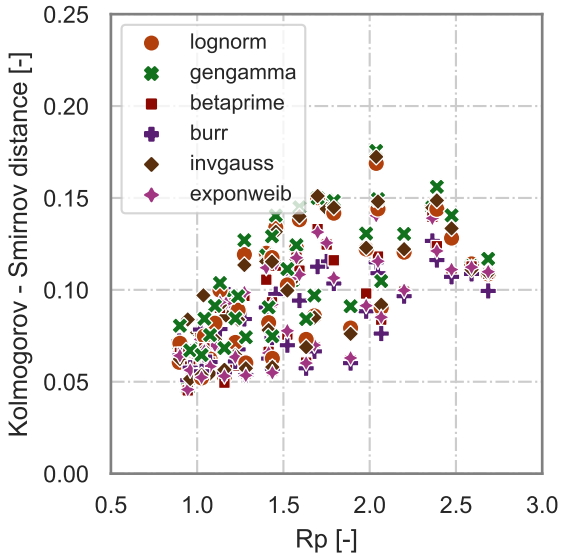

FIGURE 39: $K-S$ distance versus Rp for flash-boiling conditions

droplets they are underestimated. The calculated coefficient of determination is at a high level for all cases, the highest for exponentiated Weibull and beta prime functions (0.984), and the lowest for inverse gaussian (0.981). Thus, all functions provide a good quality of modelling data between the 10^{th} and 90^{th} quantiles.

Summarizing the above discussion, a log-normal distribution was chosen as an input function for data modelling. The reason for that was the log-normal function has the most intuitive form with parameters mean μ and standard deviation σ directly coming from the obtained data. Also, it does not include any inner functions (like Γ or B in eq. 16 – eq. 17). It depends on two parameters instead of three like for exponentiated Weibull, while the simplicity of log-normal functions does not result in significant quality deterioration.

Fig. 41 shows the log-normal function sensitivity to the controlling parameters μ and σ to present the intuition behind the model. The values of both parameters were chosen to represent the minimal, maximal, and arithmetic mean of fitted to the experimental data log-normal functions. It can be seen that increase of μ at fixed σ results in flattening the distribution and dragging it toward the right side, and what is important, it is happening in the whole range of droplet sizes. On the contrary, if one looks at the plot of different σ for fixed μ it can be seen that σ change results in the slope of CDF change, while all $CDFs$ are crossing each other at the same point. Also, the trend is slightly different than observed for μ. Along with σ increase, the mode is dragged toward the left, and the shape is flattened. Thus, it results in a reduction of droplet sizes at higher percentiles (above the crossing), and a slightly increase of smaller droplets percentiles. Thus, $Dv10$ increases with smaller σ, while $Dv90$ decreases at the same time. As it is shown in the plots, such a model is much more sensitive to μ changes than for σ.

Figure 42 shows σ and μ in the function of superheat ratio Rp. Firstly, analysing σ, it can be

noticed that a major trend is decreasing along the *Rp* increase. Thus, based on the previously shown intuition behind the log normal *PDF* (Fig. 41), it will result in a higher mode shifted

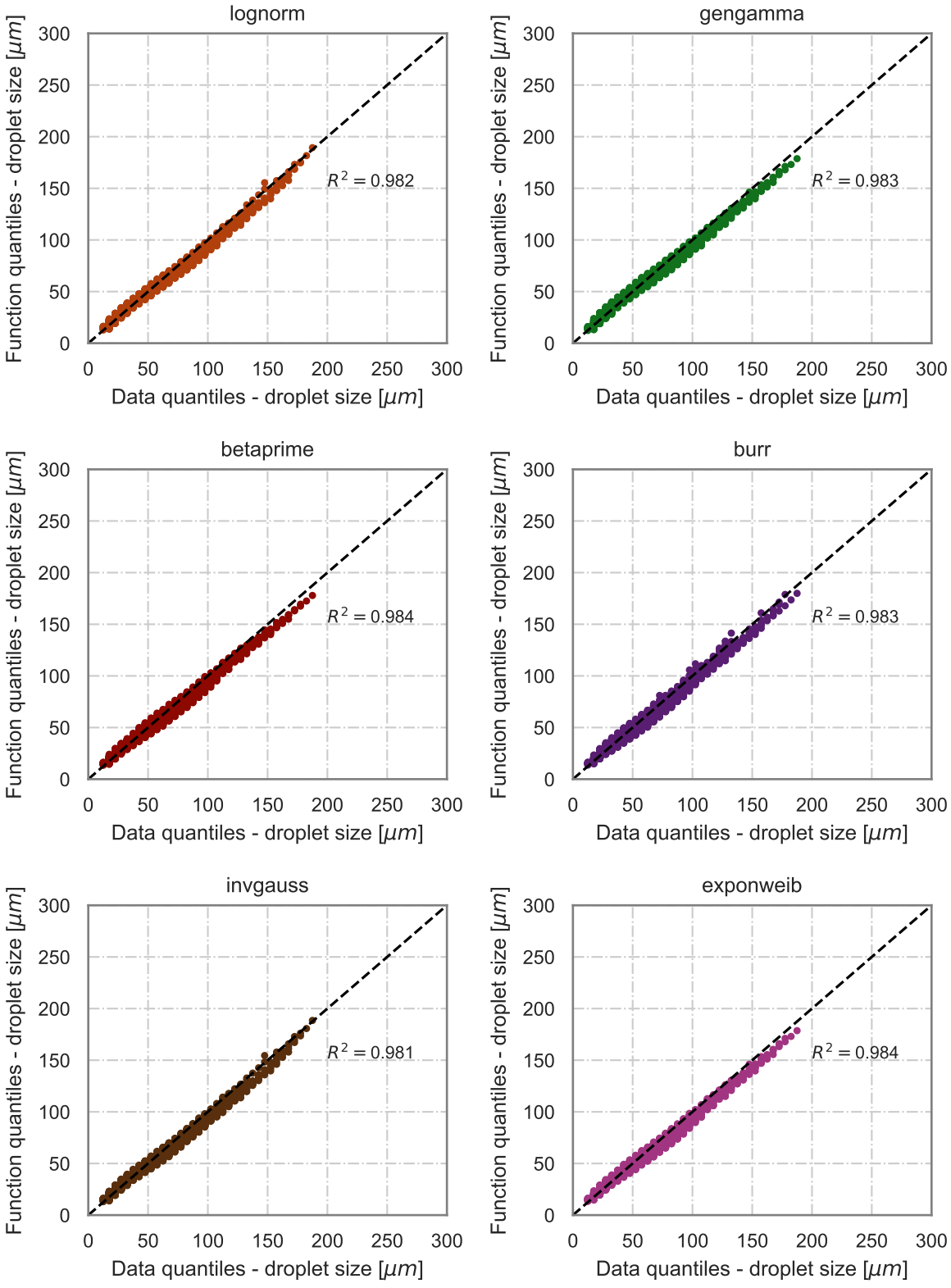

FIGURE 40: Quantile-quantile plots for log-normal, generalized gamma, beta prime, burr, inverse gaussian and exponentiated Weibull distributions

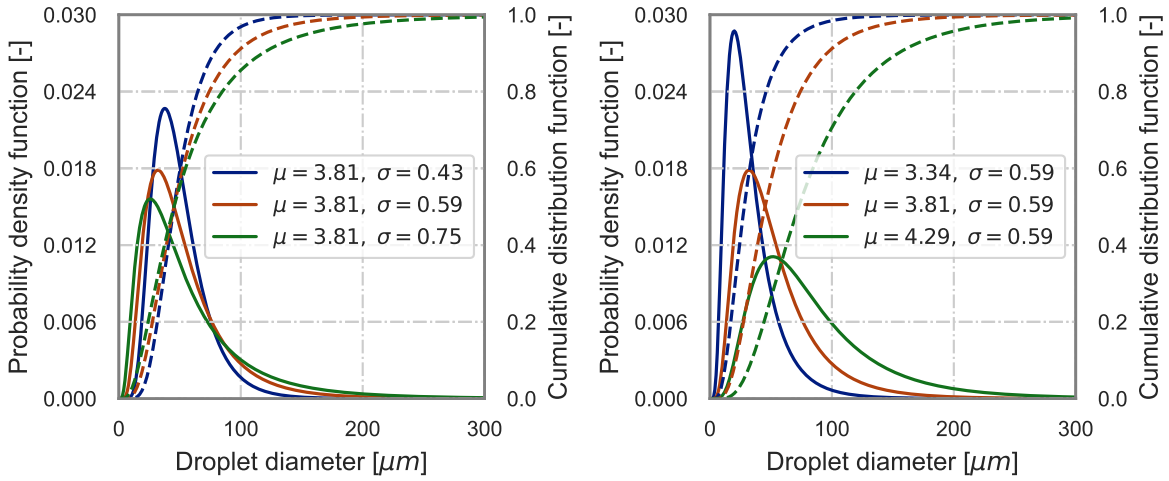

FIGURE 41: Log-normal distribution function sensitivity for different σ with fixed μ (left plot) and different μ with fixed σ (right plot)

to the right-hand side. Going into the details, the points are visibly separated by the fluid temperature so that each individual temperature makes its own trend. However, the trend direction remains similar, which is discussed in detail later on. Regarding the μ plot in the function of Rp, also a decreasing global trend can be observed, actually very similar to those observed for $Dv10$, $Dv50$, $Dv90$ and D_{32} (Fig. 33) with non-linear trend resampling hyperbolic kind of shape. Looking at the CDF functions, both parameters' decrease will result in a reduction in sizes of the biggest droplets, while for smaller droplets, reduction by μ will be suppressed by σ effect. Characteristics of μ can also be divided into groups distinguished by fluid temperature.

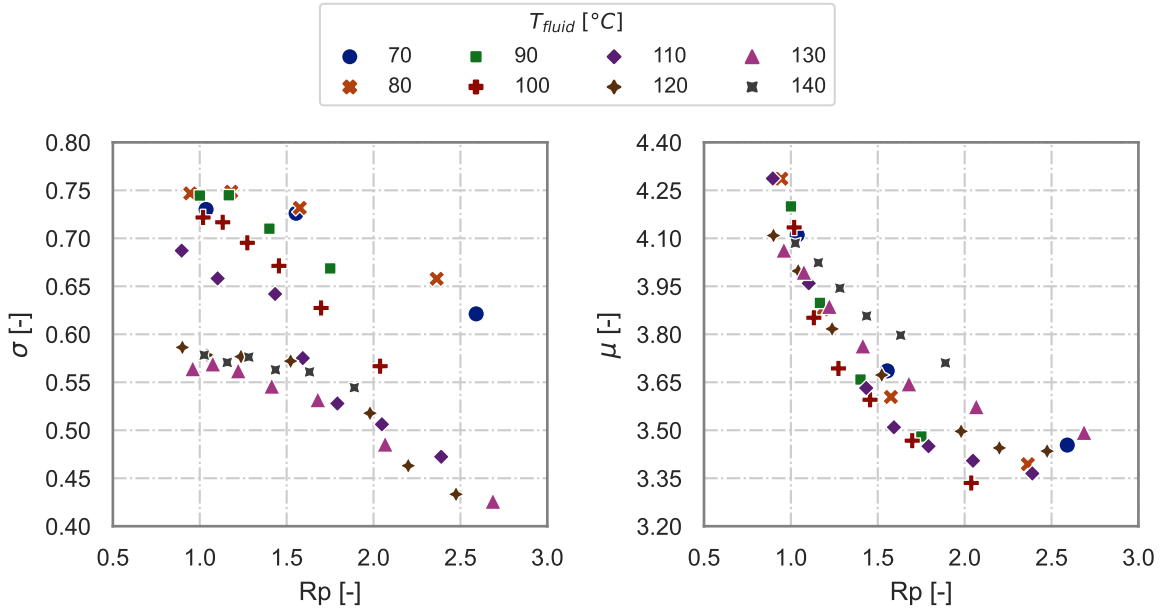

FIGURE 42: Standard deviation σ and mean μ for all cases included in group 3 (Fig. 7)

As mentioned earlier, both parameters show division regarding the fluid temperature (T_{fluid}). While for σ the linear approximation in the function of Rp is clear, in the case of μ, a hyperbolic correlation shall be considered. For each T_{fluid} subgroup, a linear regression was fitted with the following eq. 22 and eq. 23 for σ and μ respectively:

$$\sigma(Rp) = a_\sigma\left(T_{fluid}\right)\ Rp + b_\sigma\left(T_{fluid}\right) \tag{22}$$

$$\mu(Rp) = \frac{a_\mu\left(T_{fluid}\right)}{Rp} + b_\mu\left(T_{fluid}\right) \tag{23}$$

The linear regressions were fitted into the data with the ordinary least squares (OLS) method. All calculated coefficients, together with the coefficient of determination, can be found in Tab. 4. The visual representations of the regressions are shown in Fig. 43. Analysing regression obtained for σ with the experimental data, as was expected, all lines have decreasing trends; however, substantial differences could be noticed. The regressions are not parallel to

TABLE 4: Coefficients of linear regression (eq. 22 and eq. 23)

$T_{fluid}\,[^\circ C]$	a_σ	b_σ	R^2_σ	a_μ	b_μ	R^2_μ
70	-0.07	0.82	0.912	1.14	2.99	0.989
80	-0.07	0.82	0.921	1.39	2.76	0.977
90	-0.11	0.86	0.954	1.68	2.49	0.987
100	-0.16	0.89	0.988	1.53	2.56	0.965
110	-0.15	0.83	0.950	1.37	2.71	0.979
120	-0.10	0.69	0.907	1.01	3.00	0.995
130	-0.08	0.66	0.969	0.89	3.14	0.993
140	-0.04	0.62	0.896	0.86	3.27	0.992

each other, the fastest rate of decrease (lowest a_σ) is for $T_{fluid} = 100\,^\circ$C, while the slowest rate (highest a_σ) is for $T_{fluid} = 140\,^\circ$C, and for this particular case, it can be visible that the regression line breaks out from the average trend. All regressions were fitted with the satisfactory agreement of $R^2 > 0.89$. The worst approximation was for $T_{fluid} = 140\,^\circ$C and the best for $T_{fluid} = 100\,^\circ$C ($R^2 = 0.988$). In the case of regression fitted to the μ parameter, the overall quality of fit is distinctly higher than for σ, the $R^2 > 0.97$. All regressions are increasing in the function of $1/Rp$. The fastest rate is obtained for $T_{fluid} = 90\,^\circ$C, and the slowest is for $T_{fluid} = 140\,^\circ$C. While it can be observed that for both parameters, σ and μ, the direction coefficients are related to the T_{fluid}. It hardly can be said about any monotonic trend in this matter. Looking at the a_σ, for example, firstly, it increases in range of T_{fluid} between $70-110\,^\circ$C and then drops for higher temperatures. Similar observations can be made for μ.

Since the direction coefficient of fitted regression does not show any correlations to known experiment parameters, it was decided to generalize the model to simulate a globally averaged

trend of droplet size distribution reduction in means of σ and μ while leaving the possibility of fine-tuning the model by adjusting the intercept of the model, what lets include also the effect of ambient conditions on droplet sizing as well as adjust the model to other injector's data.

To build such a model, the a_σ and a_μ were averaged over the T_{fluid} to $a_{\sigma g} = -0.098$ and $a_{\mu g} = 1.235$ to capture the averaged effect of droplet size reduction over the T_{fluid} data series. The following linear equations are proposed to calculate σ and μ:

$$\sigma(Rp) = -0.098 \cdot Rp + f_\sigma \tag{24}$$

$$\mu(Rp) = \frac{1.235}{Rp} + f_\mu \tag{25}$$

where f_σ and f_μ are intercepts.

Next, in order to calculate the droplets sizes' probability distributions, eq. 24 and eq. 25 are applied to the log-normal distribution:

$$P(d) = \frac{1}{\sqrt{2\pi}\, d\, \sigma(Rp)} exp\left(-\frac{(ln(d) - \mu(Rp))^2}{2 \cdot (\sigma(Rp))^2}\right) \tag{26}$$

where d is a droplet diameter. It needs to be reminded that $P(d)$ refers to a volume-based probability function.

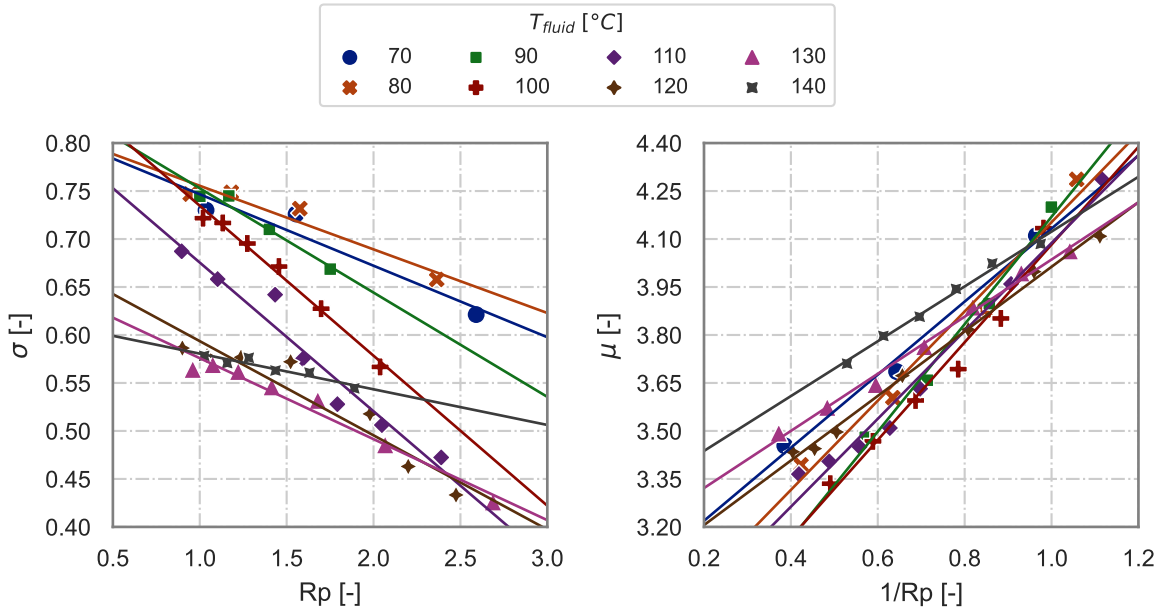

FIGURE 43: Standard deviation σ versus Rp, and mean μ versus $1/Rp$ for all cases included in group 3 (Fig. 7). Scattered points – experimental data; solid lines – regressions

Equations 24 and 25 were fitted with OLS to the experimental data. Table 5 contains f_σ and f_μ coefficients of the fitted model, and the visual representation can be seen in Fig. 44. As seen in the table, after the averaging, the overall coefficient of determination dropped. In the case of σ (eq. 24), the worst fit was obtained for $T_{fluid} = 140\,°C$ for which a coefficient of determination is below zero. This needs to be interpreted as in this case the fit is worse than the fitted horizontal line; nevertheless, the sensitivity study of log normal functions has shown that σ has a minor effect on PDF shape comparing to the μ parameter; thus, the most important feature is to simulate a systematic decrease of σ along the Rp. Also, the coefficient of determination of eq. 25 decreased compared to equation eq. 23 (Tab. 4). In this case, a decrease in coefficient of determination is not as high as for σ model. The worst fit was again for $T_{fluid} = 140\,°C$, but this time the $R^2 = 0.799$, which is a satisfactory value. All other cases are above 0.848, generally showing a good agreement.

TABLE 5: Coefficients f_σ and f_μ coefficient of determination for a averaged droplet sizing model

$T_{fluid}\,[°C]$	f_σ	R^2_σ	f_μ	R^2_μ
70	0.86	0.825	2.93	0.983
80	0.87	0.716	2.88	0.964
90	0.85	0.944	2.84	0.918
100	0.81	0.848	2.77	0.93
110	0.74	0.820	2.81	0.969
120	0.69	0.907	2.85	0.946
130	0.68	0.946	2.90	0.848
140	0.70	-1.473	2.99	0.799

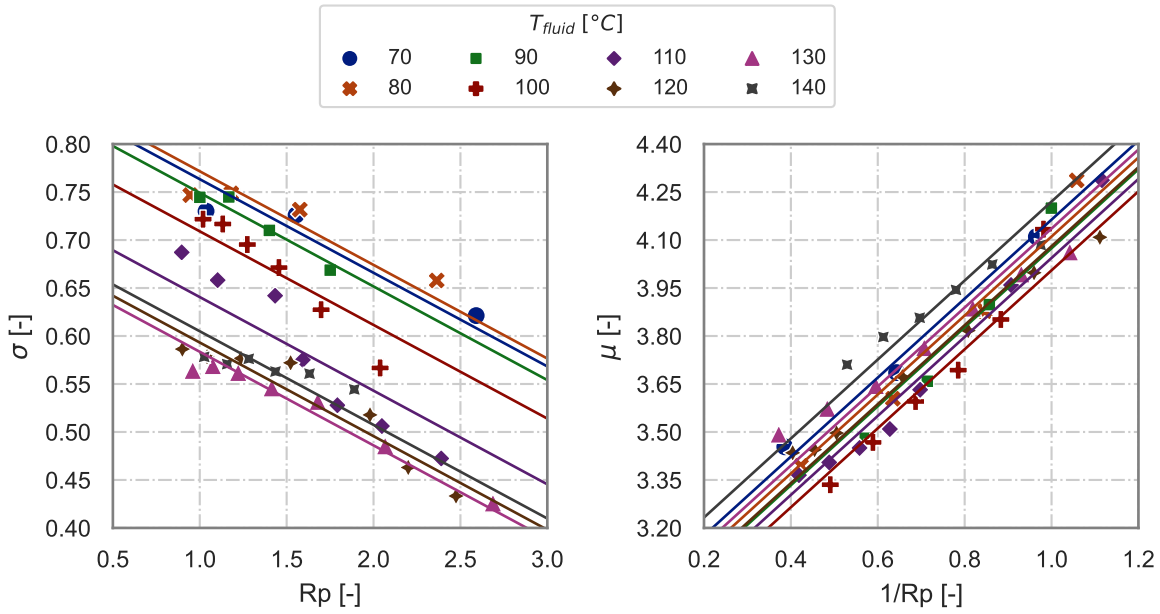

FIGURE 44: The averaged droplet sizing model fitted to the experimental data. Scattered points experimental data; solid lines adjusted model

To evaluate the model's accuracy, σ and μ were calculated using the equations (eq. 24 and eq. 25), and f_σ and f_μ from Tab. 5 and used to model the probability density function given by the model (eq. 26). Figure 45 shows the quantile-quantile plot of distributions calculated by the model for all cases and from the experimental data. The model performs with the overall coefficient of determination equal to $R^2 = 0.951$, which is lower compared to the directly fitted log-normal functions, where $R^2 = 0.982$ (Fig. 40). It can be seen that it predicts better for smaller diameters, while for larger droplets, some tend to fall into the underestimation.

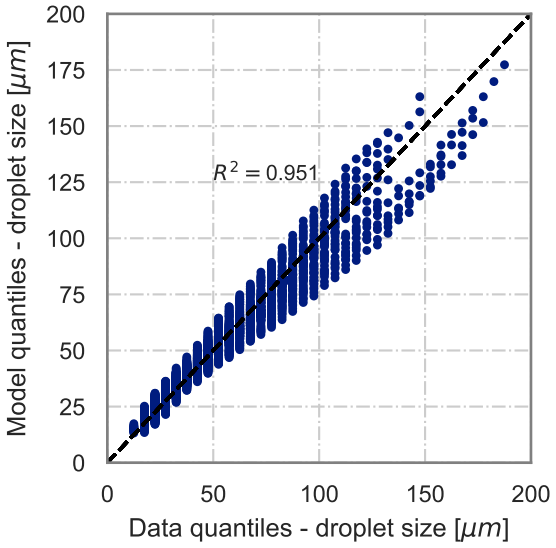

FIGURE 45: Quantile-quantile plot for the model for log-normal distribution and experimental data in the range of 10^{th} to 90^{th} quantile

While Fig. 45 depicts the overall model's performance, it does not tell anything about the order of quantile, giving only an overview of droplet sizes predictions. Therefore, the main metrics discussed in this work ($Dv10$, $Dv50$, $Dv90$, D_{32}) were plotted additionally in Fig. 46. The coefficient of determination is equal to 0.916, 0.851, 0.898 and 0.917 for $Dv10$, $Dv50$, $Dv90$ and D_{32} respectively. The best fits were obtained for D_{32} and $Dv10$, for which, both metrics oscillate close to $f(x) = x$ line. Next, in decreasing order, is $Dv90$ prediction quality. It can be seen that points are dispersed around the $f(x) = x$, but the main trend is kept in the whole range. The worst prediction performance is for $Dv50$. The overall level of agreement is satisfactory, especially for D_{32}, which captures the whole distribution characteristics and is one of the main metrics used to describe injectors in academia and industry.

Based on Tab. 5 , the worst performing model and best performing model were picked to graphically show their behaviours. The best performing model was for $T_{fluid} = 120\,°\text{C}$, and its behaviour over the range of Rp compared to the experimental data was shown in Fig. 47. The graph shows the log-normal function fitted to the experimental data (solid lines) and the calculated distributions using eq. 26 (dashed lines) for the range of Rp from 0.9 to 2.2. Analysing the PDF plot, it can be seen that the model captures the main trend very well all modelled

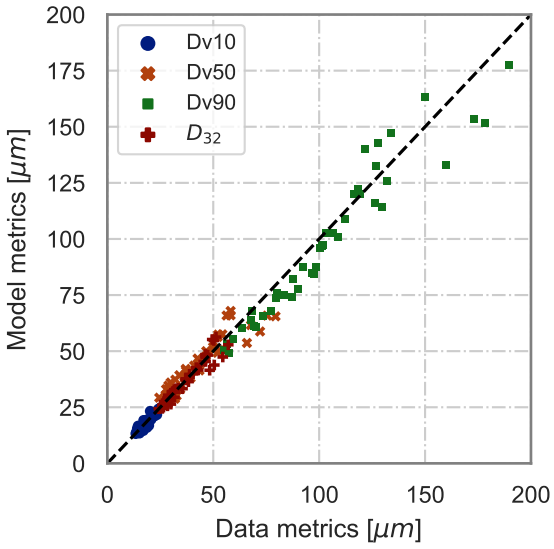

FIGURE 46: $Dv10$, $Dv50$, $Dv90$ and D_{32}; the model estimation (y-axis) and the experimental data (x-axis)

distributions consistently follow the experimental log-normal functions. The model is the best fitted for $Rp = 1.24$ where the $PDFs$ practically overlay. From this point, looking toward the lower Rp, the model tends to underestimate the mode, while for the higher Rp this trend is the opposite and the mode is slightly overestimated. Those observations can be easier interpreted based on the CDF graph. It can be seen that for low Rp, the droplet sizes are overestimated in the whole range, and this change to size underestimation after passing $Rp = 1.24$. It should be noticed that the distributions for higher Rp are modelled in a very satisfactory way.

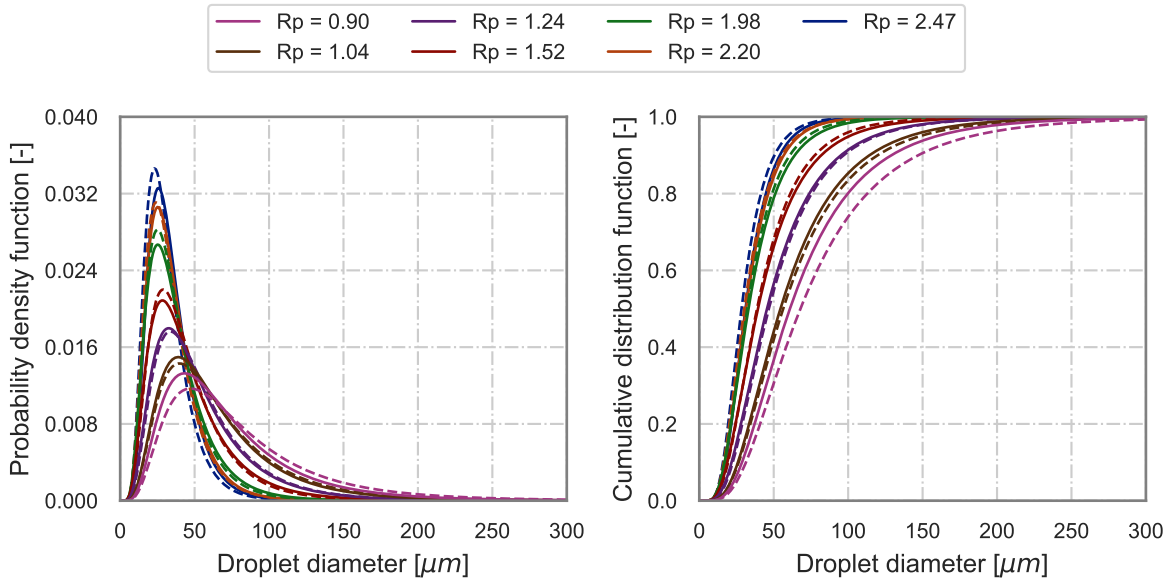

FIGURE 47: The best case scenario. The droplet size distribution calculated by the model (dashed line), and the log-normal distribution fitted to the experimental data (solid line) for $T_{fluid} = 120\,°C$

To quantify this observation, the main metrics were listed in Tab. 6. The highest deviation between log-normal and modelled distributions is for the lowest Rp (0.9). The difference for $Dv90$ is 18 µm (14%), while for $Dv50$ and $Dv10$ are 7 and 2.6 µm (11.6% and 9.2%), respectively. The overall difference for D_{32} is 5.2 µm, which is 10.1%. For the highest Rp (2.47), those differences are 1.9, 2.7, 3.6 and 2.6 ($Dv90$, $Dv50$, $Dv10$ and D_{32}), which is 6.7, 8.6, 10.4 and 9.2%. It can be noticed that while for the lowest Rp the best fit is given by small droplets and high ones are overestimated, for the highest Rp, this trend is the opposite, and the largest droplet sizes are predicted with the most satisfactory agreement. The overall droplet size in terms of D_{32} is in approximately the same order. The best fit between the model and experiment is for $Rp = 1.24$. The differences are 1.8, 1.3, 0.8 and 1.2 µm ($Dv90$, $Dv50$, $Dv10$ and D_{32}), which give only 1.9, 2.8, 3.6 and 3.2%, respectively. This, of course, can be case specific and may be different for other sets of data. Despite the discussed differences, the major trend of the flash-boiling effect on droplet sizing can be seen in $CDFs$ plots. Along with the overheat increase, CDF characteristics are shifted to the left side, and their slope is distinctly increased.

TABLE 6: $Dv10$, $Dv50$, $Dv90$ and D_{32} metrics for log-normal distribution and for modelled distributions at $T_{fluid} = 120\,°C$

		Log normal fit				**Model calculations**			
Rp	ΔT	$Dv10$	$Dv50$	$Dv90$	D_{32}	$Dv10$	$Dv50$	$Dv90$	D_{32}
[-]	°C	[µm]				[µm]			
0.90	-3	28.7	60.9	129.0	51.1	28.6	65.8	151.6	52.8
1.10	3	26.0	54.5	114.3	46.0	22.7	50.8	114.1	41.6
1.43	10	21.7	45.5	95.2	38.5	18.2	39.3	84.5	32.8
1.59	13	18.9	39.4	81.9	33.4	17.1	36.0	76.0	30.4
1.79	16	17.0	33.0	64.1	28.9	16.1	33.1	68.0	28.2
2.05	20	17.3	31.3	56.7	28.1	15.2	30.3	60.5	26.2
2.39	24	17.8	31.0	54.1	28.2	14.6	27.8	53.2	24.5

The same set of graphs was plotted for the worst-case scenario in Fig. 48. The worst-case scenario is where the model equations (eq. 24 and eq. 25) were tuned with the lowest agreement, which was for $T_{fluid} = 140$ °C. It can be seen that thanks to the generalized model, the modelled $PDFs$ and $CDFs$ are behaving in the same way as observed in Fig. 47. Also, the modes on $PDFs$ plots are lower than log-normal fit to experimental data, while for high Rp the experimental modes are exceeded by the model. In this case, however, the differences are more visible, especially for the boundary values of Rp. Table 7 contains the main metrics for discussed plots in Fig. 48. The highest deviations between the log-normal distribution fitted to the experimental data and modelled distributions are for the lowest Rp (1.03) the difference for $Dv90$ is 18.1 µm (14.6%), while for $Dv50$ and $Dv10$ are 6.6 and 2.2 µm (11.1% and 7.7%), respectively. The overall difference for D_{32} is 4.6 µm, which is 10.1%. For the highest Rp (1.89), those differences are 8.2, 2.8, 0.8 and 2 µm ($Dv90$, $Dv50$, $Dv10$ and D_{32}), which is 10, 6.9, 3.7 and 5.6%, respectively. The same trend as for the previous case can be observed;

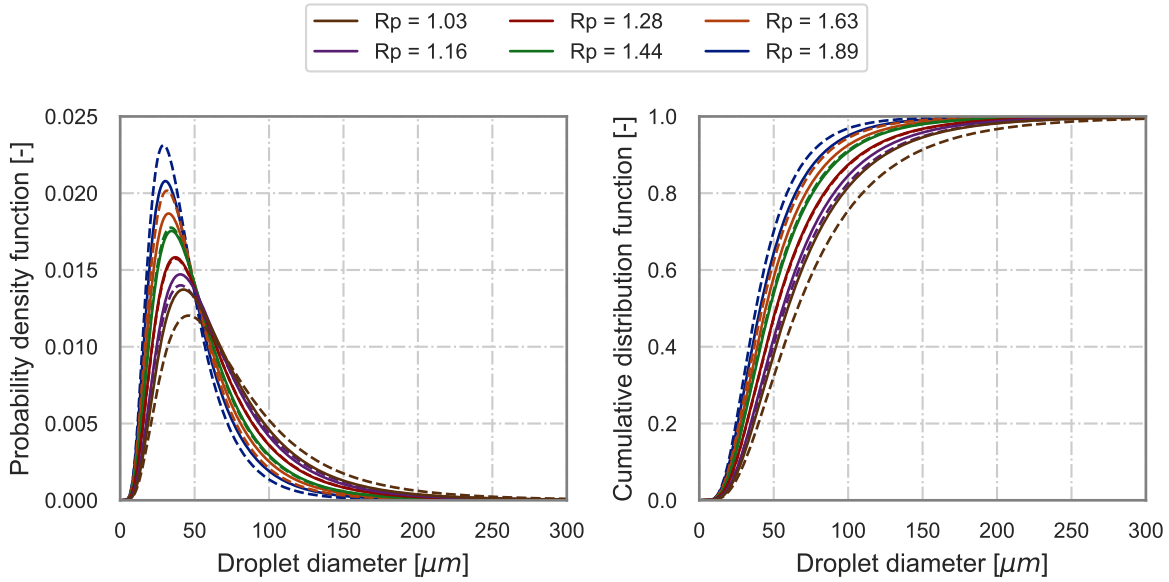

FIGURE 48: The worst-case scenario. The droplet size distribution calculated by the model (dashed line), and the log-normal distribution fitted to the experimental data (solid line) for $T_{fluid} = 140\,°C$

for low superheat ratio, the model tends to overestimate droplet sizes, while for high Rp, the sizes are underestimated. Also in this case, the best fit can be found for the middle range of examined Rp. For $Rp = 1.28$, the deviation does not exceed 0.6% for each discussed metric. To sum up, although this case was called the worst-case scenario, the model also captures the main trend with satisfactory agreement, especially considering that the whole spectrum of sizes is simulated simultaneously.

TABLE 7: $Dv10$, $Dv50$, $Dv90$ and D_{32} metrics for log-normal distribution and for modelled distributions at $T_{fluid} = 140\,°C$

		Log normal fit				**Model calculations**			
Rp	ΔT	$Dv10$	$Dv50$	$Dv90$	D_{32}	$Dv10$	$Dv50$	$Dv90$	D_{32}
[-]	°C	[μm]				[μm]			
1.03	1	28.3	59.4	124.7	50.2	30.5	66.0	142.8	54.8
1.16	5	26.9	55.9	116.2	47.4	27.0	57.5	122.4	48.2
1.28	9	24.7	51.6	108.0	43.7	24.7	51.9	108.7	43.9
1.44	12	23.0	47.3	97.4	40.4	22.8	46.8	96.2	39.9
1.63	17	21.7	44.6	91.4	38.1	21.0	42.2	84.7	36.4
1.89	21	20.3	40.9	82.1	35.2	19.6	38.1	73.9	33.3

Despite the observed differences, the model reflects the main trends with the satisfactory agreement. The proposed averaged equations (eq. 24 and eq. 25) to model the log-normal parameters σ and μ were validated and can be used to simulate the droplet size distribution change due to flash-boiling. The model also leaves room for adjustments for different conditions in terms of fluid temperature.

Chapter 4

Summary and conclusions

Within this work, the flash-boiling effect on droplet size distribution for low-pressure injection was investigated under various conditions in terms of ambient pressure and fluid temperature. The systematic work on literature review, experimental setup preparation, planning and conducting experiments, data analysis, and model for droplet size distribution creation was conducted to fill the knowledge gap in the state-of-the-art in the discussed subject.

The extensive literature review was conducted in order to find a knowledge gap that is filled as a contribution of the dissertation. It was pointed out that in the studies on flash-boiling effects on low pressure injection in various ambient pressure and fluid temperatures were not controlled individually using the same experimental setup. Also, there is a lack of the studies regarding the influence of flash-boiling effects on statistical droplet diameter distribution, since the previous focus was put on mean effects.

In order to explore the abovementioned topics, the set of experiments was conducted in a constant volume vessel with optical access that allowed for a flexible ambient pressure adjustment. Moreover, the injector's temperature was controlled through the cooling jacket by the heated oil. Such a setup allowed for flexible adjustment of the temperature of injected fluid and the ambient pressure conditions. The tests were conducted for both overheated and non-overheated conditions. To quantify the droplet sizes, a shadowgraph method was used.

The conducted tests for non-overheated conditions distinctly showed that both ambient pressure and temperature of injected fluid are relevant for the atomization process, and analysed droplet size distribution was substantially different. The same effect could be observed for flash-boiling conditions. The comparison of different cases at approximately the same overheat expressed by Rp shows that droplet size distributions are distinctly different. Despite the fact that the flash-boiling effect is considered the main driver for droplet breakup and overall atomization process, the temperature of the injected liquid and ambient pressure also play important roles in droplet size distribution formation. Nevertheless, the tests' results grouped by the same liquid temperature showed that the droplet size reduction followed the regular and, more importantly, consistent trend. This looks as follows, with overheat ratio (Rp) increase,

the mode of the droplet size distribution is shifted to the left and rise up, while the tail of the distribution is shortened with a sharper decrease. For cumulative characteristics, it can be seen a corresponding tendency to drag the distribution toward smaller diameters, and what is also important, this is done in the whole range of droplet sizes. In other words, the droplet size reduction is observed for the whole range of sizes; thus, big and small droplets are reduced by flash boiling consistently. Finally, the size-reduction effect is slowing down (in a hyperbolic manner) as Rp is increased.

Based on the previous findings, the model to calculate a droplet size distribution at a given Rp was created, with assumptions that it should simulate the main trend for each liquid temperature series as discussed previously, but it allows for the adjustment to given liquid temperature in order to include the effects of ambient pressure and fluid temperature on the droplet sizing. The log-normal function was used to represent the experimental droplet size distribution. Based on this function, a model to simulate the variables of log-normal function in the function of overheat ratio was created and validated. The rate of the droplet size reduction was averaged over the liquid temperature data series in order to obtain a main global effect of droplet reduction. At the same time, room for adjustment to account for different conditions was left through intercepts.

The overall model performance assessed based on the coefficient of determination between the log-normal and model quantiles is $R^2 = 0.951$, which was considered a satisfactory agreement. Compared to the experimental data coefficients of determination, the main metrics: $Dv10$, $Dv50$, $Dv90$ and D_{32} are 0.916, 0.851, 0.898 and 0.917. Such a correlation is considered satisfactory, especially taking into account a variety of experimental conditions and also the nature of droplet size reduction during the flash-boiling injection. The distributions change from medium to highly skewed over the different levels of overheating. Despite the observed differences in the model, the main trends of the droplet reduction are reflected in the good and consistent agreement.

Summarizing, the research proves the hypothesis stated at the beginning of the dissertation. It was shown that droplet size distribution undergoes a systematic change in terms of both the average parameters and its shape depending on intensity of flash boiling and this effect was modelled using the log-normal probability in function of superheat ratio.

Bibliography

[1] S. T. Chin and C.-F. F. Lee, "Numerical investigation of the effect of wall wetting on hydrocarbon emissions in engines", *Proceedings of the Combustion Institute*, vol. 29, no. 1, pp. 767–773, 2002, Proceedings of the Combustion Institute, ISSN: 1540-7489. DOI: https://doi.org/10.1016/S1540-7489(02)80098-0.

[2] J. Serras-Pereira, P. G. Aleiferis, and D. Richardson, "Imaging and heat flux measurements of wall impinging sprays of hydrocarbons and alcohols in a direct-injection spark-ignition engine", *Fuel*, vol. 91, no. 1, pp. 264–297, 2012, ISSN: 0016-2361. DOI: https://doi.org/10.1016/j.fuel.2011.07.037.

[3] H. Smith, T. Lauer, M. Mayer, and S. Pierson, "Optical and numerical investigations on the mechanisms of deposit formation in scr systems", *SAE International Journal of Fuels and Lubricants*, vol. 7, no. 2, pp. 525–542, 2014, ISSN: 1946-3952. DOI: https://doi.org/10.4271/2014-01-1563.

[4] F. Birkhold, U. Meingast, and P. Wassermann, "Analysis of the injection of urea-water-solution for automotive scr denox-systems: Modeling of two-phase flow and spray/wall-interaction", in *SAE 2006 World Congress Exhibition*, SAE International, 2006. DOI: https://doi.org/10.4271/2006-01-0643.

[5] W. Brack, B. Heine, F. Birkhold, M. Kruse, and O. Deutschmann, "Formation of urea-based deposits in an exhaust system: Numerical predictions and experimental observations on a hot gas test bench", *Emission Control Science and Technology*, vol. 2, no. 3, pp. 115–123, 2016, ISSN: 2199-3637. DOI: 10.1007/s40825-016-0042-2.

[6] M. Lecompte, S. Raux, and A. Frobert, "Experimental characterization of scr denox-systems: Visualization of urea-water-solution and exhaust gas mixture", in *SAE 2014 World Congress Exhibition*, SAE International, 2014. DOI: https://doi.org/10.4271/2014-01-1524.

[7] M. Sens, J. Maass, S. Wirths, and R. Marohn, "Effects of highly-heated fuel and/or high injection pressures on the spray formation of gasoline direct injection injectors", in *Fuel Systems for IC Engines*, IMechE, Ed. Woodhead Publishing, 2012, pp. 215–238, ISBN: 978-0-85709-210-6. DOI: https://doi.org/10.1533/9780857096043.6.215.

[8] I. Schmitz and A. Leipertz, "Comparison of the flash boiling influence on the spray structure of a high pressure swirl injector and of a multihole injector for gdi engines",

in *10th International Conference on Liquid Atomization and Spray Systems*, vol. 06026, 2006.

[9] M. Xu, Y. Zhang, W. Zeng, G. Zhang, and M. Zhang, "Flash boiling: Easy and better way to generate ideal sprays than the high injection pressure", *SAE International Journal of Fuels and Lubricants*, vol. 6, no. 1, pp. 2013-01–1614, 2013, ISSN: 1946-3960. DOI: 10.4271/2013-01-1614.

[10] L. J. Kapusta, R. Rogoz, and J. Bachanek, "Experimental and numerical study to evaluate the effect of flash boiling on urea-water solution sprays and SCR system performance", *Atomization and Sprays*, vol. 43, pp. 1–43, 2021.

[11] L. J. Kapusta, R. Rogoz, J. Bachanek, L. Boruc, and A. Teodorczyk, "Low-pressure injection of water and urea-water solution in flash-boiling conditions", *SAE Technical Papers*, no. 2020, 2020, ISSN: 01487191. DOI: 10.4271/2020-01-2110.

[12] L. J. Kapusta, "Understanding the collapse of flash-boiling sprays formed by multi- hole injectors operating at low injection pressures", *Energy*, vol. 247, 2022. DOI: 10.1016/j.energy.2022.123388.

[13] N. van Vuuren, G. Brizi, G. Buitoni, L. Postrioti, and C. Ungaro, "Experimental analysis of the urea-water solution temperature effect on the spray characteristics in scr systems", in *12th International Conference on Engines Vehicles*, SAE International, 2015. DOI: https://doi.org/10.4271/2015-24-2500.

[14] N. van Vuuren, C. Ungaro, G. Brizi, G. Buitoni, and L. Postrioti, "Aus-32 injector spray imaging on hot air flow bench", in *SAE 2015 World Congress Exhibition*, SAE International, 2015. DOI: https://doi.org/10.4271/2015-01-1031.

[15] M. Krämer, E. Kull, and M. Wensing, "Flashboiling-induced targeting changes in gasoline direct injection sprays", *International Journal of Engine Research*, vol. 17, no. 1, pp. 97–107, 2016. DOI: 10.1177/1468087415604763.

[16] H. Kamoun, G. Lamanna, B. Weingand, and J. Steelant, "High-speed shadowgraphy investigations of superheated liquid jet atomisation", in *ILASS-Americas 22nd Annual Conference on Liquid Atomization and Spray Systems*, 2010.

[17] M. M. Khan, J. Hélie, M. Gorokhovski, and N. A. Sheikh, "Experimental and numerical study of flash boiling in gasoline direct injection sprays", *Applied Thermal Engineering*, vol. 123, pp. 377–389, 2017, ISSN: 1359-4311. DOI: https://doi.org/10.1016/j.applthermaleng.2017.05.102.

[18] R. D. Oza and J. F. Sinnamon, "An experimental and analytical study of flash-boiling fuel injection", in *SAE International Congress and Exposition*, vol. 92, SAE International, 1983, pp. 948–962. DOI: https://doi.org/10.4271/830590.

[19] M. Chang, Z. Lee, S. Park, and S. Park, "Characteristics of flash boiling and its effects on spray behavior in gasoline direct injection injectors: A review", *Fuel*, vol. 271,

p. 117 600, 2020, ISSN: 0016-2361. DOI: https://doi.org/10.1016/j.fuel.2020.117600.

[20] T. Bar-Kohany and M. Levy, "State of the art review of flash-boiling atomization", *Atomization and Sprays*, vol. 26, no. 12, pp. 1259–1305, 2016, ISSN: 1044-5110. DOI: 10.1615/AtomizSpr.2016015626.

[21] W. G. Courtney, "Remarks on homogeneous nucleation", *The Journal of Chemical Physics*, vol. 35, no. 6, pp. 2249–2250, 1961. DOI: 10.1063/1.1732252.

[22] M. Alamgir and J. H. Lienhard, "Correlation of pressure undershoot during hot-water depressurization", *Journal of Heat Transfer*, vol. 103, no. 1, pp. 52–55, 1981, ISSN: 0022-1481. DOI: 10.1115/1.3244429.

[23] E. Elias and P. L. Chambret', "Flashing inception in water during rapid decompression", *Journal of Heat Transfer*, vol. 115, no. 1, pp. 231–238, 1993, ISSN: 0022-1481. DOI: 10.1115/1.2910654.

[24] R. Karami and N. Ashgriz, *Handbook of atomization and sprays. Theory and applications.* N. Ashgrix, Ed. Springer, ISBN: 9781441972637.

[25] Y. Kitamura, H. Morimitsu, and T. Takahashi, "Critical superheat for flashing of superheated liquid jets", *Industrial Engineering Chemistry Fundamentals*, vol. 25, no. 2, pp. 206–211, 1986. DOI: 10.1021/i100022a005.

[26] J. Zhou, P. Xu, B. Qi, Y. Zhang, and J. Wei, "Effects of micro-pin-fins on the bubble growth and movement of nucleate pool boiling on vertical surfaces", *International Journal of Thermal Sciences*, vol. 171, p. 107 186, 2022, ISSN: 1290-0729. DOI: https://doi.org/10.1016/j.ijthermalsci.2021.107186.

[27] S. Yang, S. Wang, Z. Sun, X. Li, D. L. S. Hung, and M. Xu, "In-nozzle bubble formation and its effect on fuel jet breakup under cavitating and flash boiling conditions", *Applied Thermal Engineering*, vol. 183, p. 116 120, 2021, ISSN: 1359-4311. DOI: https://doi.org/10.1016/j.applthermaleng.2020.116120.

[28] D. Dietzel, T. Hitz, C.-D. Munz, and A. Kronenburg, "Single vapour bubble growth under flash boiling conditions using a modified hllc riemann solver", *International Journal of Multiphase Flow*, vol. 116, pp. 250–269, 2019, ISSN: 0301-9322. DOI: https://doi.org/10.1016/j.ijmultiphaseflow.2019.04.010.

[29] X. Xi, H. Liu, M. Jia, M. Xie, and H. Yin, "A new flash boiling model for single droplet", *International Journal of Heat and Mass Transfer*, vol. 107, pp. 1129–1137, 2017, ISSN: 0017-9310. DOI: https://doi.org/10.1016/j.ijheatmasstransfer.2016.11.027.

[30] H. S. Lee and H. Merte, "Spherical vapor bubble growth in uniformly superheated liquids", *International Journal of Heat and Mass Transfer*, vol. 39, no. 12, pp. 2427–2447, 1996, ISSN: 0017-9310. DOI: https://doi.org/10.1016/0017-9310(95)00342-8.

[31] D.-L. Chang and C.-F. F. Lee, "Development of a simplified bubble growth model for flash boiling sprays in direct injection spark ignition engines", *Proceedings of the Combustion Institute*, vol. 30, no. 2, pp. 2737–2744, 2005, ISSN: 1540-7489. DOI: https://doi.org/10.1016/j.proci.2004.08.149.

[32] S. Suma and M. Koizumi, "Internal boiling atomization by rapid pressure reduction of liquids", *Trans. JSME (B)*, vol. 43, no. 376, pp. 4608–4617, 1977.

[33] D. Kawano, Y. Goto, M. Odaka, and J. Senda, "Modeling atomization and vaporization processes of flash-boiling spray", in *SAE 2004 World Congress Exhibition*, SAE International, Mar. 2004. DOI: https://doi.org/10.4271/2004-01-0534.

[34] G. Lamanna, H. Kamoun, B. Weigand, and J. Steelant, "Towards a unified treatment of fully flashing sprays", *International Journal of Multiphase Flow*, vol. 58, pp. 168–184, 2014, ISSN: 0301-9322. DOI: https://doi.org/10.1016/j.ijmultiphaseflow.2013.08.010.

[35] J. Senda, Y. Hojyo, and H. Fujimoto, "Modelling of atomization process in flash boiling spray", *SAE Transactions*, vol. 103, no. 1994, pp. 1026–1040, 1994, ISSN: 0096736X, 25771531.

[36] B. Zuo, A. M. Gomes, and C. J. Rutland, "Modelling superheated fuel sprays and vaporization", *International Journal of Engine Research*, vol. 1, no. 4, pp. 321–336, 2000. DOI: 10.1243/1468087001545218.

[37] L. Araneo, G. Brunello, A. Coghe, R. Donde, R. Dondé, L. Araneo, and A. Coghe, "Effects of fuel temperature and ambient pressure on a gdi swirled injector spray", in *CEC/SAE Spring Fuels Lubricants Meeting Exposition*, SAE International, 2000, pp. 1–15. DOI: https://doi.org/10.4271/2000-01-1901.

[38] M. M. Vieira and J. R. Simoes-Moreira, "Low-pressure flashing mechanisms in isooctane liquid jets", *Journal of Fluid Mechanics*, vol. 572, pp. 121–144, 2007. DOI: 10.1017/S0022112006003430.

[39] M. Mojtabi, N. Chadwick, G. Wigley, and J. Helie, "The effect of flash boiling on break up and atomization in gdi sprays", *22nd European Conference on Liquid Atomization and Spray Systems*, pp. 8–10, 2008. DOI: ILASS08-6-1.

[40] J. Serras-Pereira, Z. van Romunde, P. G. Aleiferis, D. Richardson, S. Wallace, and R. F. Cracknell, "Cavitation, primary break-up and flash boiling of gasoline, iso-octane and n-pentane with a real-size optical direct-injection nozzle", *Fuel*, vol. 89, no. 9, pp. 2592–2607, 2010, ISSN: 0016-2361. DOI: https://doi.org/10.1016/j.fuel.2010.03.030.

[41] S. L. Girshick, C. P. Chiu, P. H. Mcmurry, S. L. Girshick, C. P. Chiu, and P. H. Mcmurry, "Time-dependent aerosol models and homogeneous nucleation rates", *Aerosol Science and Technology*, vol. 13, pp. 465–477, 1990. DOI: 10.1080/02786829008959461.

[42] R. Arora, C. J. Morgan, J. D. Naber, and S.-y. Lee, "Flash boiling spray characterization of a gasoline multi-hole injector in a heated pressure vessel", in *23nd Annual Conference on Liquid Atomization and Spray Systems*, 2011.

[43] P. G. Aleiferis and Z. R. van Romunde, "An analysis of spray development with iso-octane, n-pentane, gasoline, ethanol and n-butanol from a multi-hole injector under hot fuel conditions", *Fuel*, vol. 105, pp. 143–168, 2013, ISSN: 0016-2361. DOI: https://doi.org/10.1016/j.fuel.2012.07.044.

[44] L. Allocca, A. Montanaro, R. D. Gioia, and G. Bonandrini, "Spray characterization of a single-hole gasoline injector under flash boiling conditions", *SAE Technical Papers*, vol. 2014, no. January 2019, 2014. DOI: 10.4271/2014-32-0041.

[45] D. Weber and P. Leick, "Structure and velocity field of individual plumes of flashing gasoline direct injection sprays", in *ILASS Europe 2014, 26th Annual Conference on Liquid Atomization and Spray Systems*, 2014. DOI: 10.13140/RG.2.1.1227.2724.

[46] H. Guo, B. Wang, Y. Li, H. Xu, and Z. Wu, "Characterizing external flashing jet from single-hole gdi injector", *International Journal of Heat and Mass Transfer*, vol. 121, pp. 924–932, 2018, ISSN: 0017-9310. DOI: 10.1016/j.ijheatmasstransfer.2018.01.042.

[47] H. Guo, Y. Li, X. Lu, Z. Zhou, H. Xu, and Z. Wang, "Radial expansion of flash boiling jet and its relationship with spray collapse in gasoline direct injection engine", *Applied Thermal Engineering*, vol. 146, no. October, pp. 515–525, 2019, ISSN: 13594311. DOI: 10.1016/j.applthermaleng.2018.10.031.

[48] J. D. Naber and D. L. Siebers, "Effects of gas density and vaporization on penetration and dispersion of diesel sprays", in *International Congress Exposition*, SAE International, 1996. DOI: https://doi.org/10.4271/960034.

[49] B. Wang, Z. Wang, X. Bao, Y. Li, Y. Jiang, H. Xu, and X. Zhang, "Microscopic investigation of near-field spray characteristics of 2-methylfuran, ethanol and isooctane under flash boiling conditions", *Fuel*, vol. 215, pp. 142–152, 2018, ISSN: 0016-2361. DOI: https://doi.org/10.1016/j.fuel.2017.10.035.

[50] X. Li, S. Yang, T. Li, D. L. S. Hung, and M. Xu, "Investigations on near-field atomization of flash boiling sprays for gasoline direct injection related applications", *Fuel*, vol. 257, p. 116 097, 2019, ISSN: 0016-2361. DOI: https://doi.org/10.1016/j.fuel.2019.116097.

[51] W. Zhao, J. Yan, S. Gao, T. H. Lee, and X. Li, "Effects of fuel properties and aerodynamic breakup on spray under flash boiling conditions", *Applied Thermal Engineering*, vol. 200, p. 117 646, 2022, ISSN: 1359-4311. DOI: https://doi.org/10.1016/j.applthermaleng.2021.117646.

[52] S. E. Parrish and R. J. Zink, "Spray characteristics of multi-hole injectors under flash boiling conditions", in *21st Annual Conference on Liquid Atomization and Spray Systems*, vol. ill, 2008.

[53] W. Zeng, M. Xu, G. Zhang, Y. Zhang, and D. J. Cleary, "Atomization and vaporization for flash-boiling multi-hole sprays with alcohol fuels", *Fuel*, vol. 95, pp. 287–297, 2012, ISSN: 00162361. DOI: 10.1016/j.fuel.2011.08.048.

[54] G. Zhang, M. Xu, Y. Zhang, M. Zhang, and D. J. Cleary, "Macroscopic characterization of flash-boiling multi-hole sprays using planar laser induced exciplex fluorescence technique. part i . on-axis spray structure", *Atomization and Sprays*, vol. 22, no. 10, pp. 861–878, 2012. DOI: 10445110/12/.

[55] Q. N. Chan, Y. Bao, and S. Kook, "Effects of injection pressure on the structural transformation of flash-boiling sprays of gasoline and ethanol in a spark-ignition direct-injection (sidi) engine", *FUEL*, vol. 130, pp. 228–240, 2014, ISSN: 0016-2361. DOI: 10.1016/j.fuel.2014.04.015.

[56] Y. Huang, S. Huang, R. Huang, and G. Hong, "Spray and evaporation characteristics of ethanol and gasoline direct injection in non-evaporating , transition and flash-boiling conditions", *Energy Conversion and Management*, vol. 108, pp. 68–77, 2016, ISSN: 0196-8904. DOI: 10.1016/j.enconman.2015.10.081.

[57] S. Wu, M. Xu, D. L. S. Hung, T. Li, and H. Pan, "Near-nozzle spray and spray collapse characteristics of spark-ignition direct-injection fuel injectors under sub-cooled and superheated conditions", *Fuel*, vol. 183, pp. 322–334, 2016, ISSN: 0016-2361. DOI: 10.1016/j.fuel.2016.06.080.

[58] S. Moon, C. Bae, E. Abo-Serie, and J. Choi, "Internal and near-nozzle flow of a pressure-swirl atomizer under varied fuel temperature", *Atomization and Sprays*, vol. 17, pp. 529–550, 2007. DOI: 10.1615/AtomizSpr.v17.i6.30.

[59] L. Araneo and R. Donde, "Flash boiling in a multihole g-di injector effects of the fuel distillation curve", *Fuel*, vol. 191, pp. 500–510, 2017, ISSN: 0016-2361. DOI: https://doi.org/10.1016/j.fuel.2016.11.104.

[60] H. Guo, H. Ding, Y. Li, X. Ma, Z. Wang, H. Xu, and J. Wang, "Comparison of spray collapses at elevated ambient pressure and flash boiling conditions using multi-hole gasoline direct injector", *Fuel*, vol. 199, pp. 125–134, 2017, ISSN: 0016-2361. DOI: 10.1016/j.fuel.2017.02.071.

[61] J. Lacey, F. Poursadegh, M. J. Brear, R. Gordon, P. Petersen, C. Lakey, B. Butcher, and S. Ryan, "Generalizing the behavior of flash-boiling, plume interaction and spray collapse for multi-hole, direct injection", *Fuel*, vol. 200, pp. 345–356, 2017, ISSN: 0016-2361. DOI: https://doi.org/10.1016/j.fuel.2017.03.057.

[62] Z. Wang, C. Jiang, H. Xu, T. Badawy, B. Wang, and Y. Jiang, "The influence of flash boiling conditions on spray characteristics with closely coupled split injection strategy",

Applied Energy, vol. 187, pp. 523–533, 2017, ISSN: 0306-2619. DOI: https://doi.org/10.1016/j.apenergy.2016.11.089.

[63] Y. Li, H. Guo, S. Fei, X. Ma, Z. Zhang, L. Chen, L. Feng, and Z. Wang, "An exploration on collapse mechanism of multi-jet flash-boiling sprays", *Applied Thermal Engineering*, vol. 134, pp. 20–28, 2018, ISSN: 1359-4311. DOI: https://doi.org/10.1016/j.applthermaleng.2018.01.102.

[64] Y. Li, H. Guo, X. Ma, Y. Qi, Z. Wang, H. Xu, and S. Shuai, "Morphology analysis on multi-jet flash-boiling sprays under wide ambient pressures", *Fuel*, vol. 211, pp. 38–47, 2018, ISSN: 0016-2361. DOI: https://doi.org/10.1016/j.fuel.2017.08.082.

[65] C. Jiang, M. C. Parker, D. Butcher, A. Spencer, C. P. Garner, and J. Helie, "Comparison of flash boiling resistance of two injector designs and the consequences on downsized gasoline engine emissions", *Applied Energy*, vol. 254, p. 113 735, 2019, ISSN: 0306-2619. DOI: https://doi.org/10.1016/j.apenergy.2019.113735.

[66] C. Jiang, M. C. Parker, J. Helie, A. Spencer, C. P. Garner, and G. Wigley, "Impact of gasoline direct injection fuel injector hole geometry on spray characteristics under flash boiling and ambient conditions", *Fuel*, vol. 241, pp. 71–82, 2019, ISSN: 0016-2361. DOI: https://doi.org/10.1016/j.fuel.2018.11.143.

[67] Y. Li, H. Guo, Z. Zhou, Z. Zhang, X. Ma, and L. Chen, "Spray morphology transformation of propane, n-hexane and iso-octane under flash-boiling conditions", *Fuel*, vol. 236, pp. 677–685, 2019, ISSN: 0016-2361. DOI: https://doi.org/10.1016/j.fuel.2018.08.160.

[68] L. Wang, F. Wang, and T. Fang, "Flash boiling hollow cone spray from a gdi injector under different conditions", *International Journal of Multiphase Flow*, vol. 118, pp. 50–63, 2019, ISSN: 0301-9322. DOI: 10.1016/j.ijmultiphaseflow.2019.05.009.

[69] S. Wu, S. Yang, M. Wooldridge, and M. Xu, "Experimental study of the spray collapse process of multi-hole gasoline fuel injection at fl ash boiling conditions", *Fuel*, vol. 242, no. October 2018, pp. 109–123, 2019, ISSN: 0016-2361. DOI: 10.1016/j.fuel.2019.01.027.

[70] Q. Xu, H. Pan, Y. Gao, X. Li, and M. Xu, "Investigation of two-hole flash-boiling plume-to-plume interaction and its impact on spray collapse", *International Journal of Heat and Mass Transfer*, vol. 138, pp. 608–619, 2019, ISSN: 0017-9310. DOI: https://doi.org/10.1016/j.ijheatmasstransfer.2019.04.111.

[71] J. Du, B. Mohan, J. Sim, T. Fang, and W. L. Roberts, "Study of spray collapse phenomenon at flash boiling conditions using simultaneous front and side view imaging", *International Journal of Heat and Mass Transfer*, vol. 147, p. 118 824, 2020, ISSN: 0017-9310. DOI: https://doi.org/10.1016/j.ijheatmasstransfer.2019.118824.

[72] J. Du, G. Zang, B. Mohan, R. Idoughi, J. Sim, T. Fang, P. Wonka, W. Heidrich, and W. L. Roberts, "Study of spray structure from non-flash to flash boiling conditions with space-time tomography", *Proceedings of the Combustion Institute*, vol. 38, no. 2, pp. 3223–3231, 2021, ISSN: 1540-7489. DOI: https://doi.org/10.1016/j.proci.2020.06.171.

[73] M. Chang, J. Park, H. Ik, and S. Park, "Comparison of spray evaporation characteristics of five-hole gdi injectors with different hole arrangements under flash boiling conditions", *International Journal of Heat and Mass Transfer*, vol. 181, p. 121 841, 2021, ISSN: 0017-9310. DOI: https://doi.org/10.1016/j.ijheatmasstransfer.2021.121841.

[74] W. Liu, Y. Lu, Y. Kang, J. Yan, and C.-f. Lee, "Macroscopic characteristics of flash-boiling spray focused on plume interaction", *International Journal of Heat and Mass Transfer*, vol. 170, p. 120 999, 2021, ISSN: 0017-9310. DOI: https://doi.org/10.1016/j.ijheatmasstransfer.2021.120999.

[75] B. S. Park and S. Y. Lee, "An experimental investigation of flash atomization mechanism", *Atomization and Sprays*, vol. 4, pp. 159–179, 1994.

[76] R. Lecourt, P. Barricau, J. Steelant, and N. Ag, "Spray velocity and drop size measurements in vacuum conditions", in *20th Annual Conference on Liquid Atomization and Spray System*, 2007.

[77] V. Cleary, P. Bowen, and H. Witlox, "Flashing liquid jets and two-phase droplet dispersion i . experiments for derivation of droplet atomisation correlations", vol. 142, pp. 786–796, 2007. DOI: 10.1016/j.jhazmat.2006.06.125.

[78] S. H. Park, H. J. Kim, and C. S. Lee, "Macroscopic spray characteristics and breakup performance of dimethyl ether (dme) fuel at high fuel temperatures and ambient conditions", *Fuel*, vol. 89, no. 10, pp. 3001–3011, 2010, ISSN: 0016-2361. DOI: https://doi.org/10.1016/j.fuel.2010.05.002.

[79] W. Kim, T. Yu, and W. Yoon, "Atomization characteristics of emulsified fuel oil by instant emulsification", *Journal of Mechanical Science and Technology*, vol. 26, no. 6, pp. 1781–1791, 2012, ISSN: 1976-3824. DOI: 10.1007/s12206-012-0422-7.

[80] C.-S. Wen, K.-m. Chung, F. K. Lu, and W.-h. Lai, "Assessment of flash-boiling for pulse detonation engines", *International Journal of Heat and Mass Transfer*, vol. 55, no. 11, pp. 2751–2760, 2012, ISSN: 0017-9310. DOI: https://doi.org/10.1016/j.ijheatmasstransfer.2012.02.030.

[81] H. Kamoun, G. Lamanna, B. Weigand, S. Saengkaew, G. Gréhan, and J. Steelant, "Temperature and droplet size measurements in a flashing ethanol jet using the global rainbow thermometry", in *ILASS Europe 2013, 25th European Conference on Liquid Atomization and Spray Systems*, 2013.

[82] S. Shen, M. Jia, T. Wang, Q. Lü, and K. Sun, "Measurement of the droplets sizes of a flash boiling spray using an improved extended glare point velocimetry and sizing", *Experiments in Fluids*, vol. 57, no. 4, p. 56, 2016, ISSN: 1432-1114. DOI: 10.1007/s00348-016-2147-3.

[83] Y. Liu, Y. Pei, Z. Peng, J. Qin, Y. Zhang, Y. Ren, and M. Zhang, "Spray development and droplet characteristics of high temperature single-hole gasoline spray", *Fuel*, vol. 191, pp. 97–105, 2017, ISSN: 0016-2361. DOI: https://doi.org/10.1016/j.fuel.2016.11.068.

[84] S. Yang, X. Li, D. L. S. Hung, M. Arai, and M. Xu, "In-nozzle flash boiling flow of multi-component fuel and its effect on near-nozzle spray", *Fuel*, vol. 252, pp. 55–67, 2019, ISSN: 0016-2361. DOI: https://doi.org/10.1016/j.fuel.2019.04.104.

[85] O. F. Atac, S. Moon, and J. Jeon, "Unraveling the initial flash boiling spray formation at the same superheated index achieved by altering ambient pressure and fuel temperature independently", *International Journal of Heat and Mass Transfer*, vol. 169, p. 120 897, 2021, ISSN: 0017-9310. DOI: https://doi.org/10.1016/j.ijheatmasstransfer.2020.120897.

[86] J. Yan, S. Gao, W. Liu, T. Chen, T. H. Lee, and C.-F. Lee, "Experimental study of flash boiling spray with isooctane, hexane, ethanol and their binary mixtures", *Fuel*, vol. 292, p. 120 415, 2021, ISSN: 0016-2361. DOI: https://doi.org/10.1016/j.fuel.2021.120415.

[87] S. Gao, J. Yan, T. H. Lee, and C.-F. Lee, "Model development for flash boiling spray and validations with isooctane, hexane, ethanol and their binary mixtures", *Fuel*, vol. 321, p. 123 917, 2022, ISSN: 0016-2361. DOI: https://doi.org/10.1016/j.fuel.2022.123917.

[88] M. Chang, Y. S. Yu, S. Park, and S. Park, "Spray dynamics and atomization characteristics of multi-hole gdi injectors under flash boiling conditions", *Applied Thermal Engineering*, vol. 200, p. 117 626, 2022, ISSN: 1359-4311. DOI: https://doi.org/10.1016/j.applthermaleng.2021.117626.

[89] X. Li, Q. Xu, S. Qiu, S. Wang, D. Hung, and M. Xu, "Investigations on the impact of phase change on single plume flash boiling radial expansion and drop-sizing characteristics", *Applied Thermal Engineering*, vol. 202, no. August 2021, p. 117 911, 2022, ISSN: 1359-4311. DOI: 10.1016/j.applthermaleng.2021.117911.

[90] A. Varna, A. C. Spiteri, Y. M. Wright, P. D. Eggenschwiler, and K. Boulouchos, "Experimental and numerical assessment of impingement and mixing of urea-water sprays for nitric oxide reduction in diesel exhaust", *Applied Energy*, vol. 157, pp. 824–837, 2015, ISSN: 18729118. DOI: 10.1016/j.apenergy.2015.03.015.

[91] R. Rogoz, L. J. Kapusta, J. Bachanek, J. Vankan, and A. Teodorczyk, "Improved urea-water solution spray model for simulations of selective catalytic reduction systems",

Renewable and Sustainable Energy Reviews, vol. 120, p. 109 616, 2020, ISSN: 1364-0321. DOI: https://doi.org/10.1016/j.rser.2019.109616. [Online]. Available: https://www.sciencedirect.com/science/article/pii/S1364032119308238.

[92] R. Payri, G. Bracho, J. Gimeno, and A. Moreno, "Investigation of the urea-water solution atomization process in engine exhaust-like conditions", *Experimental Thermal and Fluid Science*, vol. 108, no. May, pp. 75–84, 2019, ISSN: 0894-1777. DOI: 10.1016/j.expthermflusci.2019.05.019.

[93] L. J. Kapusta and A. Teodorczyk, "Laser diagnostics for urea-water solution spray characterization", *MATEC Web of Conferences*, vol. 118, no. 00029, pp. 1–6, 2017. DOI: 10.1051/matecconf/201711800029.

[94] S. Grout, J.-B. Blaisot, K. Pajot, and G. Osbat, "Experimental investigation on the injection of an ureawater solution in hot air stream for the scr application: Evaporation and spray/wall interaction", *Fuel*, vol. 106, no. x, pp. 166–177, 2013, ISSN: 0016-2361. DOI: https://doi.org/10.1016/j.fuel.2012.09.022.

[95] Y. Liao, P. Dimopoulos Eggenschwiler, D. Rentsch, F. Curto, and K. Boulouchos, "Characterization of the urea-water spray impingement in diesel selective catalytic reduction systems", *Applied Energy*, vol. 205, no. March, pp. 964–975, 2017, ISSN: 03062619. DOI: 10.1016/j.apenergy.2017.08.088.

[96] L. J. Kapusta, M. Sutkowski, R. Rogoz, M. Zommara, and A. Teodorczyk, "Characteristics of water and urea-water solution sprays", *Catalysts*, vol. 9, no. 9, 2019, ISSN: 20734344. DOI: 10.3390/catal9090750.

[97] P. Linstrom, W. Mallard, and Eds., *Nist chemistry webbook, nist standard reference database number 69*, Washington, D.C., 2001. DOI: /10.18434/T4D303.

[98] A. Wood, G. Wigley, and J. Helie, "Flash boiling sprays produced by a 6-hole gdi injector", *International Symposium on Applications of Laser Techniques to Fluid Mechanics*, vol. i, no. Kawano 2006, pp. 7–10, 2014, ISSN: 14685884. DOI: 10.13140/2.1.5105.3445.

[99] M. Mahabat, J. Hélie, M. Gorokhovski, and N. Ahmed, "Experimental and numerical study of flash boiling in gasoline direct injection sprays", *Applied Thermal Engineering*, vol. 123, pp. 377–389, 2017, ISSN: 1359-4311. DOI: 10.1016/j.applthermaleng.2017.05.102.

[100] P. Virtanen, R. Gommers, T. E. Oliphant, M. Haberland, T. Reddy, D. Cournapeau, E. Burovski, P. Peterson, W. Weckesser, J. Bright, S. J. van der Walt, M. Brett, J. Wilson, K. J. Millman, N. Mayorov, A. R. J. Nelson, E. Jones, R. Kern, E. Larson, C. J. Carey,. Polat, Y. Feng, E. W. Moore, J. VanderPlas, D. Laxalde, J. Perktold, R. Cimrman, I. Henriksen, E. A. Quintero, C. R. Harris, A. M. Archibald, A. H. Ribeiro, F. Pedregosa, P. van Mulbregt, and S. 1. Contributors, "SciPy 1.0: Fundamental algorithms for scientific

computing in python", *Nature Methods*, vol. 17, pp. 261–272, 2020. DOI: 10.1038/s41592-019-0686-2.

[101] J. L. Hodges, "The significance probability of the smirnov two-sample test", *Arkiv för Matematik*, vol. 3, no. 5, pp. 469–486, 1958. DOI: 10.1007/BF02589501.

[102] S. P. Lin and R. D. Reitz, "Drop and spray formation from a liquid jet", *Annual Review of Fluid Mechanics*, vol. 30, no. 1, pp. 85–105, 1998, ISSN: 0066-4189. DOI: 10.1146/annurev.fluid.30.1.85.

[103] "Ohnesorge number", in *Encyclopedia of Microfluidics and Nanofluidics*. Boston, MA: Springer US, 2008, p. 1513, ISBN: 978-0-387-48998-8. DOI: 10.1007/978-0-387-48998-8_1141.

[104] "Weber number", in *Encyclopedia of Microfluidics and Nanofluidics*. Boston, MA: Springer US, 2008, p. 2185, ISBN: 978-0-387-48998-8. DOI: 10.1007/978-0-387-48998-8_1689.

[105] F. J. M. Jr., "The kolmogorov-smirnov test for goodness of fit", *Journal of the American Statistical Association*, vol. 46, no. 253, pp. 68–78, 1951. DOI: 10.1080/01621459.1951.10500769.